Martin Gottfried Ibel, BSc

# Bulk Current Injection Modelling

**Master's Thesis**

to achieve the university degree of

Master of Science

Master's degree programme: Electrical Engineering

submitted to

**Graz University of Technology**

Supervisor

Univ.-Prof. Dipl.-Ing. Dr.techn. Bernd Deutschmann

Institute of Electronics
Head: Univ.-Prof. Dipl.-Ing. Dr.techn. Bernd Deutschmann

Graz, May 2021

## Affidavit

I declare that I have authored this thesis independently, that I have not used other than the declared sources/resources, and that I have explicitly indicated all material which has been quoted either literally or by content from the sources used. The text document uploaded to TUGRAZonline is identical to the present master's thesis.

| | |
|---|---|
| Date | Signature |

# Acknowledgement

I would first like to thank ams AG and Silicon Austria Labs GmbH. Their funding made this work possible.

I would like to thank the Institute of Electronics and especially my supervisor, Professor Dr Bernd Deutschmann, for his guidance through each stage of the process. Also, I would like to thank Dr Gunter Winkler for his help in conducting the BCI tests and measurements. His calm and sophisticated approach to problem-solving helped me a lot. Next, I want to thank Michael Fuchs for his limitless patience with my numerous requests for measurement equipment.

Also, I want to thank my colleagues from Silicon Austria Labs GmbH and primarily my supervisor Dr Bernhard Auinger, for directing me towards the finishing line. I am incredibly grateful to Dr Herbert Hackl for his help and guidance throughout the whole thesis. I also wish to thank Alex Connaughton, Thomas Langbauer and Franz Vollmaier for their insightful comments and suggestions.

Additionally, I would like to thank my family, my girlfriend, and especially my parents, who made it possible for me to pursue this education through their support.

Finally, I want to thank all my friends for their help and support, and I apologise if I did not have enough time for them.

# Abstract

Bulk Current Injection (BCI) is used in several industry standards to determine the resilience of electronic components against high frequency (HF) disturbance. For this, a disturbance signal is injected into a cable harness connected to the device under test (DUT). In case the DUT fails the test, the necessary redesigns are time-consuming and costly.

Modelling the BCI test itself allows electronic system designers to observe the impacts of the BCI test in circuit simulation and thus adapt initial designs to the requirements of the BCI test before the first "real-world" tests are carried out. This promises to immensely increase the chance of passing the test first time.

The proposed model describes the BCI probe, wire harness, and the coupling between them from 9 kHz to 500 MHz. Based on S-parameter reflection measurements, the probe is modelled by a passive RLC circuit that emulates the BCI probe's input impedance. As the model consists only of ideal passive components, it can be easily imported into any SPICE circuit simulation software. The modelling workflow is described in detail and allows for replication and adaptation to different setups. Comparison to common mode current measurements validates the merit of the proposed model.

# Contents

# List of Figures

# Glossary

**ABS** anti-lock braking system
**AM** amplitude modulation
**AN** artificial network

**BCI** bulk current injection

**CM** common mode
**CW** continuous wave

**dBm** decibel milliwatt
**DC** direct current
**DM** differential mode
**DUT** device under test

**ECU** electronic control unit
**EEC** equivalent electric circuit
**EM** electromagnetic
**EMC** electromagnetic compatibility
**EMF** electromagnetic field
**EMI** electromagnetic immunity
**EUT** equipment under test

**IC** integrated circuit

**LISN** line impedance stabilization network

**MTL** multiconductor transmission line

**p.u.l.** per unit length
**PCB** printed circuit board
**PWM** pulse width modulation

**RF** radio frequency

**TL** transmission line
**TWC** tubular wave coupler
**TWP** twisted wire pair

**VNA** vector network analyzer

# 1. Introduction

In this work methods to model and simulate a bulk current injection (BCI) test according to ISO 11451-4 will be presented including the fundamentals utilized in them. One method is adapted to meet the set objectives and the results are presented and discussed.

## 1.1. Motivation

A modern vehicle holds up to to 5000 m of cables, 500 LEDs and more than 100 control units [1]. Those control units manage not only the radio, the power windows or the air-conditioning they are also responsible for all safety features like anti-lock braking system (ABS) or airbags. A malfunction of one of the safety related systems could be very dangerous for the driver and passengers. Therefore, it is essential to guarantee a certain level of safety and reliability by reducing the level of emitted electromagnetic (EM) disturbances to a minimum and on the other hand increasing the immunity against EM disturbances of all systems in the vehicle. The advance of autonomous driving increases the amount of sensors and electronics even further.

Suppliers of electronic appliances are required to test their devices for electromagnetic compatibility (EMC). EMC testing can be divided into tests to determine immunity against EM disturbances and emission of EM disturbances (Fig. 1.1). Further separating into conducted or radiated emission or immunity respectively. To guarantee that a device satisfies immunity or emission levels the manufacturer needs to test it. For example, vehicle manufacturers need to proof EMC compliance of the whole vehicle. One way to do so is to proof that each utilized sub-system complies with EMC regulations and none of the used sub-systems disturbs or is disturbed by another sub-system.

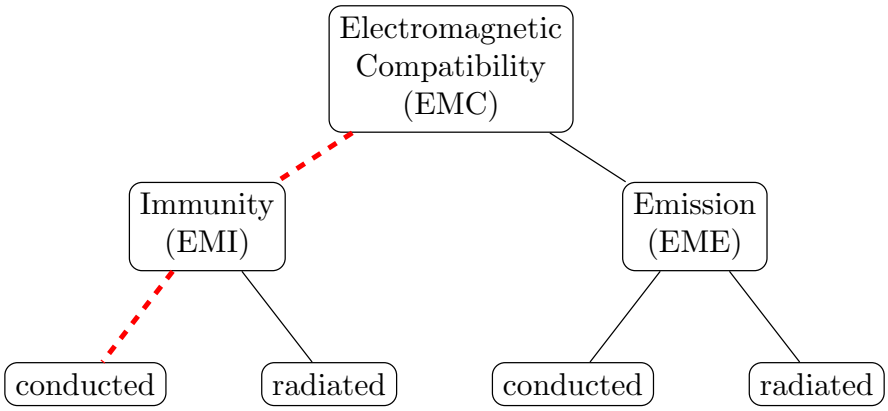


Figure 1.1.: Classification of EMC tests. In red are the sections that include BCI tests.

The BCI test applies to electronic systems and also integrated circuits (ICs) with off-board wire connections, for example cable harness. For the test a radio frequency (RF) current is injected into the wiring harness of the device under test (DUT) through a toroidal injection probe clamped onto the wiring harness. The injection probe can be seen as primary winding of a transformer where the wiring harness forms the secondary winding. A RF voltage is induced into the wires of the harness, producing a current. The level of the current depends on the termination impedances on the source and DUT side, respectively. An additional current measurement probe might be used to monitor the induced current.

The BCI method of immunity testing is utilized in following standards:

| | |
|---|---|
| ISO 11451-4 | Test for vehicles and machines too large to fit into a standard vehicle EMC. |
| ISO 11452-4 | Harness excitation methodes for road vehicles, described in Sec. 2. |
| IEC 62132-3 | Integrated circuits - Measurement of electromagnetic immunity (EMI), 150 kHz to 1 GHz. |
| SAE J1113/4 | Immunity to radiated electromagnetic fields bulk current injection method. |

MIL-STD 461 Requirements for the control of Electromagnetic Interference Characteristics of Subsystems and Equipment Department of Defence Interface Standard.

These tests are costly and can only be done when the first prototypes are available. Not to mention that precious prototypes can be destroyed by the test. If for example problems show up and make a design change necessary the hole cycle starts from the beginning. This is associated with time delays and additional EMC tests which result in a waste of resources and increasing cost. A way of EMC testing in an earlier design stage, before production of prototypes, is desirable and would save resources. Designers of electronic systems and ICs want to predict EMC problems before fabrication. Therefore EMC models like the proposed BCI Model have to be integrated into the design flow. EMC problems could be detected earlier and necessary design changes could be implemented before actual production.

## 1.2. Objectives

Various publications on modelling of BCI tests exist. The published approaches should be compared, combined and applied to the given test setup. Scope of the thesis is to generate an equivalent circuit model of the complete setup, that is specifically, the creation of a circuit model for the simulation of injected BCI currents at the external pins of ICs or electronic systems. The model should be composed of RLC equivalents, to allow versatile use within different circuit simulation environments, e.g. LTSPICE, Keysight ADS or Cadence Spectre. The model should include an equivalent circuit of the current injection into the cable harness of multiple wires using a BCI probe and equivalent circuits of electronic control unit (ECU) (or artificial network (AN), line impedance stabilization network (LISN)) and DUT at the harness ends to mimic their frequency dependent impedances.

The number of wires in the cable harness needs to be adjustable.

The obtained circuit level simulation results should match the measurement results with an accuracy of $\pm 3\,\mathrm{dB}$ from $10\,\mathrm{kHz}$ to $500\,\mathrm{MHz}$, whereas shifts in resonance frequencies of $\pm 10\,\mathrm{MHz}$ are tolerated. Where possible, each

component of the model should be validated regarding this accuracy specification. If the simulation does not achieve the requested performance, the specific deviation and its influence on the overall test result (DC voltage at the DUT) should be discussed.

Which components of the overall model (BCI probe, cable harness, printed circuit board (PCB), DUT) have the most critical impact on the DC voltage reading at the DUT? Which are the components parameters that need to be modelled with high accuracy and which have no critical influence on the overall result?

## 1.3. Structure of the Thesis

The thesis is structured in six chapters. Starting with the introduction which explains the reasoning for this work and presents the foundaitions and current state of work for BCI modelling. Chapter two illustrates the BCI test method by the international standard ISO 11452 Part 4 [2], whilst the third chapter recapitulates the theoretical foundations for the utilized techniques in chapter four, where the used models are explained. The fifth and forelast chapter compares conducted BCI tests with simulations of the proposed novel BCI test model. The thesis concludes with the discussion about proposed model capabilities and limitations. Also an outlook of further development of the proposed model and scientific questions that need to be addressed is given.

## 1.4. Current State of Research

This section gives a brief overview of the most influental works in the topic of BCI modelling. Even though the first publication on the topic has been long time ago the research interest considerably increased in the last couple of years, as shown in Fig. 1.2.

In the paper "Modeling of a bulk current injection setup for susceptibility threshold measurement" [3] Sultan describes a mathematical model for the

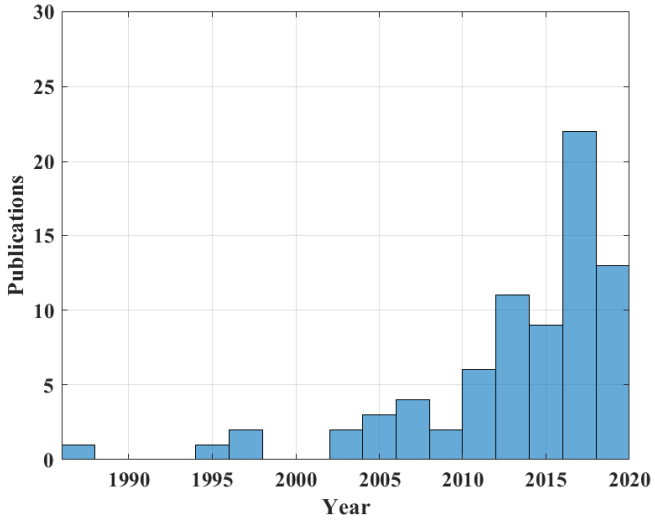


Figure 1.2.: The histogram depicts the number of publications on BCI modelling over time. The utilized data is gathered from *www.ieeexplore.ieee.org*.

current distribution on a multiconductor transmission line (TL) and the sensitivity of the injected current to different parameters.

In [3] the considered coupling effect is sole inductive coupling from the injection probe to the harness wires. The coupling between the wires is considered a mixture of capacitive and inductive coupling. Fig. 1.3 shows the schematic test set-up for the BCI test with the DUT on the right, components or controls on the left and the wiring harness in-between. The injection and monitoring probe are shown on the harness. In [3] this setup is broken down into smaller blocks for easier analytical describtion. The wiring harness is modelled with TLs and the components to the left and the DUT on the right are modelled through their respective input impedances as impedance matrices.

In his approach [3] starts modelling the wiring harness as multiconductor TL over an ideal ground plane as depicted in Fig. 1.4. To simplify calculations the wires are modelled in a constant homogeneous medium with a wire-to-wire distance of at least five times the diameter, to avoid the proximity effect. The

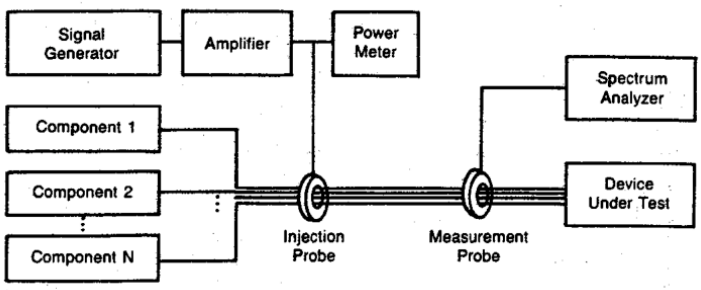


Figure 1.3.: Bulk current injection test setup [3].

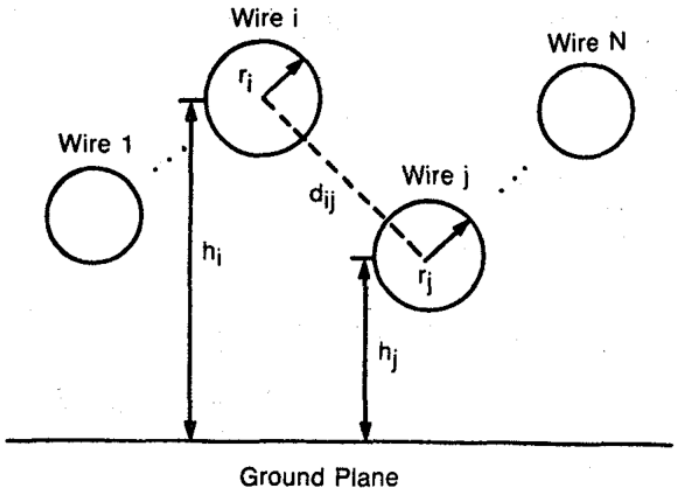


Figure 1.4.: Cross secitonal geomety of n-wire TL above a conducting ground plane [3].

line impedance and inductive coupling coefficients are calculated from the geometrical configuration of the wire cross-section. A TL model is used to describe the cable harness over a conducting ground plane. The TL model is described in Sec. 3.

For the TL model the per-unit-length inductance matrix **L** and capacitance matrix **C** must be calculated from the cable harness geometry. The calculation for wires above a conducting ground plane is described in Sec. 3.4.2.

Since [3] describes the injection and monitoring probe as sole inductive coupling, it is necessary to calculate the mutual inductances between the probe and the wires and also between the wires. Therefore [3] modelled the portion of the cable harness that is inside the injection or monitor probe as wires enclosed in a circular conducting shield to calculate the per-unit-length parameters. In this configuration the circular shield acts as reference potential as described in Sec. 3.4.3

The coupling of the injection probe and each wire of the multiwire harness is approximated as transformer whereas the probe is the primary and the wires form multiple secondary windings of the transformer as shown in Fig. 1.6,

where $v_\mathrm{p}$ and $z_\mathrm{p}$ are the probe voltage and impedance respectively, $L_\mathrm{pp}$ is the probe self inductance which is coupled by the mutual inductance $M_\mathrm{ip}$ to the wire self inductances $L_\mathrm{ii}$. This is further simplified to a Thevenin source (Fig. 1.7, voltage source and impedance series circuit) where the inductive couplings are substituted into the voltage source $V_s$ and the complex impedance $Z_s$. The monitor probe uses the same equivalent circuit with the exception that the voltage source equals zero.

With all components of Fig. 1.8 the solution is determined by calculating the impedance at the terminals of the voltage source $V_\mathrm{s}$ and hence calculate line currents injected into the wiring harness. With the line currents it is possible to calculate the forward travelling voltage waves in every wire on the three TLs between the left-end load and the injection probe, injection probe and monitoring probe and monitoring probe and DUT on the right end. The line current at any point of the TL can now be obtained with the equations in [3]. The bulk current as measured by the monitoring probe corresponds to the vector sum of the line currents at any given point.

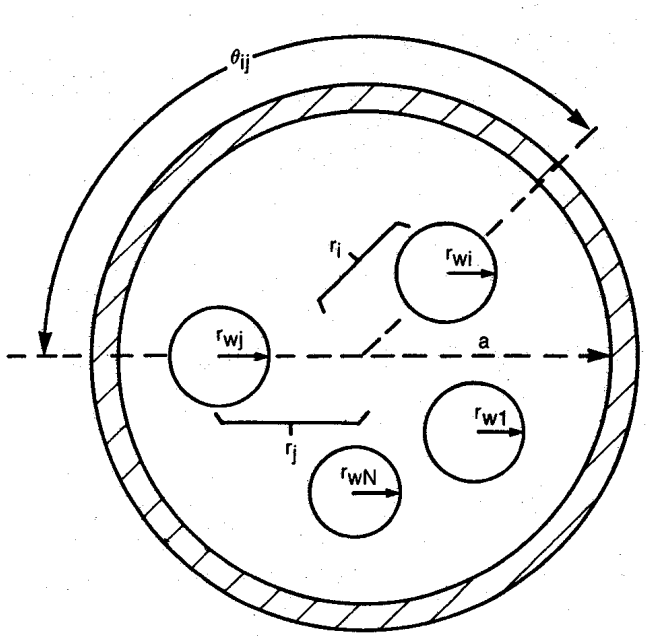


Fig. 5 Cross sectional geometry of n-wire transmission line inside injection or monitor probe windows.

Figure 1.5.: Cross section geometry of n-wire TL inside injection or measurement probe [3].

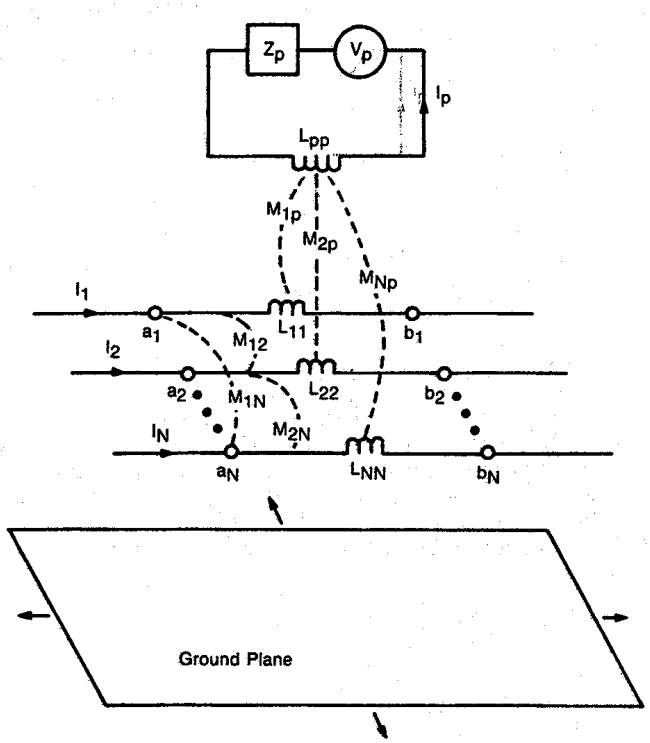


Fig. 3 Injection and monitor probe networks. For the monitor probe network
$V_p$ = 0.

Figure 1.6.: Equivalent circuit for the injection and measurement probe. For the measurement probe the source is Vp=0 [3].

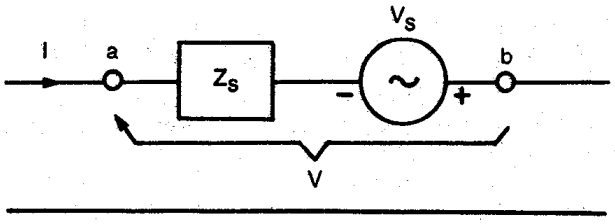


Fig. 4 Equivalent circuit for injection and monitor probe networks ($V_s$ = 0 for monitor network).

Figure 1.7.: Simplified equivalent circuit for injection and measurement probe networks (Vs=0 for measurement probe) [3].

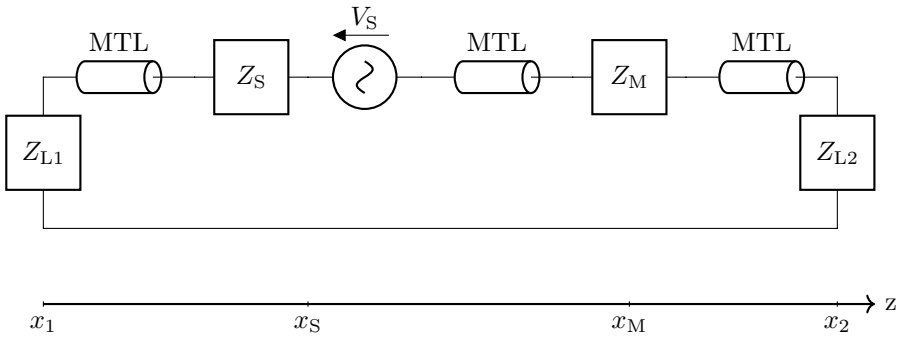


Figure 1.8.: BCI Model of Sultan.

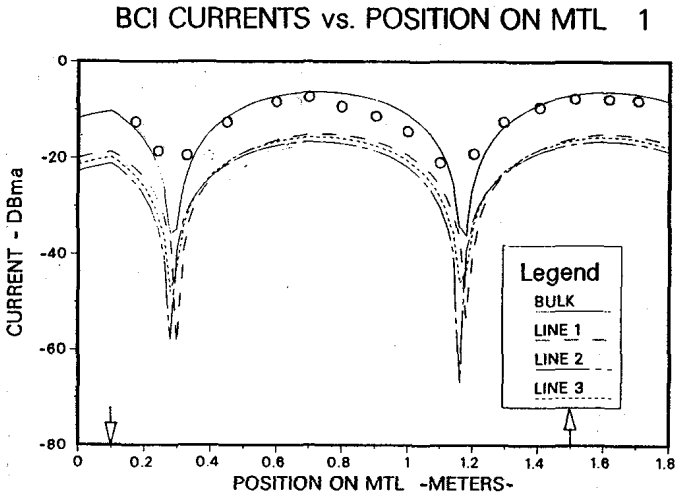


Fig. 8a Effect of injection probe position. Probe at 0.1 meter.

Figure 1.9.: Current distribution along a 1.8 m line, 6 cm above a conducting ground plane and the injection probe position at 0.1 meter. The utilized frequency is not mentioned. [3]

Fig. 1.9 shows the current magnitude and distribution on the wiring harness whereas the open circles are actual measurements of the bulk current and the continuous lines are calculated values. The ordinate shows the current in each line and the bulk current in dB mA and the abscissa shows the position on the line whereas the arrow pointing down shows the position of the injection probe and the arrow pointing up shows the position of the measurement probe. One can see that the calculated and measured values for the bulk current match fairly well.

The paper "Circuit Modeling of Injection Probes for Bulk Current Injection" from Grassi et al. [4] presents two different approaches to modelling of BCI Probes. The first modelling approach relies on scattering parameter measurements in a well known test fixture and in the further course is called *implicit model*. The second modelling approach relies on the measurement of the probe input impedance and is called *explicit model*. Both the implicit and explicit models result in equivalent lumped-Pi circuit structures.

The test fixture necessary for the *implicit model* is basically a single wire between to sheet metal plates where the connectors are mounted. The injection probe mounts on this wire. The probe and the fixture form a three-port. The three-port scattering parameters are measured. This passive three-port is transformed into an active two-port by modelling the RF-source at the probe-port as an non-ideal voltage source. This active two-port is now converted to chain parameter representation and decomposed into the chain connection of the connector, fixture and wire on each side and the active probe in the middle, as shown in Fig. 1.10.

The probe two-port is extracted by de-embedding and a lumped-Pi circuit model is calculated from it, depicted in Fig. 1.11. It is worth noting that this so called *implicit model* of the injection probe is solely created from the scattering parameter measurements.

The *explicit model* should represent the physical and circuit structure of the probe on the conductor. The coupling is described as inductive between the probe and wire inductance like in [3], although including frequency dependent inductances in the probe and fixture circuit and hence a frequency dependent mutual inductance shown in Fig. 1.12.

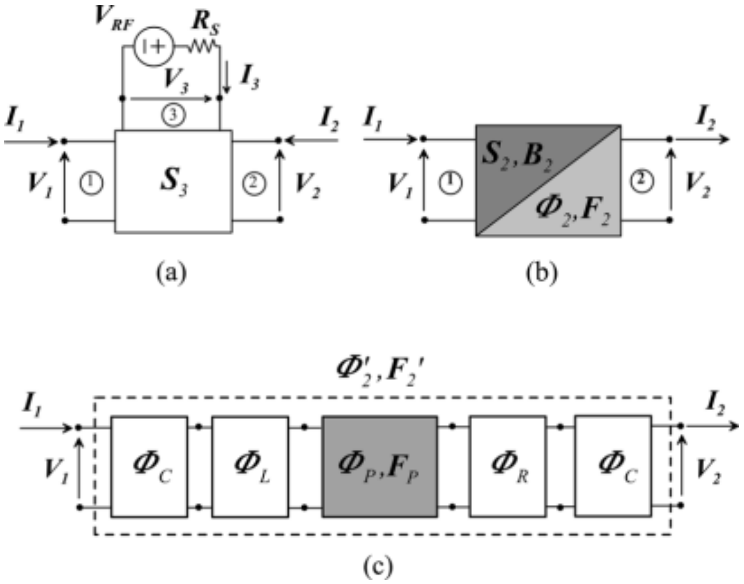


Figure 1.10.: Passive three-port of the probe on the test fixture, whereas the probe is loaded by the RF source represented by an Thévenin source (a), active two port (b) and chain parameter representation for decoposition (c) [4].

Both models match the measurements quite well but, due to the use of frequency dependent values in both models, are problematic for the use in standard circuit simulators.

In [5] Lafon et al. proposed a model for the injection probe that is suited for the use in circuit simulators. The model is based on measurements of the reflection coefficient $S_{11}$ of the injection probe. A model based on the physical structure of the probe similar to the *explicit model* before. The model consists of two parts, the typ-N connector and the loop model whereas loop

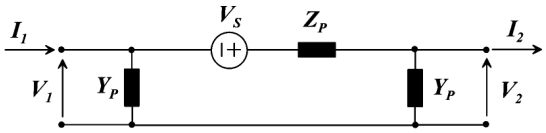


Figure 1.11.: Resulting lumped-Pi model on a single conductor form implicit modelling approach [4].

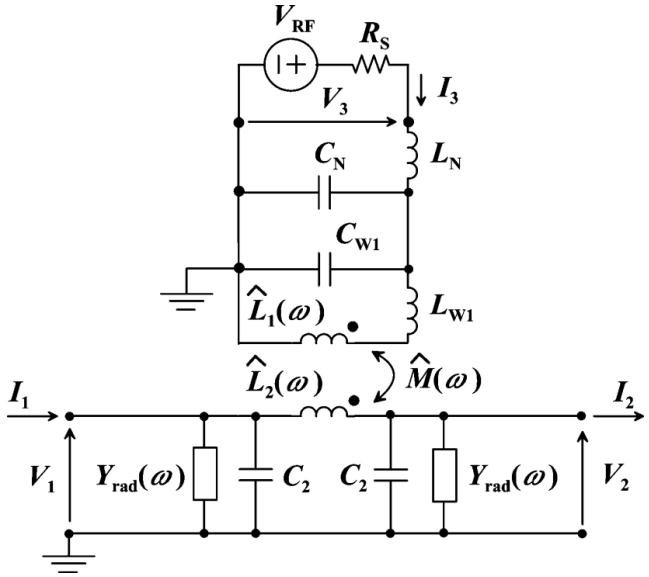


Figure 1.12.: Explicit circuit model for the injection clamp on a single conductor [4].

denotes the primary winding and the ferrite core of the injection probe.

The model uses frequency dependent resistances to achieve good correlation with the measurements.

A model for the utilized test fixture was created with the emphasis on differentiating between the coupled and non-coupled parts of the fixture, shown in Fig. 1.15. The non-coupled part including the connectors would resemble the fixture without the injection probe mounted on it. This is done by measurements of the test fixture with and without the probe, whereby the probe input was left open, to only measure the influence of the ferrite core on the fixture.

To determine the coupled part [5] presumably used chain-parameters to describe the parts of the test fixture, shown in Fig. 1.15, as series of two-port networks. The unknown coupled part of the test fixture was extracted by de-embedding of the measurements with the known structures (networks).

In this work capacitive coupling between the probe and the wires is neglected. Mutual inductive coupling between the probe main inductance and the

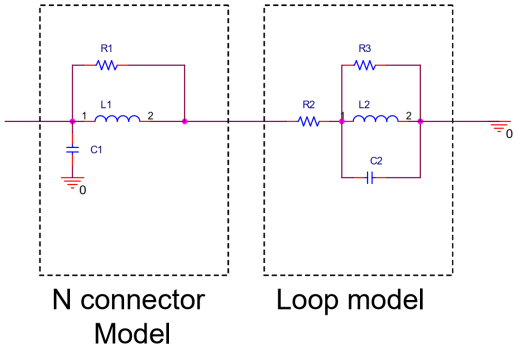


Figure 1.13.: Equivalent model of the injection probe [5].

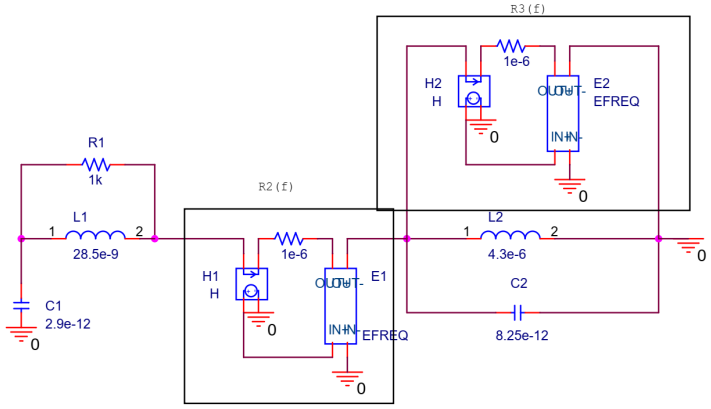


Figure 1.14.: Final probe model with frequency dependent resistance models for $R2$ and $R3$ [5].

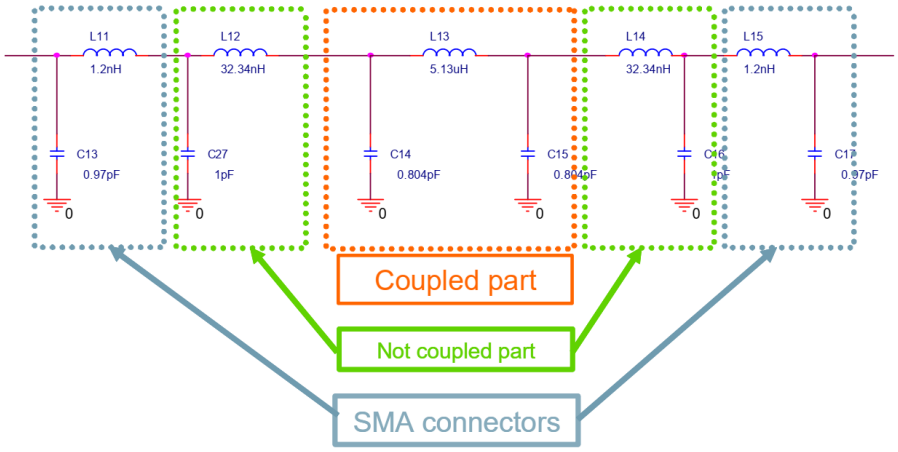


Figure 1.15.: Equivalent circuit representation for the test fixture loaded with the open circuit injection probe [5].

fixtures coupled part is regarded as main coupling mechanism.

The model is validated until 500 MHz from there on until 1 GHz the model shows deviations of 10 dB. Also for every change of the cable harness the coupled part (capacitance, mutual inductance) has to be determined.

# 2. Bulk Current Injection Immunity Test

The BCI test is a method to test the immunity of electronic devices with an attached cable harness. The method is applied in the international standard ISO 11452 Part 4 [2] which scope is the immunity of electronic devices in passenger cars and commercial vehicles.

The international standard states the following: "The bulk current injection (BCI) test method is based on current injection into the wiring harness using a current probe as transformer where the harness forms the secondary winding." [2]

## 2.1. Setup

The BCI test after ISO 11452-4 [2] is conducted in an shielded enclosure where the DUT with its cable harness and attached equipment is placed on an insulating material, with low $\epsilon_r$, 50 mm over a conducting ground plane. Distances to other equipment or the edge of the ground plane are given in the standard the positions of the injection probe and the current measuring probe, on the harness, are also specified in the standard.

### 2.1.1. Injection Probe

The injection probe is a toroidal ferrite core with a copper winding on it. This assembly is inside an aluminium housing. The copper winding goes from the connector around the ferrite core to the aluminium housing which itself is connected to the reference potential of the connector. The probe housing

Figure 2.1.: Test setup for BCI substitution method after ISO 11452-4:2011. This photo was taken at the EMC Lab of the Institute of Electronics at TU Graz.

| **Condition** | **Value** |
|---|---|
| BCI test method | 1 to 400 MHz |
| Tubular wave coupler (TWC) test method | 400 to 3 GHz |
| Test temperature | $23 \pm 5$ °C |
| Supply Voltage | $13.5 \pm 0.5$ V (12 V systems)<br>$27 \pm 1$ V (24 V systems)<br>Ohter values shall be recorded |
| Modulation | CW: 0.01 MHz to 18 GHz<br>AM: 0.01 MHz to 800 MHz (1kHz at 80%)<br>PM: 800 MHz to 18 GHz |
| Dwell time | min. 1 s (response time to control the DUT |
| Frequency step sizes | Table ISO 11452-1:2005 |
| Definition of test severity levels | Table 2.7 |
| Test signal quality | Amplifier harmonics content (ISO 11452-1:2005) |

Table 2.1.: General BCI test conditions and values [2], [6].

and ferrite core are split to allow mounting on a cable harness. Fig. 2.2 shows an opened injection probe. The injection probe acts as a transformer during BCI tests. Whereas the injection probe forms the primary side of a transformer, the ferrite corresponds to the iron core of a transformer and guides the magnetic field and the harness inside the injection probe forms the secondary winding. The aluminium housing has a slit on the inside to avoid eddy currents.


Figure 2.2.: BCI Probe [7].

### 2.1.2. Measurement Probe

The measurement probe is in construction and principle similar to the injection probe but smaller and for less power.

### 2.1.3. Calibration Fixture

The calibration fixture as shown in Fig. 2.3 is used to calibrate the injection fixture before a BCI test.

### 2.1.4. Wire Harness

The wiring harness for the BCI test is not specified in the standard and can be different depending on purpose and requirements. Automotive cable

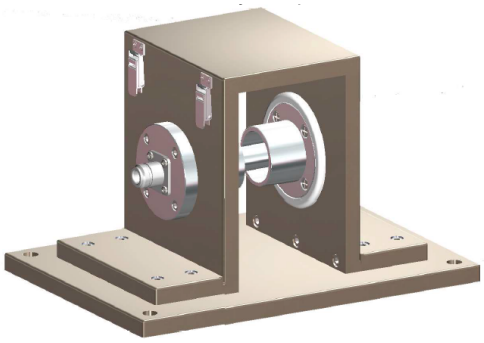

Figure 2.3.: Depiction of a calibration fixture for a BCI probe from [8].

harnesses are typically multiple branches of different length. Shielded wires are avoided to reduce costs.

### 2.1.5. Substitution Method

The *substitution method* applies a previously in calibration determined forward power to the injection probe.

For the calibration the injection probe is clamped on the calibration fixture, as shown in Fig. 2.4. The fixture is on one side terminated with a 50 Ω load and on the other side with a 50 Ω current sensor. During the calibration run, the forward power is adjusted so that the measured current reaches a predefined test severity level as depicted in Fig. 2.7 and Tab. 2.2. The forward power $P_{\text{calibration}}$ necessary to achieve the current for the specified test severity level is recorded.

For the immunity test the DUT or equipment under test (EUT) together with the cable harness and all necessary equipment is installed on the test bench with the respective distances as in [2], as shown in Fig. 2.5. The injection probe is clamped on the harness at the position specified in the standard. For the test the prerecorded forward power curve is applied to the injection probe. The use of a current measurement probe is optional because it is not necessary in this test but it can be of interest to measure the actual bulk current. The cable harness and termination impedances on both sides of the

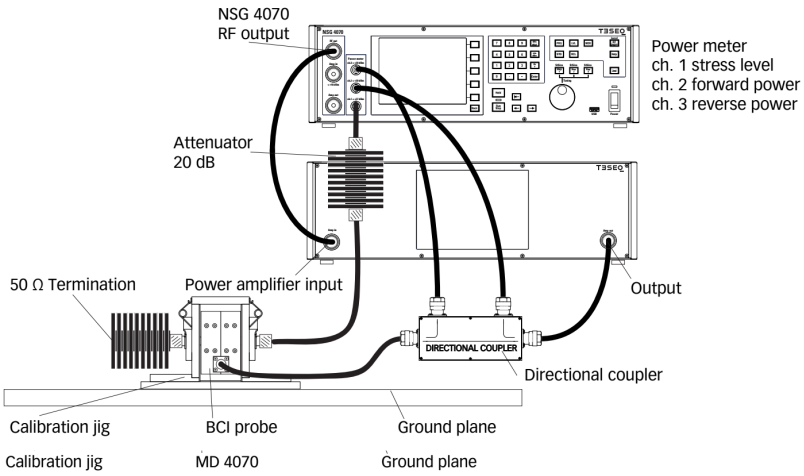


Figure 2.4.: Injection Probe clamped on calibration fixture with termination load and power-meter attached [9].

injection probe have a significant influence on the bulk current and certainly deviate from the calibration set-up. During the test the forward power for a frequency step is applied and the operation of the DUT is monitored. The DUT passes the test successfully if it keeps working normally during the entire test.

### 2.1.6. Closed-Loop Method

With the *closed-loop method* the injected bulk current is continuously measured during the test and the forward power can be adjusted within certain limits.

The calibration power $P_{\text{calibration}}$ is determined in the same way as for the substitution method. With that, the maximum forward power limit for continuous wave test signals is defined in [2] as

$$P_{\text{CWlimit}} = k \cdot P_{\text{calibration}} \,, \tag{2.1}$$

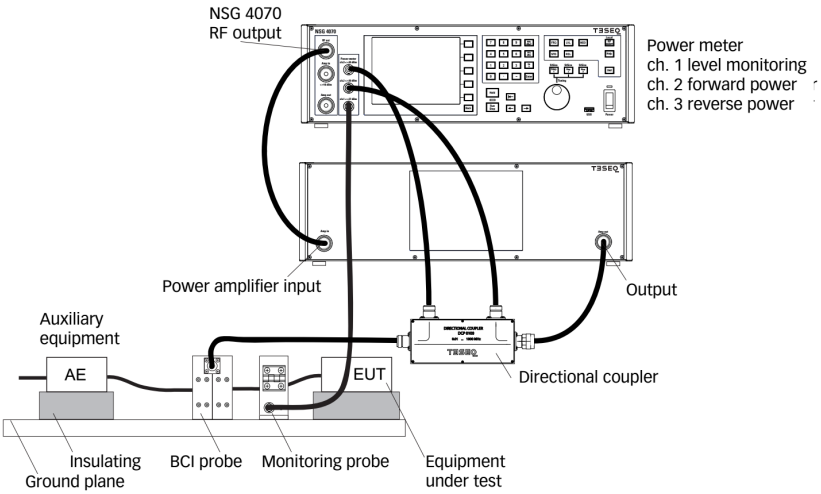


Figure 2.5.: BCI test applying the substitution/closed-loop method [9].

where $P_{\text{calibration}}$ is the in calibration recorded forward power to reach a predefined severity level and $k = 4$ unless otherwise specified.

During the test the bulk current is measured by a monitoring probe which is clamped on the harness close to the DUT. For the test the forward power is increased, starting from the calibration power, until it reaches the power limit or the bulk current reaches the specified test level. In case the DUT fails the achieved forward power and bulk current are recorded and the test is continued at the next frequency step.

### 2.1.7. Test Signal

The standard [6] lists three modulation techniques for test signals, continuous wave (CW), amplitude modulation (AM) and pulse width modulation (PWM) as depicted in Fig. 2.6. This work only regards CW test signals.

The test severity levels, given in Tab. 2.2 and Fig. 2.7, describe the values for the bulk current that must be reached during calibration of the BCI test. These current levels must be achieved in calibration only, because the

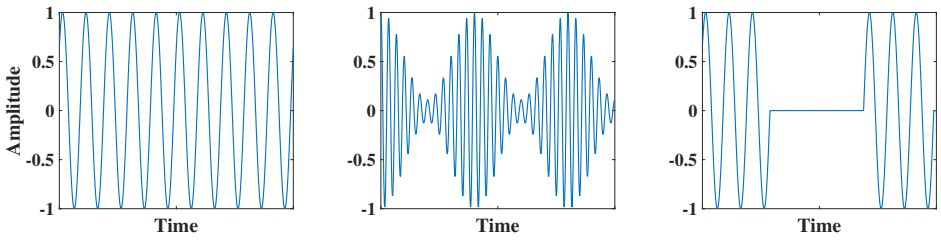


(a) (b) (c)

Figure 2.6.: The test signal modulation can be chosen as (a) un-modulated continuous sine wave, (b) sinusoidal test signal amplitude modulated with 1kHz sinusoidal or (c) pulse width modulation [6].

| **Frequency band** (MHz) | **Test level I** (mA) | **Test level II** (mA) | **Test level III** (mA) | **Test level IV** (mA) |
|---|---|---|---|---|
| 1 to 3 | $60 \cdot F_{(MHz)}/3$ | $100 \cdot F_{(MHz)}/3$ | $150 \cdot F_{(MHz)}/3$ | $200 \cdot F_{(MHz)}/3$ |
| 3 to 200 | 60 | 100 | 150 | 200 |
| 200 to 400 | $60 \cdot 200/F_{(MHz)}$ | $100 \cdot 200/F_{(MHz)}$ | $150 \cdot 200/F_{(MHz)}$ | $200 \cdot 200/F_{(MHz)}$ |

Table 2.2.: Test severity levels and frequency bands as stated in [2]

actual BCI test methods are based upon the forward power determined by calibration of the injection probe on the calibration fixture.

## 2.2. Influence of Probe Position, Harness Length and Load Impedance

In [10] Sato describes the influence of probe position, harness length and load impedance on the injected current by a BCI test. The effects were demonstrated in reference to a simplified simulation model based on the test shown in Fig. 2.8. The simulation model consists of a Thévenin source coupled via an ideal transformer to the harness which is represented by lossless 50 Ω TL on either side. The characteristic impedance of the TL is 50 Ω for matching and to allow an isolated view on each of the discussed effects. Be aware that under test conditions the characteristic impedance of the harness is often not known and impedance matching is not possible.

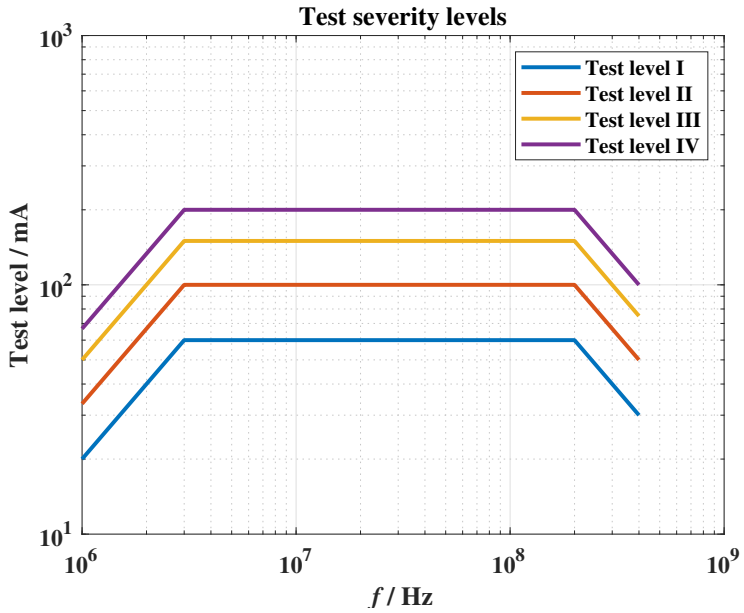


Figure 2.7.: Test severity levels in mA over frequency as depicted in [2].

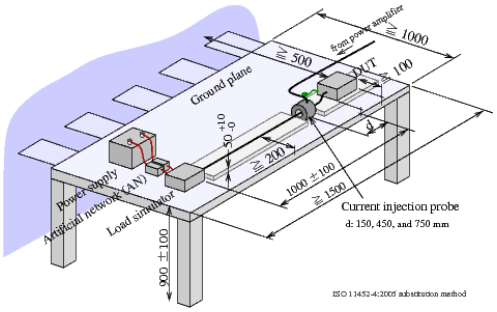


Figure 2.8.: Test setup for substitution method after ISO 11452-4:2011 with measurements [10].

### 2.2.1. Probe Position

In the first example from [10] the impedance at the DUT is 50 Ω and 0 Ω at the load side, as shown in Fig. 2.9 on the right. The probe's position from the DUT $d$ is changed between 150, 450 and 750 mm. When the frequency of the test signal approaches values of $L - d = \lambda/4$ the TL on the load side acts as a *quater-wave impedance transformer* and the *short* on the load side is transformed to an *open* and the injection current will become low. These resonant frequencies depend on the probe position and the wave length for the specific TL.

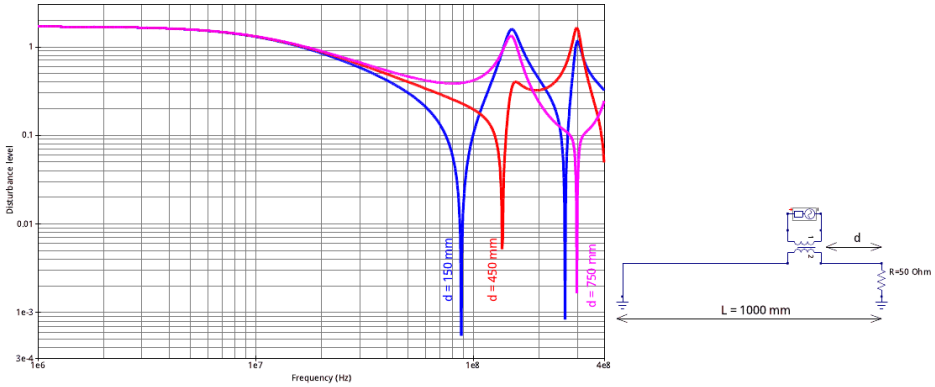


Figure 2.9.: Disturbance levels for different probe positions $d$ at overall harness length $L$ of 1 m as shown in the circuit on the right [10].

We can see the prior described effect in the plot in Fig. 2.9. At probe position $d = 150$ mm the TL on the load side is $L - d = 850$ mm. 850 mm equals a quarter of the wavelength at 88 MHz which coincides with the first minimum of the curve. As previously explained the TL works at that specific frequency as a quarter-wave transformer and the load impedance at the injection point will appear high and therefore prevent current injection. The second minimum of the blue curve appears at three times the frequency of the first minimum. This can be seen as adding full rotations in the smith diagram and therefore occur at odd multiples of the fundamental frequency. The same happens for $L - d = 550$ mm at 136 MHz and for $L - d = 250$ mm at 300 MHz. Fig. 2.10 depicts the same for a harness length of 2 m.

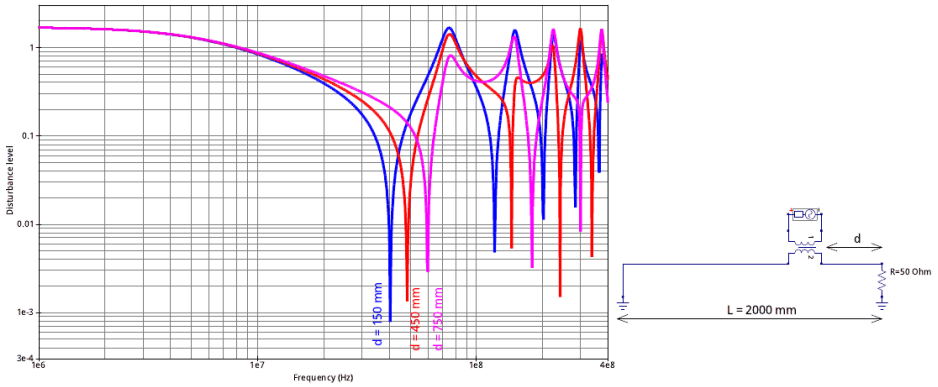


Figure 2.10.: Disturbance levels for different probe positions $d$ at overall harness length of 2 m as shown in the circuit on the right [10].

### 2.2.2. Load Simulator Impedance

For low frequencies the injected current flows through the harness, to the DUT, through the ground plane to the load simulator $Z_{\text{load}}$, and the harness again back to the probe. Therefore the impedance of the load simulator is very important for the disturbance levels as shown in Fig. 2.11. Terminating the lines with capacitors, as depicted in Fig. 2.12, can be a solution to these reduced disturbance levels.

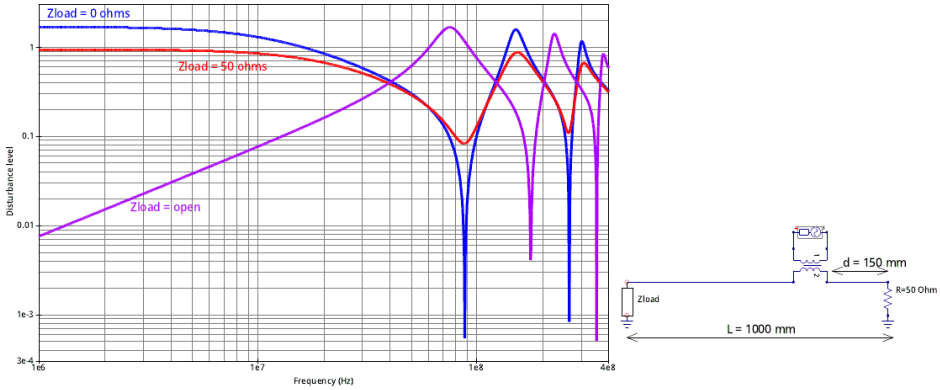


Figure 2.11.: Disturbance levels for different load impedances Zload for 1 m harness length and probe position $d = 150$ mm [10].

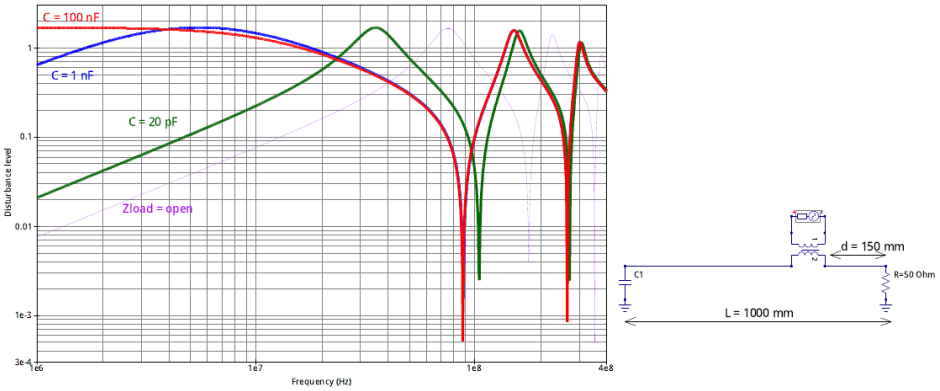


Figure 2.12.: Disturbance levels for different capacitive load impedances C1 for 1 m harness length and probe position $d = 150\,\text{mm}$ [10].

### 2.2.3. DUT Grounding

The influence of a grounding wire to connect the DUT to the ground plane locally is shown in Fig. 2.13. The capacitance of the DUT to the ground plane and the inductance of the wire are represented by a LC parallel circuit. At the resonance frequency this LC circuit is high impedance and prevents current injection. The resonance frequency in the example circuit in Fig. 2.13 is $f_0 = 1/(2\pi\sqrt{LC}) = 79.5\,\text{MHz}$ as in the plot, where $C$ and $L$ were 20 pF and 200 nH respectively.

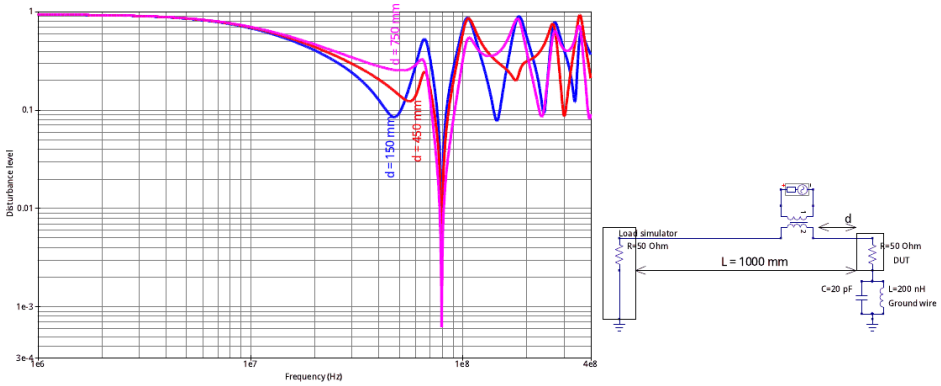


Figure 2.13.: Influence of the DUT ground wire on the disturbance levels for 1 m harness length and probe position $d = 150$ mm [10].

# 3. Transmission Line

Transmission lines are used to transfer digital or analog signals between two points. The influence of TLs on signal integrity increases with frequency. Therefore it is necessary to now the TL in detail. Transmission lines in RF can be divided into two classes, wave-guides and multi-conductor cables. In this chapter the sole focus will be on multi-conductor cables. We will start with a recapitulation of TL fundamentals from [11].

## 3.1. Transmission Line Theory

As described in [11], the voltage and current waves travelling along a pair of conductors form EM fields around the conductors. The energy stored in those fields can be assigned to a capacitance and inductance per unit of length distributed over the line. Similarly the losses can be attributed to a series- and shunt-resistances. Fig. 3.1 depicts a TL of length $\mathscr{L}$ and Fig. 3.2 shows a segment of length $\Delta z$ of the TL. The distributed per-unit-length parameters are denoted with a prime (eg.: $L'$).

### 3.1.1. Telegrapher's Equation

By applying Kirchhoff's voltage and current laws to the circuit in Fig. 3.2 we acquire two first order differential equations, describing a short TL segment also known as telegrapher's equations:

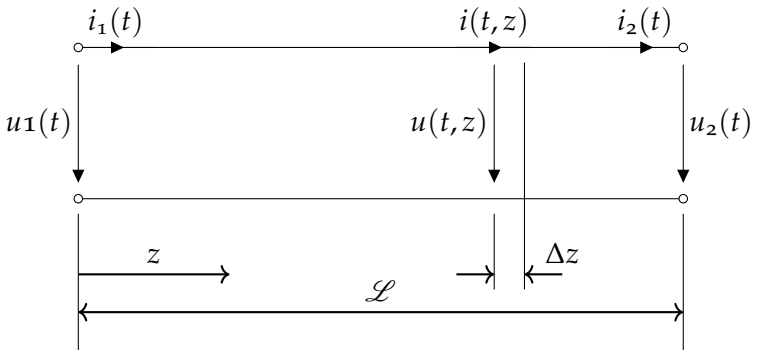


Figure 3.1.: Illustration of a two-wire TL.

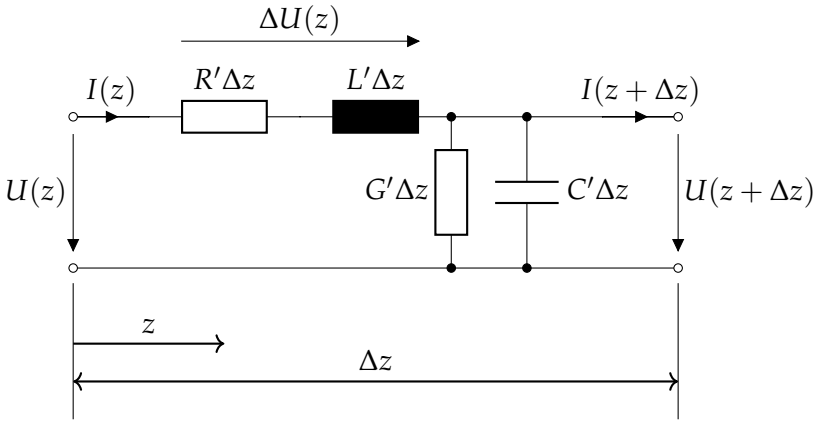


Figure 3.2.: Equivalent circuit diagram of a two-wire TL segment in difference depiction.

$$-\frac{dU(z)}{dz} = (R' + j\omega L') \cdot I(z), \tag{3.1}$$

$$-\frac{dI(z)}{dz} = (G' + j\omega C') \cdot U(z). \tag{3.2}$$

The Eqs. (3.1, 3.2) can be combined to form a second order differential equation:

$$\frac{d^2U(z)}{dz^2} - (G' + j\omega C') \cdot (R' + j\omega L') \cdot U(x) = 0. \tag{3.3}$$

At this point it is necessary to introduce the *propagation constant* $\gamma$ which is defined as:

$$\gamma = \alpha + j\beta = \sqrt{(G' + j\omega C') \cdot (R' + j\omega L')}, \tag{3.4}$$

where $\alpha$ is the *attenuation constant* and $\beta$ is refered to as *phase constant*. This simplifies Eq. 3.3 to:

$$\frac{d^2U(z)}{dz^2} - \gamma^2 \cdot U(z) = 0. \tag{3.5}$$

The general solution for this homogeneous second order differential equation is:

$$U(z) = U_p\, e^{-\gamma z} + U_r\, e^{\gamma z}, \tag{3.6}$$

where the $U_p\, e^{-\gamma z}$ term represents the voltage wave propagating in positive $z$ direction, as indicated by the $p$ index for *propagation*, and the $U_r\, e^{\gamma z}$ term propagates in the negative $z$ direction, as indicated by the $r$ index for *reflection*. Similarly the current wave on the line is expressed as:

$$I(z) = \sqrt{\frac{G' + j\omega C'}{R' + j\omega L'}} \cdot (U_p e^{-\gamma z} - U_r e^{\gamma z}), \tag{3.7}$$

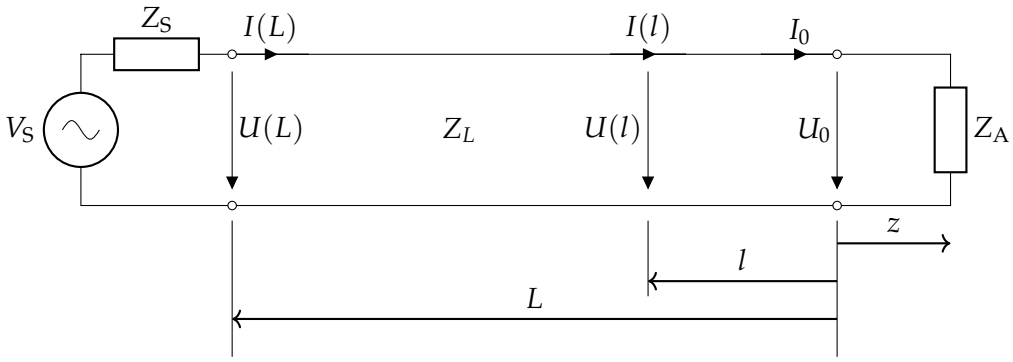


Figure 3.3.: Illustration of a two-wire TL.

which leads to the *characteristic impedance* $Z_L$ of a TL and is defined as:

$$Z_L = \sqrt{\frac{R' + j\omega L'}{G' + j\omega C'}}. \tag{3.8}$$

### Solution of $U_p$ and $U_r$

The integration constants $U_p$ and $U_r$ are determined by the boundary conditions at the beginning and the end of the TL. Furthermore the current $I(l)$ and voltage $U(l)$ on the line can be calculated from the current $I_0$ and voltage $U_0$ at the termination resistor $Z_A$. To define the position on the line the auxiliary variable $l = -z$ is used.

At the coordinate origin $l = 0$, Eq. 3.6 and 3.7 simplify to:

$$U(l = 0) = U_0 = U_p + U_r, \tag{3.9}$$
$$I(l = 0) \cdot Z_L = I_0 \cdot Z_L = (U_p - U_r). \tag{3.10}$$

Applying the elimination method, for $U_r$ and $U_p$, on Eqs. 3.9 and 3.10 gives:

$$U_p = 1/2(U_0 + I_0 \cdot Z_L) \tag{3.11}$$
$$U_r = 1/2(U_0 - I_0 \cdot Z_L) \tag{3.12}$$

Inserting in Eqs. 3.6 and 3.7 leads to:

$$U(l) = 1/2(U_0 + I_0 \cdot Z_L)\ e^{\gamma l} + 1/2(U_0 - I_0 \cdot Z_L)\ e^{-\gamma l},$$
$$I(l) \cdot Z_L = 1/2(U_0 + I_0 \cdot Z_L)e^{\gamma l} - 1/2(U_0 - I_0 \cdot Z_L)e^{-\gamma l},$$

Using the following conversions:

$$\sinh(\gamma l) = 1/2(e^{\gamma l} - e^{-\gamma l})$$
$$\textit{and} \quad \cosh(\gamma l) = 1/2(e^{\gamma l} + e^{-\gamma l})$$

Gives the system of linear equations in Eq. 3.13 which is also the A-Parameter representation.

$$\begin{pmatrix} U(l) \\ I(l) \end{pmatrix} = \begin{pmatrix} \cosh(\gamma l) & Z_L \sinh(\gamma l) \\ 1/Z_L \sinh(\gamma l) & \cosh(\gamma l) \end{pmatrix} \begin{pmatrix} U_0 \\ I_0 \end{pmatrix} \tag{3.13}$$

This matrix can be converted to S-parameters as explained in Sec. 3.7, by applying $l = L$ and $Z_S = Z_L = Z_A$, as depicted in Fig. 3.3. The equal impedances of source, load and characteristic impedance of the transmission line is called matching.

$$[S] = \begin{pmatrix} 0 & e^{-\gamma l} \\ e^{-\gamma l} & 0 \end{pmatrix} \tag{3.14}$$

Because of matching the reflection coefficients, the elements in the main diagonal of the matrix, are zero.

### The low-loss Line

The low-loss line describes a TL where both the conductor and dielectric losses are small, $R' \ll \omega L'$ and $G' \ll \omega C'$. This assumption is very close to reality and leads to some simplifications for the *propagation constant* $\gamma$, as shown in [11]

$$\gamma = \alpha + j\beta = \sqrt{(G' + j\omega C') \cdot (R' + j\omega L')} \tag{3.15}$$

$$\gamma = \sqrt{j\omega C' \left(1 + \frac{G'}{j\omega C'}\right) j\omega L' \left(1 + \frac{R'}{j\omega L'}\right)} \tag{3.16}$$

$$\gamma \approx j\omega\sqrt{C'L'}\sqrt{1 + \frac{G'}{j\omega C'} + \frac{R'}{j\omega L'}} \tag{3.17}$$

$$\gamma \approx j\omega\sqrt{C'L'}\left(1 + \frac{G'}{j\omega 2C'} + \frac{R'}{j\omega 2L'}\right) \tag{3.18}$$

$$\gamma \approx \underbrace{j\omega\sqrt{C'L'}}_{=j\beta} + \underbrace{\frac{G'}{2}\sqrt{\frac{L'}{C'}} + \frac{R'}{2}\sqrt{\frac{C'}{L'}}}_{=\alpha}. \tag{3.19}$$

With this simplifications the *characteristic impedance* $Z_L$ adopts the same form as in the loss-less case and therefore shows that for low-losses $Z_L$ can be approximated as real values.

$$Z_L = \sqrt{\frac{R' + j\omega L'}{G' + j\omega C'}} = \sqrt{\frac{j\omega L'}{j\omega C'}} \cdot \sqrt{\left(1 + \frac{R'}{j\omega L'}\right) / \left(1 + \frac{G'}{j\omega C'}\right)} \approx \sqrt{\frac{L'}{C'}} \tag{3.20}$$

### The loss-less Line

For the loss-less line the quantities $R'$ and $G'$ are zero. Therefore $\alpha$ is also zero and $\gamma$ becomes $\gamma = j\beta$. Eqs. 3.13 and 3.14 simplify to:

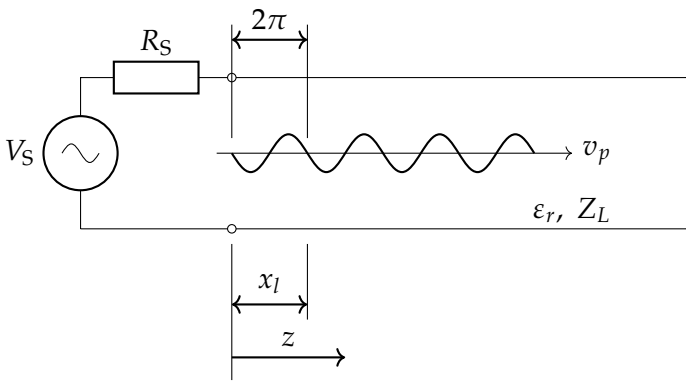


Figure 3.4.: Wave propagating on TL.

$$\begin{pmatrix} U(l) \\ I(l) \end{pmatrix} = \begin{pmatrix} \cos(\beta l) & jZ_L \sin(\beta l) \\ j^1/_{Z_L} \sin(\beta l) & \cosh(\beta l) \end{pmatrix} \begin{pmatrix} U_0 \\ I_0 \end{pmatrix} \tag{3.21}$$

$$[S] = \begin{pmatrix} 0 & e^{-j\beta l} \\ e^{-j\beta l} & 0 \end{pmatrix} \tag{3.22}$$

### Time Delay, Velocity of Propagation, Group Delay

Fig. 3.4 shows a TL of infinite length, to avoid reflections in this example. The wave excited by the generator propagates from $z = 0$ in positive $z$ direction. At $z = 0$, or any other point, the wave oscillates with frequency $f$. The phase of point $z = 0$ propagates with *phase velocity* $v_p$ and appears delayed by the time $t_l$ at point $x_l$.

In free-space ($\mu = \mu_0$, $\varepsilon = \varepsilon_0$) when there is no material between the conductors of the TL the *phase velocity* $v_p$ can be expressed as

$$v_p = \frac{x_l}{t_l} = c_0 = \lambda f = \frac{1}{\sqrt{\mu_0 \varepsilon_0}} \tag{3.23}$$

where $t_l$ is the time it takes the wave to travel the distance $x_l$, $c_0$ is the *speed of light*, $\lambda$ is the *wavelength* which in Fig. 3.4 corresponds to the length $x_l$

and $f$ is the *frequency* of the signal. In an application where some material is between the conductors, like for example an coaxial cable, the *phase velocity* reduces to

$$v_p = \frac{\omega}{\beta} = \frac{1}{\sqrt{L'C'}} = \frac{c}{\sqrt{\mu_r \varepsilon_r}} = \frac{1}{\sqrt{\mu\varepsilon}} \tag{3.24}$$

where $\mu = \mu_0\mu_r$ and $\varepsilon = \varepsilon_0\varepsilon_r$. This reducing factor $VF = {}^1/_{\sqrt{\mu_r\varepsilon_r}}$ is called *velocity factor*. This leads to a shortening of the wavelength by the same factor.

$$\lambda = \frac{v_p}{f} = \frac{c}{\sqrt{\mu_r\varepsilon_r}f} = \frac{2\pi v_p}{\omega} = \frac{2\pi}{\beta} = \frac{1}{f\sqrt{L'C'}}. \tag{3.25}$$

The *time delay* $T_D$ is the duration a wave needs to travel along a line of length $\mathscr{L}$. As already mentioned this time delay depends on the TL.

$$T_D = \frac{\mathscr{L}}{v_p} \tag{3.26}$$

The *group delay* describes how long it takes various frequency components to pass through the system. If the group delay is not constant, because of frequency dependent transmission behaviour (dispersion), the signal gets distorted.

$$\tau_g = -\frac{d\phi(\omega)}{d\omega} = -\frac{d\angle S_{21}}{d\omega} \tag{3.27}$$

The term *electrical length* $E$ is the ratio of the physical length of the conductor to the "shortened" wavelength and is given with a reference frequency at which the wavelength was calculated. The *phase length* $\theta$ is similar but expresses the before mentioned ratio in degrees,

$$E = \frac{\mathscr{L}}{\lambda} \tag{3.28}$$

$$\theta = \frac{\mathscr{L}}{\lambda} \cdot 360° \,, \tag{3.29}$$

where $\mathscr{L}$ is the physical *length* of the TL and $\lambda$ is the *wavelength*.

## 3.2. Coaxial Line

In this section TL parameters are calculated on the basis of a coaxial line, depicted in Fig. 3.5. The parameters of a TL depend mostly on geometry and material except for the frequency dependent internal parameters like internal inductance and resistance.

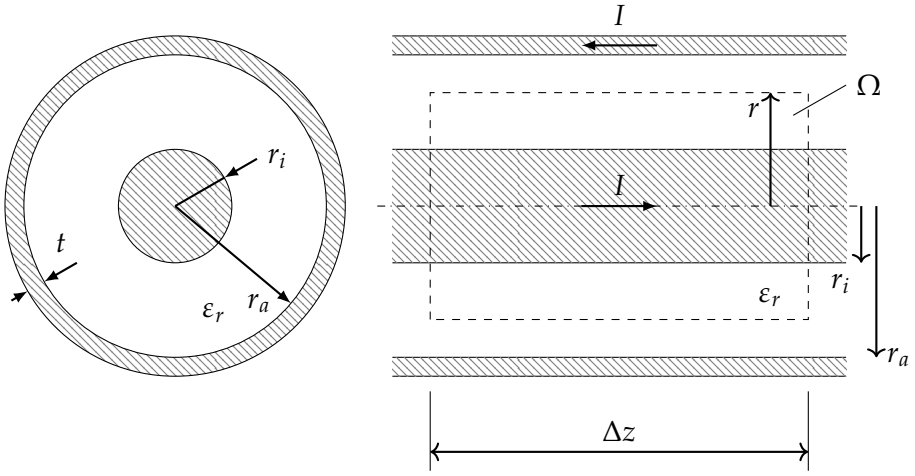


Figure 3.5.: Transversal cross-section of a coaxial TL (a) and longitudinal cross-section (b). Where $r_i$, $r_a$ and $t$ are the inner and outer radius and the thickness of the outer conductor respectively. $\varepsilon_r$ is the permittivity of the material inbetween the conductors and $\Omega$ is the integration volume. The length of the considered line segment is $\Delta z$.

### 3.2.1. Capacitance

The per unit length (p.u.l.) capacitance is calculated by applying a charge to a coaxial cable of 1 m length.

$$Q' = C' \cdot V \tag{3.30}$$

We start by calculating the electrical field in radial direction

$$E_r = \frac{\tau \Delta z}{2\pi\varepsilon} \frac{1}{r} , \tag{3.31}$$

where $\tau$ is an *uniform line charge density*, $\Delta z$ is the *length*, $\varepsilon$ is the *permittivity* of the material between the conductors and $r$ is the *radius* with $r_i \leq r \leq r_a$. The integration region spans the area inbetween the conductors, as depicted in Fig. 3.5. With this we can calculate the voltage between the conductors.

$$V = V_i - V_a = \int_{r_a}^{r_i} \boldsymbol{E}(\boldsymbol{r}) d\boldsymbol{r} = \frac{\tau \Delta z}{2\pi\varepsilon} \ln \frac{r_a}{r_i} \tag{3.32}$$

With Eq. 3.30 and $Q = \tau \cdot \Delta z$ the capacitance is defined as

$$C' = \frac{Q'}{V} = \frac{2\pi\varepsilon}{\ln \frac{r_a}{r_i}} . \tag{3.33}$$

### 3.2.2. Shunt Conductance

The shunt conductance can be calculated from the capacitance

$$G' = \sigma \frac{C'}{\varepsilon} = \frac{2\pi\sigma}{\ln \frac{r_a}{r_i}} , \tag{3.34}$$

where $\sigma$ and $\varepsilon$ are the conductance and permittivity of the material inbetween the conductors respectively. Another approach is by calculating the total

shunt current by integrating the current density around the conductor and then dividing by the potential difference from Eq. 3.32

$$I_{shunt} = \Delta z \int_0^{2\pi} \sigma E_r d\phi = \frac{2\pi\sigma\tau\Delta z}{2\pi\varepsilon}. \tag{3.35}$$

### 3.2.3. Inductance

The inductance of a conductor is a combination of the external and internal inductance

$$L' = L'_{\text{ext}} + L'_{\text{int,ra}} + L'_{\text{int,rb}}\ , \tag{3.36}$$

where the *external inductance* $L'_{\text{ext}}$ is the dominant part and is only dependent on the geometry and material whilst the internal inductance is frequency dependent and can be neglected for higher frequencies.

#### Internal Inductance

The internal inductance is produced by the magnetic flux inside the conductor itself. This flux is due to the current flow in the conductor. Since the current distribution inside the conductor is frequency dependent (skin effect), this internal inductance is only relevant for low frequencies. To determine the *internal inductance* of a non-magnetic circular conductor with uniform current distribution, radius $r_i$ and length of 1 m as depicted in [12], we start by defining the current through a concentric circle with radius $x$ where $x \leq r_i$.

$$I_x = I\frac{\pi x^2}{\pi r_i^2} \tag{3.37}$$

Ampere's law states that summing up the *magnetic field intensity* $H$ along a closed contour corresponds to the current flow through the enclosed area. Therefore we can express the *magnetic field intensity* $H$ at radius $x$ as

$$H_x = \frac{I_x}{2\pi x} = \frac{I}{2\pi r_i^2} x \tag{3.38}$$

and the *magnetic field density* $B$ as

$$B_x = \mu H_x = \frac{\mu_0 I x}{2\pi r_i^2} \tag{3.39}$$

From here we derive the *differential magnetic flux* $d\phi$ through a ring of thickness $dx$.

$$d\phi = B_x dx = \frac{\mu_0 I x}{2\pi r^2} dx \tag{3.40}$$

Since the above expressed flux is not constant over the entire cross-sectional area we have to link the flux to the relative conductor area spanned by a circle of radius $x$.

$$d\lambda = \frac{\pi x^2}{\pi r_i^2} d\phi = \frac{\mu_0 I x^3}{2\pi r_i^4} dx \tag{3.41}$$

The *internal flux linkage* $\lambda_{int}$ is determined by integrating the *differential flux linkage* $d\lambda$ over the radius and thus leads to the *internal inductance* $L'_{int}$.

$$\lambda_{\text{int}} = \int_0^r d\lambda = \frac{\mu_0 I}{8\pi} \tag{3.42}$$

$$L'_{\text{int,ri}} = \frac{\lambda_{\text{int}}}{I} = \frac{\mu}{8\pi} \tag{3.43}$$

The internal inductance of the outer enclosing conductor is expressed by [13] as follows:

$$L'_{\text{int,ra}} = \frac{\mu}{8\pi} \frac{1 - 4\left(\frac{r_a}{r_c}\right)^2 + 3\left(\frac{r_a}{r_c}\right)^3 + 4\left(\frac{r_a}{r_i}\right)^4 \ln\left(\frac{r_c}{r_a}\right)}{\left(1 - \left(\frac{r_a}{r_c}\right)^2\right)^2}\,, \tag{3.44}$$

where $r_i$, $r_a$ are the radii of the inner and outer conductors respectively as depicted in Fig. 3.5 and $r_c = r_b + t$.

### External Inductance

The external inductance describes the magnetic field in the space between the inner and outer conductor

$$H_r = \frac{I}{2\pi y}\,, \tag{3.45}$$

where $I$ is the current in the conductor and $y$ is the radius whereas $r_i \leq y \leq r_a$ holds. We get the magnetix flux density by multiplying with the permeability $\mu$ of the material between the conductors.

$$B_y = \mu H_y = \frac{\mu I}{2\pi y} \tag{3.46}$$

With the *magnetic field density* $B$ we calculate the flux through a ring of thickness $dy$ to obtain the *differential flux*. According to [12] since the total current $I$ is enclosed in the conductor the *differential flux linkage* $d\lambda$ equals the *differential flux* $d\phi$.

$$d\lambda = d\phi = B_y dy = \frac{\mu I}{2\pi y} dy \tag{3.47}$$

The *flux linkage lambda* is aquired by integration from the inner conductor surface to the outer conductor surface.

$$\lambda_{\text{ext}} = \int_{y=r_i}^{r_a} d\lambda = \frac{\mu I}{2\pi} \ln \frac{r_a}{r_i} \tag{3.48}$$

$$L'_{\text{ext}} = \frac{\lambda_{\text{ext}}}{I} = \frac{\mu}{2\pi} \ln \frac{r_a}{r_i} \tag{3.49}$$

### 3.2.4. Resistance

#### Low Frequency Resistance

The low frequency resistance is the resistance of the whole conductor without taking the skin effect into account is given in Eq. 3.2.4, where $\sigma_i$ and $\sigma_a$ are the conductivity of the inner and outer conductor respectively. $A_i$ and $A_a$ are the area of the inner and outer conductor. This assumption proves to be sufficiently accurate up until frequencies at which the *skin depth* $\delta_s$ is still larger than the radius of the conductor.

$$\begin{aligned} R'_{\text{lf}} &= \frac{1}{\sigma_i A_i} + \frac{1}{\sigma_a A_a} \\ &= \frac{1}{\sigma_i r_i^2 \pi} + \frac{1}{\sigma_a \pi [(r_a + t)^2 - r_a^2]} \end{aligned} \tag{3.50}$$

#### High Frequency Resistance

The high frequency resistance $R'_{hf}$ of the coaxial line must be considered above frequencies, where the *skin depth* $\delta_s(f)$ decreases below the radius of the inner conductor $r_i$ or the thickness of the outer conductor $t$ respectively. The skin depth $\delta_s$ is given in Eq. 3.81 in Sec. 3.6.1. The high frequency resistance $R'_{hf}$ is defined as follows:

$$\begin{aligned} R'_{\mathrm{hf}} &= R'_i + R'_a \\ &= \frac{1}{\sigma_i A_i} + \frac{1}{\sigma_a A_a} \\ &\approx \frac{1}{\sigma_i [\pi 2 r_i \delta_s]} + \frac{1}{\sigma_a [\pi 2 r_a \delta_s]} \\ &= \frac{1}{2pi\delta_s} \left[ \frac{1}{\sigma_i r_i} + \frac{1}{\sigma_a r_a} \right] , \end{aligned} \tag{3.51}$$

where $R_i$ and $R_a$ are the resistances for the inner conductor and outer shield respectively, $\sigma_i$ and $\sigma_a$ are the inner and outer conductivities. The approximation used for the area is explained in Eq. 3.82.

## 3.3. Two-Wire Line

In this section the TL parameter of a two-wire line are explained and formulas for the calculation of these parameters are provided. The geometry of the TL is shown in Fig. 3.6.

### 3.3.1. Capacitance

The voltage for the two-wire line is defined as

$$V = \frac{1}{2\pi\varepsilon} \tau \Delta z \ln \frac{d^2}{r_i^2} , \tag{3.52}$$

similarly to the coaxial line we calculate the capacitance with Eq. 3.30 as follows

$$C' = \frac{Q'}{V} = \frac{\pi\varepsilon}{\ln \frac{d}{r_i}}. \tag{3.53}$$

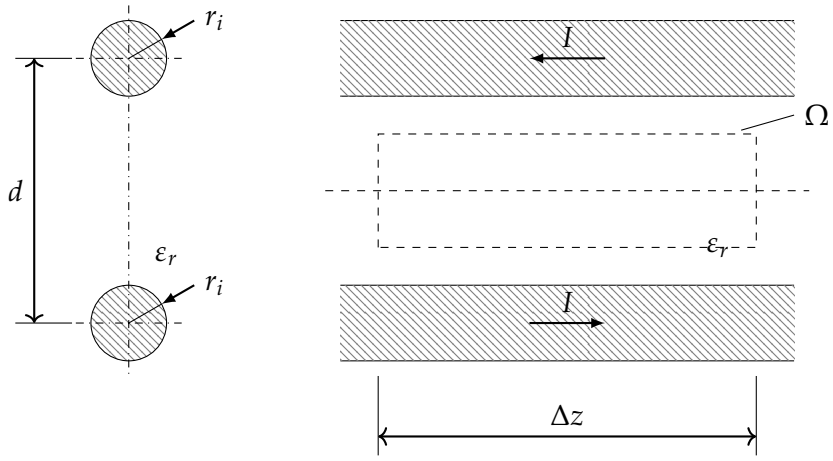


Figure 3.6.: Transversal cross-section of a two-wire TL (a) and longitudinal cross-section (b). Where $r_i$ and $d$ are the radius of the conductors and the distance of the conductors respectively. $\varepsilon_r$ is the permittivity of the material inbetween the conductors and $\Omega$ is the integration volume. The length of the considered line segment is $\Delta z$.

The capacitance can also be derived from the inductance with

$$C' = \frac{\varepsilon_0 \mu_0}{L'} \,, \tag{3.54}$$

as shown in [14], be aware that this gives you only the capacitance in free-space $\varepsilon = \varepsilon_0$ and is only possible with the free-space inductance.

### 3.3.2. Shunt Conductance

As with the coaxial line before the shunt conductance can be calculated from the capacitance as

$$G' = \sigma \frac{C'}{\varepsilon} = \frac{\pi \sigma}{\ln \frac{d}{r_i}} \,. \tag{3.55}$$

### 3.3.3. Inductance

For the calculation we assume two conductors with radius $r_i$, current $I$ in each conductor but in opposing directions and at distance $d$, as depicted in Fig. 3.6. The conductors are at close enough distance for flux linkage to take place in both conductors.

#### Internal Inductance

The internal inductance $L_{\text{int}}$ for each of the two wires is calculated the same way as for the inner conductor of the coaxial-cable shown in Eq. 3.43 in Sec. 3.2.3.

#### External Inductance

To calculate the external inductance we need to calculate the flux linkage $\lambda$ first. Since the magnetic fields of both conductors are affecting each other the flux linkage for each conductor has two components. The flux linkage for one conductor, denoted as $\lambda_A$ consists of the flux produced by conductor $A$ and the flux produced by conductor $B$ linked to conductor $A$. The same holds for the other conductor. With this in mind we define the flux at an arbitrary point $P$ as follows:

$$\lambda_P = \lambda_{AP} + \lambda_{BP} = (\lambda_{AAP} + \lambda_{ABP}) + (\lambda_{BAP} + \lambda_{BBP}) \tag{3.56}$$

where $\lambda_{AP}$ is the flux linkage from conductor $A$ at point $P$, $\lambda_{AAP}$ is the flux linkage from the magnetic field of conductor $A$ on conductor $A$ at point $P$, $\lambda_{ABP}$ is the flux linkage from the field of conductor $B$ on conductor $A$ at point $P$ and alike for $\lambda_{BP}$, $\lambda_{BBP}$ and $\lambda_{BAP}$.

$$\lambda_{\text{AAP}} = \frac{\mu}{2\pi} I \ln \frac{D_{AP}}{r_i}$$
$$\lambda_{\text{BBP}} = \frac{\mu}{2\pi} I \ln \frac{D_{BP}}{r_i}$$

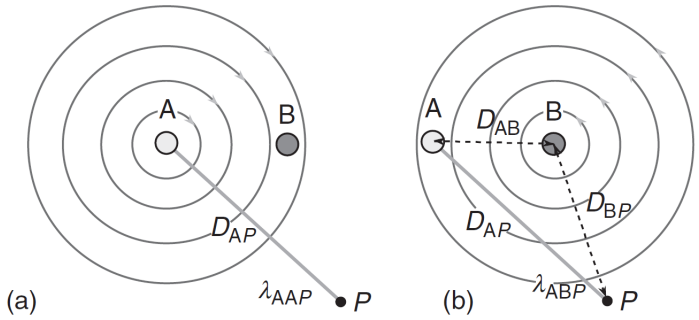


Figure 3.7.: "Flux linkage of (a) conductor $A$ at point $P$ and (b) conductor $B$ on conductor $A$ at point $B$." [12] The current for conductor $A$ goes into the plane and comes out of the plane for conductor $B$. Distance $D_{AB} = D_{BA} = d$.

$$\lambda_{\mathrm{ABP}} = \int_d^{D_{BP}} B_{BP} dP = -\frac{\mu}{2\pi} I \ln \frac{D_{BP}}{d}$$
$$\lambda_{\mathrm{BAP}} = \int_d^{D_{AP}} B_{AP} dP = -\frac{\mu}{2\pi} I \ln \frac{D_{AP}}{d}$$

The magnetic field densities $B_{AP}$ and $B_{BP}$ are the magnetic field densities at point $P$ generated by the current through conductor $A$ and $B$ respectively. The negative sign derives from the opposing current direction to the referred conductor $I_A = -I_B$.

$$\begin{aligned}
\lambda_P =& (\lambda_{AAP} + \lambda_{ABP}) + (\lambda_{BAP} + \lambda_{BBP}) \\
=& \frac{\mu}{2\pi} I \ln \frac{D_{AP}}{r_i} - \frac{\mu}{2\pi} I \ln \frac{D_{AP}}{d} \\
&+ \frac{\mu}{2\pi} I \ln \frac{D_{BP}}{r_i} - \frac{\mu}{2\pi} I \ln \frac{D_{BP}}{d} \\
=& \frac{\mu}{2\pi} I \ln \left( \frac{D_{AP}}{r_i} \frac{d}{D_{AP}} \frac{D_{BP}}{r_i} \frac{d}{D_{BP}} \right) \\
=& \frac{\mu}{2\pi} I \ln \left( \frac{d^2}{r_i^2} \right)
\end{aligned} \tag{3.57}$$

The total flux linkage simplifies if both conductors have the same current and radii, as defined in [12],

$$\lambda = \frac{\mu}{2\pi} I \ \ln \frac{d^2}{r_i^2}, \tag{3.58}$$

where $d$ is the distance between the conductors and $r_i$ is the radius of both conductors. With this we can calculate the external inductance $L'_{\text{ext}}$.

$$L'_{\text{ext}} = \frac{\lambda}{I} = \frac{\mu}{2\pi} \ln \frac{d^2}{r_i^2} \tag{3.59}$$

### 3.3.4. Resistance

The low and high frequency resistances of the two-wire line are defined in the same way as the inner conductor of the coaxial line in Sec. 3.2.4.

$$R'_{\text{lf}} = \frac{2}{\sigma_i A_i} = \frac{2}{\sigma_i r_i^2 \pi} \tag{3.60}$$

$A_i$ is the area, $\sigma_i$ is the conductance and $r_i$ is the radius of one conductor.

$$\begin{aligned} R'_{\text{hf}} &= 2R'_i \\ &= \frac{2}{\sigma_i A_i} \\ &\approx \frac{1}{\sigma_i [\pi r_i \delta_s]} \end{aligned} \tag{3.61}$$

$R_i$ is the resistance of one of the conductors and $\delta_s$ is the skin effect. The approximation used for the area is explained in Eq. 3.82.

## 3.4. Multiconductor Transmission Lines (MTLs)

Until this section we derived formulas for the TL parameters for two-conductors but in real test scenarios cable harnesses often hold significantly more wires. Therefore we take a look on the calcultation of cable parameters for different arrangements of multiconductor transmission lines (MTLs). In [14] Paul et al. described methods to calculate the capacitance **C** and inductance **L** matrix of different MTLs configurations. The formulas presented in [14] approximate a uniform charge distribution on the surface of the conductor therefore a ratio of the wire-separation to wire-radius greater or equal to four is required for this approximation (no proximity effect).

### 3.4.1. System of Wires

Fig. 3.8 depicts a system of $(n+1)$ wires. To calculate the TL parameters for the arrangement in Fig. 3.8 (a) it is necessary to derive the *generalised capacitance matrix* $\mathscr{C}$.

The derivation for the generalised capacitance matrix is is given by Paul and Clements in [15] and [14]. Therefore the *total free charge* $q_{fi}$ and the *potential* $\phi_i$ at each conductor have to be derived. Since the derivation is quite long and intricate it is omitted at this point.

$$\begin{pmatrix} q_{f0} \\ q_{f1} \\ \vdots \\ q_{fn} \end{pmatrix} = \begin{pmatrix} \mathscr{C}_{00} & \mathscr{C}_{01} & \dots & \mathscr{C}_{0n} \\ \mathscr{C}_{10} & \mathscr{C}_{11} & & \vdots \\ \vdots & & & \\ \mathscr{C}_{n0} & \dots & & \mathscr{C}_{nn} \end{pmatrix} \cdot \begin{pmatrix} \phi_0 \\ \phi_1 \\ \vdots \\ \phi_n \end{pmatrix} \tag{3.62}$$

With Eq. 3.63 and 3.64 the generalised capacitance matrix can be converted to the Maxwell capacitance matrix [14] as depicted in Eq. 3.65.

$$V_i = \phi_i - \phi_0 \tag{3.63}$$

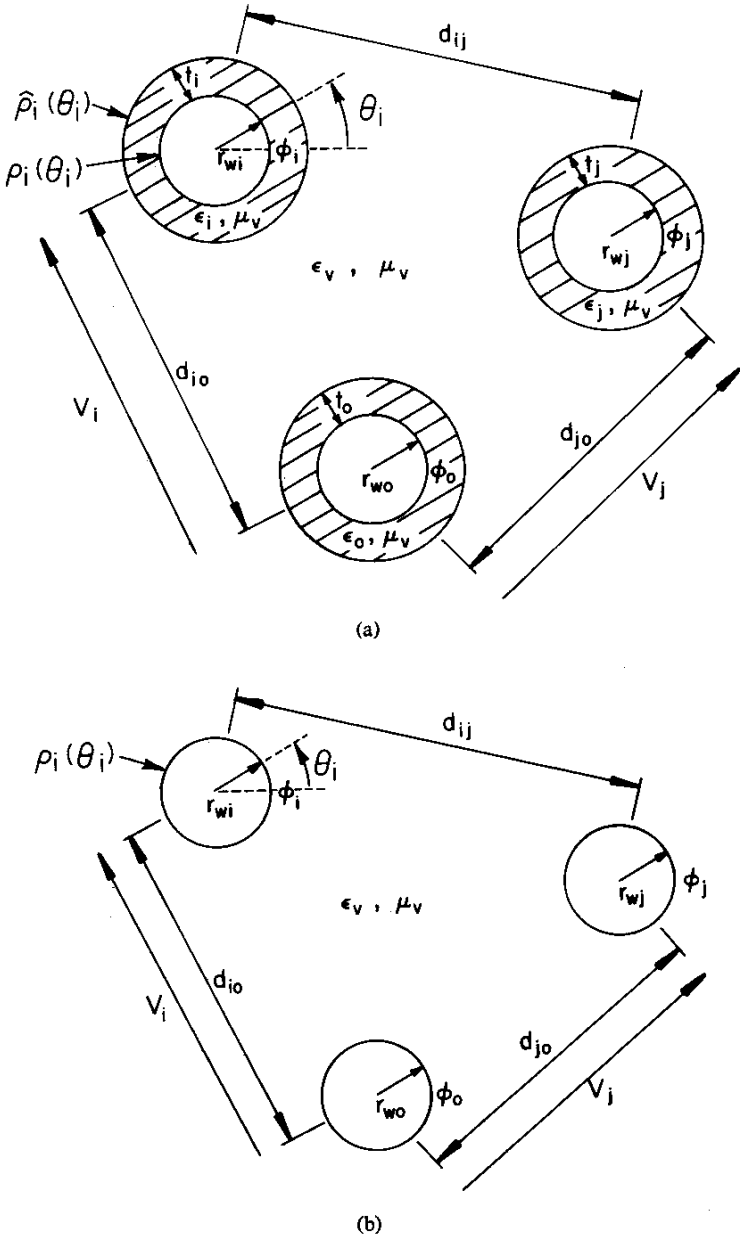


Figure 3.8.: System of n+1 wires, with dielectric material as insulation (a) and without insulation (b) [14].

$$q_{f0} = -\sum_{i=1}^{n} q_{fi} \tag{3.64}$$

$$\begin{pmatrix} q_{f1} \\ q_{f2} \\ \vdots \\ q_{fn} \end{pmatrix} = \begin{pmatrix} C_{11} & C_{12} & \dots & C_{1n} \\ C_{21} & C_{22} & & \vdots \\ \vdots & & & \\ C_{n1} & \dots & & C_{nn} \end{pmatrix} \cdot \begin{pmatrix} V_1 \\ V_2 \\ \vdots \\ V_n \end{pmatrix} \tag{3.65}$$

The Maxwell capacitance matrix $C$ from Eq. 3.65 is defined as follows

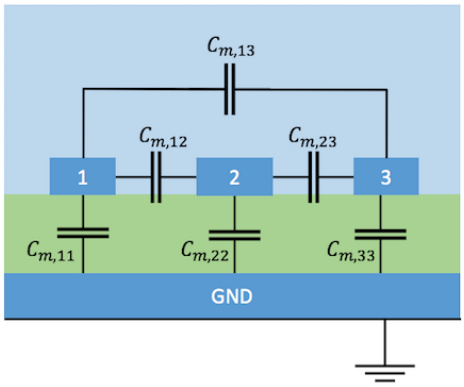


Figure 3.9.: Example for mutual capacitance in a microstrip line over a ground plane [16].

where the $C_{m,ii}$ entries are the mutual capacitances to a reference point (eg. ground) and the $C_{m,ij}$ entries with $i \neq j$ are the mutual capacitances between conductors as shown in Fig. 3.9. The Maxwell capacitance matrix is a symmetric matrix. The conductor-to-ground capacitances are easily calculated by summation of all elements in a column or row, since the off-diagonal elements are negative and the main diagonal holds the sum of all elements in a row or column as depicted in Eq. 3.66.

$$\mathbf{C} = \begin{pmatrix} \sum_{i=1}^{N} C_{m,1i} & -C_{m,12} & \dots & -C_{m,1N} \\ -C_{m,21} & \sum_{i=1}^{N} C_{m,2i} & \dots & -C_{m,2N} \\ \vdots & \vdots & \ddots & \vdots \\ -C_{m,N1} & -C_{m,N2} & \dots & \sum_{i=1}^{N} C_{m,Ni} \end{pmatrix} \tag{3.66}$$

This derivation simplifies considerably for the case in Fig. 3.8 (b). In this case the entries of the capacitance matrix $\mathbf{C}_0$ can be calculated as follows:

$$[\mathbf{C}_0^{-1}]_{ii} = \frac{1}{2\pi\varepsilon_0} \ln\left(\frac{d_{i0}^2}{r_{wi} r_{w0}}\right) \tag{3.67}$$

$$[\mathbf{C}_0^{-1}]_{\substack{ij \\ i\neq j}} = \frac{1}{2\pi\varepsilon_0} \ln\left(\frac{d_{j0} d_{i0}}{d_{ij} r_{w0}}\right) \tag{3.68}$$

for $i, j = 1, \dots, n$. Where $\mathbf{C}_0$ denotes the capacitance matrix without dielectric insulation, $d_{i0}$ is the distance of the $i$th conductor to the reference conductor, in this case the conductor with the index 0, and $r_{wi}$ and $r_{w0}$ are the respective radii. With Eq. 3.69, the matrix correspondence of Eq. 3.54, the inductance matrix can be derived from the free-space capacitance matrix as in Eqs. 3.70 and 3.71.

$$\mathbf{L} = \mu_0 \varepsilon_0 \, \mathbf{C}_0^{-1} \tag{3.69}$$

$$[\mathbf{L}]_{ii} = \mu_0 \varepsilon_0 [\mathbf{C}_0^{-1}]_{ii} = \frac{\mu_0}{2\pi} \ln\left(\frac{d_{i0}^2}{r_{wi} r_{w0}}\right) \tag{3.70}$$

$$[\mathbf{L}]_{\substack{ij \\ i\neq j}} = \mu_0 \varepsilon_0 [\mathbf{C}_0^{-1}]_{ij} = \frac{\mu_0}{2\pi} \ln\left(\frac{d_{j0} d_{i0}}{d_{ij} r_{w0}}\right) \tag{3.71}$$

### 3.4.2. System of Wires above a Ground Plane

Often in EMC testing a ground plane is used to create reference surface and increase repeatability of the measurements. This arrangement of conductors over a conducting ground plane is depicted in Fig. 3.10. In this case the ground plane forms a *electric wall* [11] ($E_t = 0$) where the electric field lines end perpendicular on the plane. This can be solved with the *method of images* [14]. Therefore the ground plane is replaced by a set of image conductors for each original conductor. The image conductors match the dimensions of their original counterparts though they are beneath the ground plane. The potential and the charge distribution on the image conductor are the same as at the original conductor but with opposite sign. When the images are in place as depicted in Fig. 3.10 and the ground plane is omitted, we can calculate the capacitance matrix in the same way as in Sec. 3.4.1.

The entries of the inductance matrix $\mathbf{L}$ are given by

$$[\mathbf{L}]_{ii} = \mu_0 \varepsilon_0 [\mathbf{C}_0^{-1}]_{ii} = \frac{\mu_0}{2\pi} \ln\left(\frac{2h_i}{r_{wi}}\right) \tag{3.72}$$

$$[\mathbf{L}]_{\substack{ij \\ i \neq j}} = \mu_0 \varepsilon_0 [\mathbf{C}_0^{-1}]_{ij} = \frac{\mu_0}{2\pi} \ln\left(\frac{d_{ij}^*}{d_{ij}}\right) \tag{3.73}$$

where $h_i$ is the heigth of the $i$th conductor over the ground plane, $r_{wi}$ is the radius and $d_{ij}$ and $d_{ij*}$ are the distances from conductor $i$ to conductor $j$ and its image conductor respectively. The distance $d_{ij*}$ is given as

$$\begin{aligned} d_{ij*} &= \sqrt{(h_j + h_i)^2 + d_{ij}^2 - (h_j - h_i)^2} \\ &= \sqrt{d_{ij}^2 + 4h_i h_j}. \end{aligned} \tag{3.74}$$

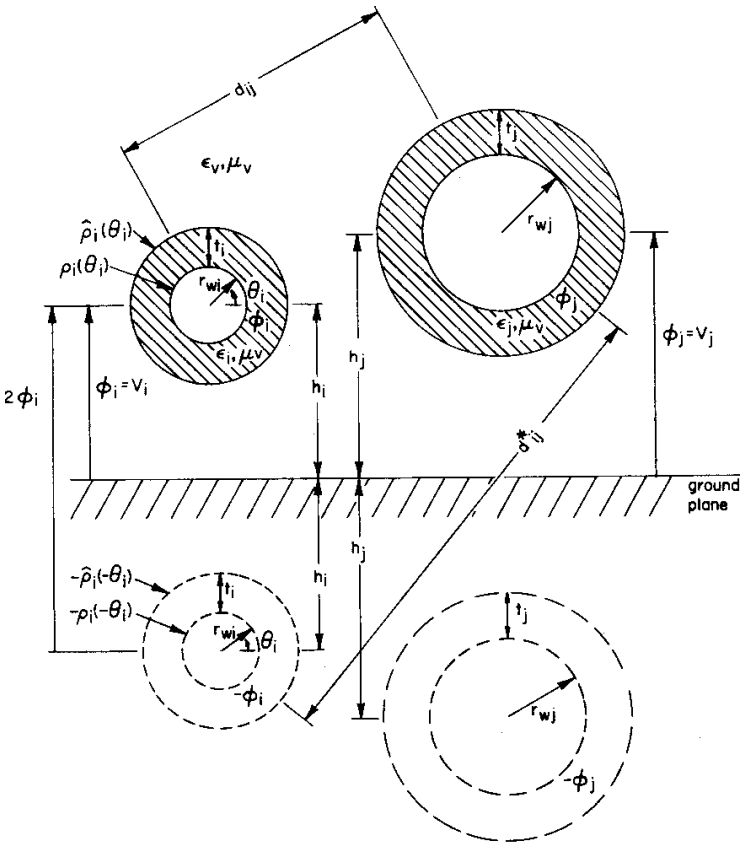


Figure 3.10.: System of n wires above a conducting ground plane, from [14].

### 3.4.3. System of Wires within a circular Shield

The system of n-wires in a circular shield as depicted in Fig. 3.11 can also be solved with the *method of images* as in Sec. 3.4.2, described by Paul in [14]. Therefore the image conductors are placed on a straight line through the center of the shield and the $i$th conductor at distance $r_s^2/ri$ from the center, where $r_s$ is the radius of the circular shield and $r_i$ the distance from the center to the $i$th wire. Placement of the image charges is depicted in Fig. 3.12.

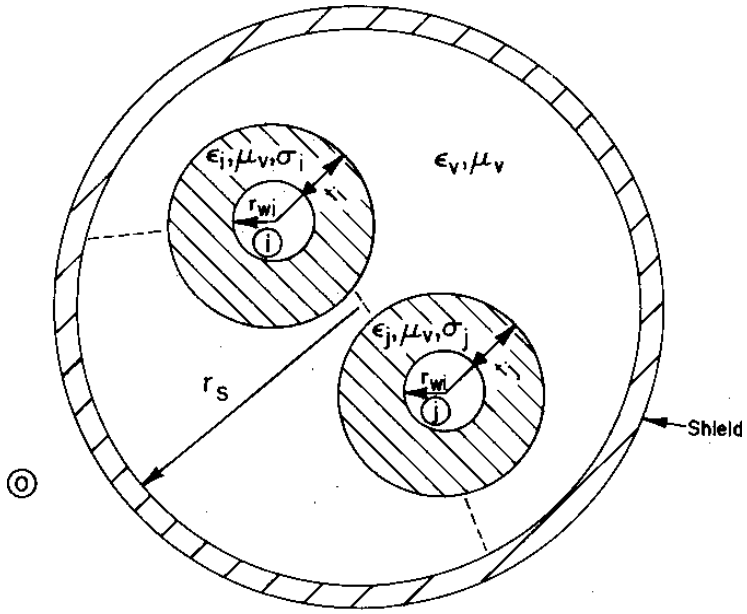


Figure 3.11.: Wires in a conducting circular shield, from [14].

With this the entries of the inductance matrix can be calculated the same as before [14].

$$L'_{ii} = \mu_0 \varepsilon_0 [\mathbf{C}_0^{-1}]_{ii} = \frac{\mu_0}{2\pi} \ln\left(\frac{r_s^2 - r_i^2}{r_s r_{wi}}\right) \tag{3.75}$$

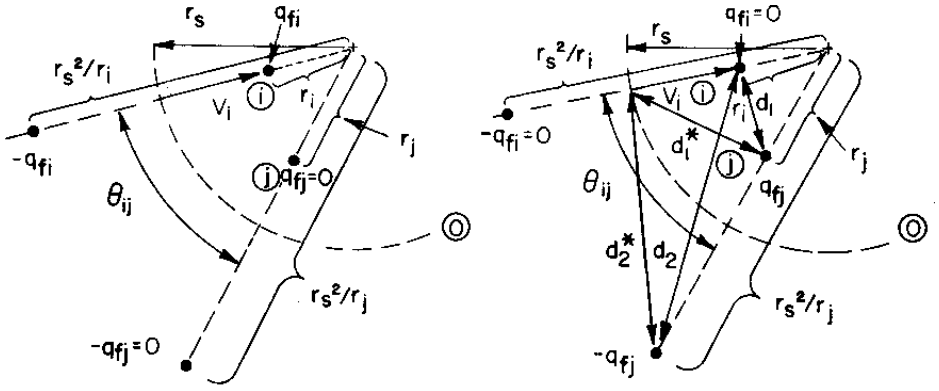


Figure 3.12.: Schematic of Fig. 3.11 with line charges and their respective images [14].

$$L'_{\substack{ij \\ i\neq j}} = \mu_0\varepsilon_0[\mathbf{C}_0^{-1}]_{ij} = \frac{\mu_0}{2\pi}\ln\left[\left(\frac{r_j}{r_s}\right)\sqrt{\frac{(r_i r_j)^2 + r_s^4 - 2r_i r_j r_s^2\cos(\theta_{ij})}{(r_i r_j)^2 + r_j^4 - 2r_i r_j^3\cos(\theta_{ij})}}\right] \tag{3.76}$$

## 3.5. RLGC Model of a Transmission Line

With the p.u.l. parameters of the TL defined it is viable to represent the TL by a cascade of lumped circuit elements as depicted in Fig. 3.13. These circuit elements can be arranged in gamma, pi and t-structures. The later ones have the advantage of a symmetric structure whereas the gamma structure needs less circuit elements, especially when you take the mutual capacitances and inductances between the conductors, which are not shown in Fig. 3.13, into account.

The RLCG lumped-circuit model has a certain bandwidth determined by the number of sections. Bogatin approximated the bandwidth for such a lumped circuit in [17] as follows

$$BW_{model} = \frac{n}{4}\cdot\frac{f_0}{2} \approx n\cdot\frac{f_0}{10} = n\cdot\frac{1}{10\cdot T_D} = n\cdot\frac{v_p}{10\cdot\mathscr{L}} \tag{3.77}$$

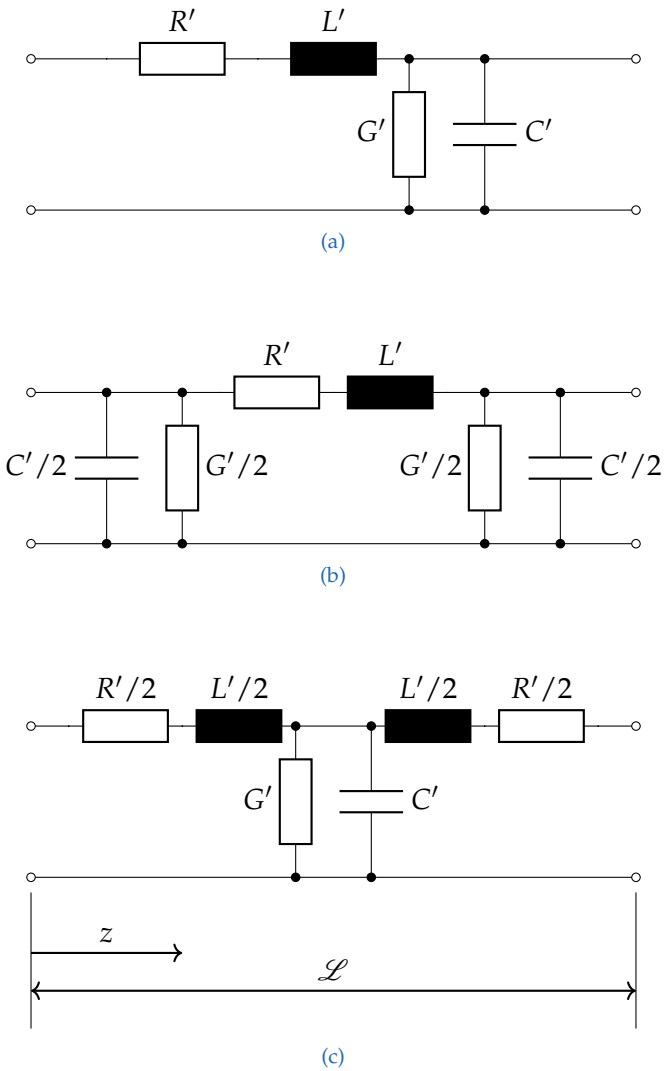


Figure 3.13.: Equivalent TL circuit elements, reverse gamma (a), pi (b) and T structure (c).

where $n$ is the *number of sections*, necessary to achieve the bandwidth, $f_0$ is the frequency at which the wavelength is equal to the length of the line, $T_D$ is the *time delay* introduced by the line and $v_p$ is the *phase velocity*.

The length of a single line segment $\Delta\mathscr{L}$ should suffice following convention

$$\Delta\mathscr{L} \leq \frac{\lambda}{10} = \frac{v_p}{f_{\max}}\frac{1}{10} = \frac{1}{10f\sqrt{L'C'}} = \frac{c}{\sqrt{\mu_r\varepsilon_r}\,10\,f_{\max}}\,, \tag{3.78}$$

where $\mathscr{L}$ is the physical length of the line and $\lambda$ the wavelength as in Eq. 3.25. When the segments are larger the behaviour of the TL can not be reproduced satisfactory and if the segments are smaller the computational effort increases. A sweet-spot needs to be found. The number of segments is given in [18] by

$$N \geq 10f_{max}\frac{\mathscr{L}}{v_p} = 10f_{\max}\frac{\mathscr{L}\sqrt{\mu_r\varepsilon_r}}{c_0}\,, \tag{3.79}$$

where $f_{\max}$ is the maximum frequency of interest .

## 3.6. Losses

In this section the effects that cause losses in TLs are discussed and formulas to describe their behaviour are presented.

### 3.6.1. Skin Effect

As Wheeler outlined in [20] the skin effect is a reduction of the current density in the center of the conductor at high frequencies. With reference to [21] this effect is due to eddy currents induced by the changing magnetic field and the counter electromagnetic field (EMF) produced by them. This change in current distribution leads to an increase of resistance with increasing frequency. The current density changes from a uniform distribution at direct

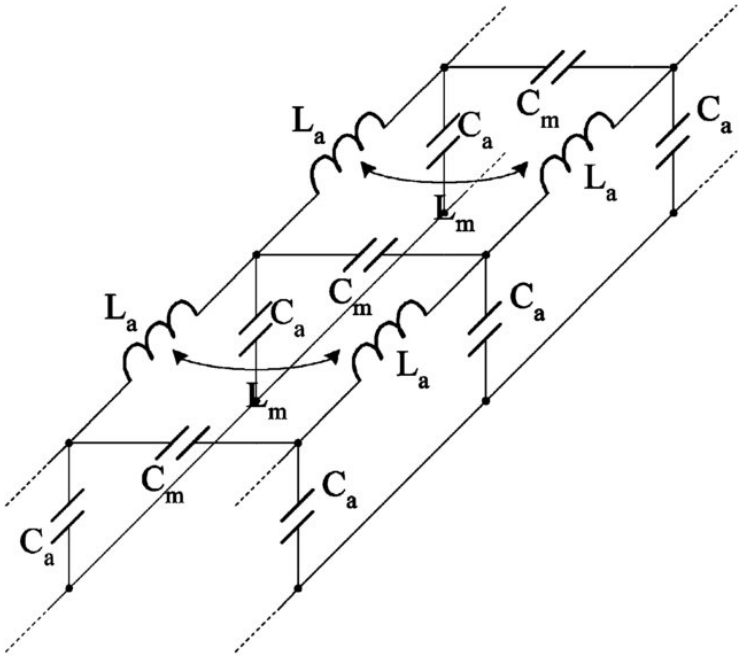


Figure 3.14.: Lumped equivalent circuit for a lossless TL with mutual capacitance and inductance between conductors [19].

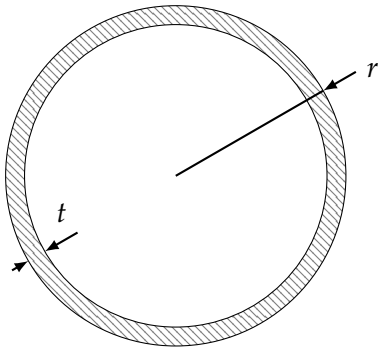


Figure 3.15.: Ring with radius $r$ and thickness $t$.

current (DC) to a current distribution only on the surface as shown in Fig. 3.16. The current density $J$ decreases according to following formula:

$$J = J_S \, e^{-(1+j)d/\delta_s} \, , \tag{3.80}$$

where $J$ is the current density at depth $d$, $J_S$ is the current density at the surface and $\delta_s$ is the *skin depth* described in Eq. 3.81. The skin depth $\delta_s$ is the depth where the current density is reduced by $1/e$ or 37% and is calculated as follows

$$\delta_s = \sqrt{\frac{2\rho}{\omega\mu}} = \sqrt{\frac{\rho}{\pi f \mu}} \, , \tag{3.81}$$

where $\rho$ is the electric resistivity of the conductor, as listed in Tab. 3.1, $\omega$ is the angular frequency and $\mu$ is the permeability of the conductor material, which is for most non-magnetic conductors close to one and can therefore be neglected. The resulting area shaped like ring and is given by

$$A_{\text{skin}} = r^2\pi - (r-t)^2\pi = 2rt\pi - t^2\pi \approx 2rt\pi \, , \tag{3.82}$$

where $r$ is the outer radius of the ring and $t$ its thickness as depicted in Fig. 3.15. In case of $t \ll r$ the last term ($\pi t^2$) is often omitted.

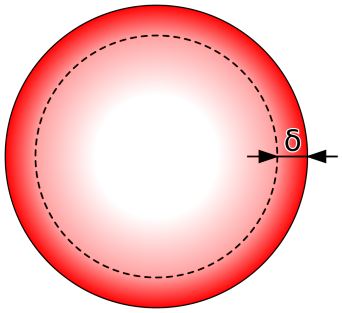


Figure 3.16.: The skin depth $\delta$ revers to the point where the current density $J_S$ at the surface of the conductor reduces to $1/e$ or 37% [22].

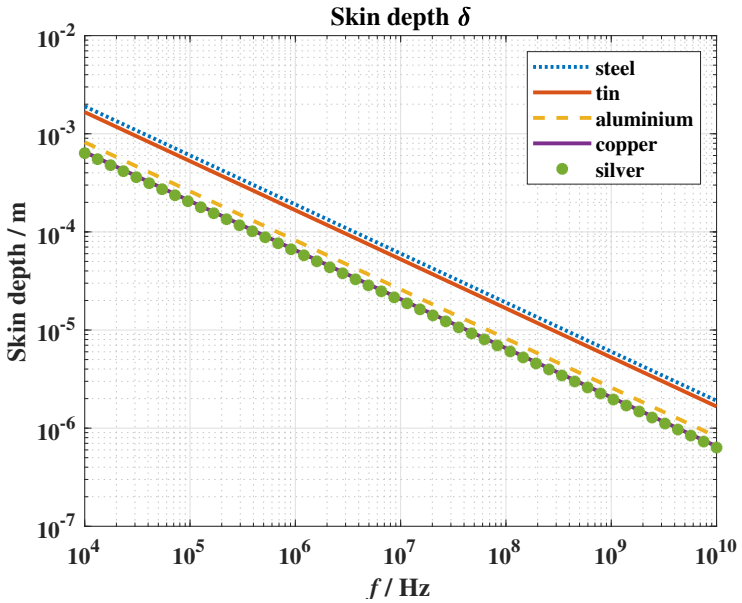


Figure 3.17.: The skin depth $\delta$ for different materials over frequency.

| Material | Resistivity $\rho(\Omega \cdot \mathrm{m})$ at 20 °C | Conductivity $\sigma(S/\mathrm{m})$ at 20 °C |
|---|---|---|
| Silver | $1.59 \times 10^{-8}$ | $6.30 \times 10^{7}$ |
| Copper | $1.68 \times 10^{-8}$ | $5.96 \times 10^{7}$ |
| Aluminium | $2.65 \times 10^{-8}$ | $3.77 \times 10^{7}$ |
| Tin | $1.09 \times 10^{-7}$ | $9.17 \times 10^{6}$ |
| Steel | $1.43 \times 10^{-7}$ | $6.99 \times 10^{6}$ |

Table 3.1.: Resistivity and conductivity for different materials from [23].

The surface of the conductor has a certain roughness to it. As long as the skin depth is larger than these surface contour variations the influence of the surface rougness on the resistance is negligible but with increasing frequency the skin depth reaches a point where the surface current has to follow the varying contour and is therefore additionally increased by a rough sourface finish. This can be solved easily by a smoother surface finish.

### Equivalent Circuit Model for Skin Effect

Kim et al. proposed a non uniform ladder circuit in [24] to model the increase in series resistance induced by the skin effect. Therefore the cross-section of the conductor is divided into four concentric rings with the same relative difference in resistivity from one ring to the other, as depicted in Fig. 3.18 $(a)$. Each section of the ladder represents one of the rings. The ladder is constructed so that every resistor has a R-L lowpass in parallel, as depicted in Fig. 3.18 $(b)$, and reducing the overall impedance. With increasing frequency the impedance of each inductor increases until the overall impedance is dominated by the remaining paths and therefore increases.

There are certain requirements on the circuit [24]. The DC resistance of the ladder circuit must be the same as the DC resistance $R_{dc}$ of the conductor and similarly the low frequency inductance of the circuit must be the same as the actual low frequency inductance $L_{lf}$ of the conductor. The resistance ratio is defined as

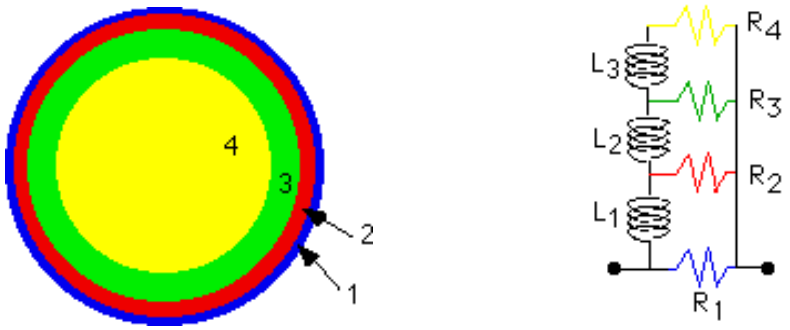


(a) (b)

Figure 3.18.: Depiction of the ladder circuit proposed in [24]. Cross-section of the conductor (a) and ladder circuit (b). Related conductor regions and circuit elements have matching colors [25].

$$RR = \frac{R_i}{R_{i+1}}, \quad i = 1, 2, 3, \tag{3.83}$$

also the first resistance $R_1$ is defined as

$$R_1 = \alpha_R R_{dc}, \tag{3.84}$$

where $R_{dc}$ is the DC resistance of the conductor and $\alpha_R$ is

$$\alpha_R = 0.53 \frac{\text{wire radius}}{\delta_{\max}}, \tag{3.85}$$

where $\delta_{\max}$ is the skin depth at the maximum frequency of interest. All those requirements together lead to the following cubic equation:

$$(RR)^3 + (RR)^2 + RR + (1 - \alpha_R) = 0 \tag{3.86}$$

The inductance values are obtained the same way, starting with the inductance ratio

$$LL = \frac{L_i}{L_{i+1}}, \quad i = 1, 2, 3, \tag{3.87}$$

and the first inductance value $L_1$ is defined as

$$L_1 = \frac{1}{\alpha_L} L_{lf}, \qquad with \quad \alpha_L = 0.315\ \alpha_R \tag{3.88}$$

where $L_{lf}$ is the low frequency inductance and $\alpha_L$ depends on $\alpha R$. The inductance ratio $LL$ is obtained the same way from Eq. 3.89.

$$\begin{aligned} \left(\frac{1}{LL}\right)^2 + \left(1 + \frac{1}{RR}\right)^2 \frac{1}{LL} + \left(\left[\frac{1}{RR}\right]^2 + \frac{1}{RR} + 1\right)^2 \\ -\alpha_L \left(\left[1 + \frac{1}{RR}\right]\left[\left(\frac{1}{RR}\right) + 1\right]\right)^2 = 0 \end{aligned} \tag{3.89}$$

### 3.6.2. Proximity Effect

The *proximity effect* is a high frequency effect that increases the series resistance of conductors when they are close together. Similar to the skin effect [21] eddy currents are induced by a changing magnetic field and reduce the current density. In this case the source of the changing magnetic field is the alternating current in the opposing conductor. Both conductors are affecting each other mutually. The resulting current distribution depends of the current direction, conductor diameter, distance between the conductors, the conductors form and the frequency. Fig. 3.19 shows the mutual attraction or repulsion of the current distributions for different current directions. Proximity effect does not affect coaxial lines because of their circular symmetry [26], but is a significant factor in e.g. parallel wires or twisted-pair TLs. As [26] points out a analytical solution tends to be complicated and there is no general solution.

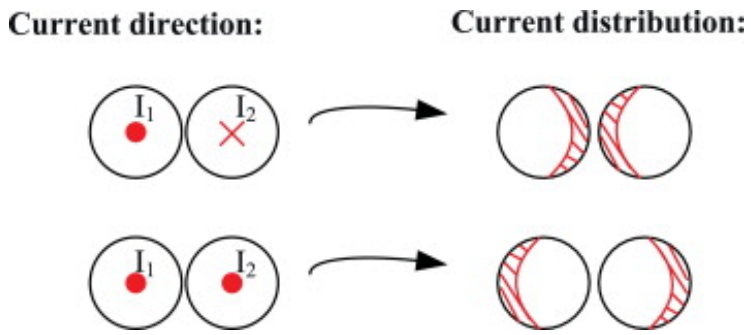


Figure 3.19.: Proximity effect in two conductors with same and opposing current directions [27].

### 3.6.3. Dielectric Losses

The *dielectric loss* describes an energy loss through heating by polarisation when a dielectric material is placed in a varying electric field. This is the case for capacitors and also for cables or TLs with dielectric material between its conductors, e.g. coaxial cables. The dielectric loss is dependent on the dielectric material and the frequency. We start by examining the dissipation current through a block of dielectric material, with surface area $A$ and height $h$, defined by [26] as follows:

$$I(\omega) = V(\omega)\frac{A}{h}(\sigma + j\omega\varepsilon) \tag{3.90}$$

where $V$ is the applied voltage with angular frequency $\omega$. $\sigma$ and $\varepsilon$ are the conductivity and permittivity of the material. The current in Eq. 3.90 can be separated into a real part (in-phase term), that is called the conduction current, and the imaginary part (quadrature term), which is called displacement current. Depending if your material is a conductor or a insulator one of both is dominant.

$$\varepsilon(\omega) = \varepsilon' - j\varepsilon'' \tag{3.91}$$

We rewrite Eq. 3.90 with Eq. 3.91 where $\varepsilon'$ is the lossless permittivity and $\varepsilon''$ is associated with the losses due to bound charges and dipole relaxation.

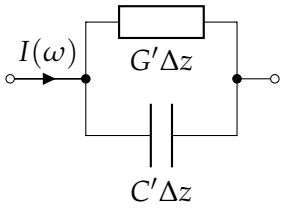


Figure 3.20.: Equivalent circuit diagram of dielectric material.

$$I(\omega) = V(\omega)\frac{a}{h}((\sigma + \varepsilon'') + j\omega\varepsilon') \tag{3.92}$$

In some literature as [11] the losses are summarised into $\varepsilon''$. The dielectric loss tangent, denoted as $\tan\delta$, relates the losses to the energy storing capacity of the material.

$$\tan(\delta) = \frac{(\sigma + \varepsilon'')}{\varepsilon'} \tag{3.93}$$

Note that it is often denoted as $\tan\delta = {}^{\varepsilon''}/_{\varepsilon'}$ where $\sigma$ is included in $\varepsilon''$.

When we now think back at our TL from Fig. 3.2 we can take a closer look at the shunt resistance depicted in Fig. 3.20. The shunt current is

$$I(z,\omega) = V(z,\omega)(G' + j\omega C')\Delta z. \tag{3.94}$$

With the relations presented above we can express the conductivity $G'$ from $C'$ and $\tan\delta$.

$$G' = \omega C' \tan(\delta) \approx \omega C'\ \delta \tag{3.95}$$

For dielectric materials with small losses $\tan(\delta) \approx \delta$ holds, because of the linearity around the origin of the $\tan(.)$ function.

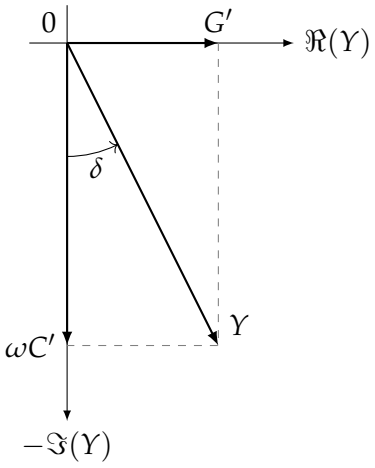


Figure 3.21.: Vector diagram of equivalent electric circuit (EEC) in 3.20.

## 3.7. Scattering Parameters

A two-port network is a four terminal circuit where two terminals each are consolidated into a port. Therefore the terminals of the port need to suffice the port condition which states that the current flowing into one terminal, has to match the current going out the other terminal of the port as shown in Fig. 3.22 [11].

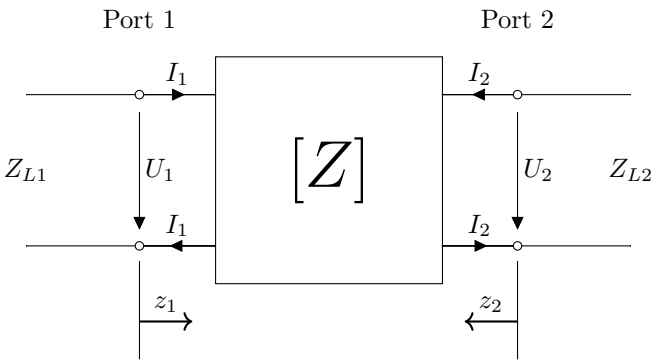


Figure 3.22.: Two-port network with voltages and currents.

These two-port networks can be described by Z- or Y-parameters as in Eq. 3.96 by linking the currents to voltages via $Z_{ij}$ Parameters.

$$\begin{pmatrix} U_1 \\ U_2 \end{pmatrix} = \begin{pmatrix} Z_{11} & Z_{12} \\ Z_{21} & Z_{22} \end{pmatrix} \begin{pmatrix} I_1 \\ I_2 \end{pmatrix} \tag{3.96}$$

The voltages and currents in Eq. 3.96 can be expressed by the forward propagating and the reflected voltage waves, as already shown in 3.1.1.

$$\begin{aligned} U_1 &= U_{p1} + U_{r1}, \quad I_1 = \frac{U_{p1}}{Z_L} - \frac{U_{r1}}{Z_L} \\ U_2 &= U_{p2} + U_{r2}, \quad I_2 = \frac{U_{p2}}{Z_L} - \frac{U_{r2}}{Z_L} \end{aligned}$$

Scattering parameters link the normalised reflected voltage wave $b_i$ to the forward propagating voltage wave $a_i$ as shown in Eq. 3.99 and Fig. 3.23.

$$a_i = \frac{U_{pi}}{\sqrt{\Re\{Z_{Li}\}}} \tag{3.97}$$

$$b_i = \frac{U_{ri}}{\sqrt{\Re\{Z_{Li}\}}} \tag{3.98}$$

The normalised voltage waves have the dimension $\sqrt{\text{Watt}}$.

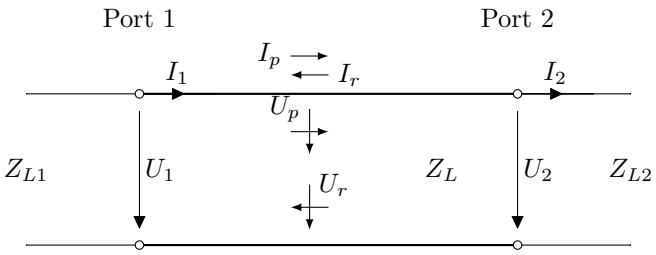


Figure 3.23.: Example of an RF line with voltage and current waves along the line.

$$\begin{pmatrix} b_1 \\ b_2 \end{pmatrix} = \begin{pmatrix} S_{11} & S_{12} \\ S_{21} & S_{22} \end{pmatrix} \begin{pmatrix} a_1 \\ a_2 \end{pmatrix} \tag{3.99}$$

The coefficients of the scattering parameter matrix **S** are determined by driving port $j$ with forward propagating wave $a_j$ and measuring the reflected wave $b_i$ on port $i$ whilst all other ports are terminated with matched loads to avoid reflections $a_k = 0$.

$$S_{ij} = \frac{b_i}{a_j}|_{a_k=0 \text{for} k \neq j} \tag{3.100}$$

The coefficients for the example two-port circuit in Fig. 3.24 are defined in [11] as follows:

$S_{21}$ forward transmission factor with matched output

$S_{11}$ input reflection coefficient with matched load at the output

$S_{12}$ reverse transmission factor with matched input

$S_{22}$ output reflection coefficient with matched load at the input

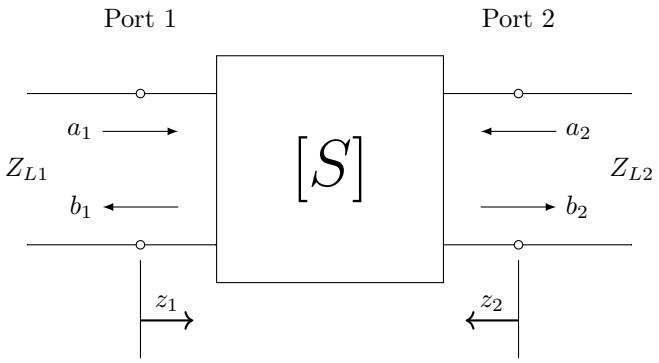


Figure 3.24.: S-parameter network with incident and reflected power waves $a_i$ and $b_i$.

# 4. Modelling

This chapter describes how the different parts of the BCI test are modelled and put together to allow for simulation of the BCI test methode.

## 4.1. Cable Model

The modelling of the cable harnesses is a complicated task and commonly used S-parameter representations from measurements or simulations result in models that are not easily adaptable to changes in length or geometry.

Ch. 3 explains how to extract the TL parameters from different geometries and Sec. 3.5 provides a methodology to create a TL model from the parameters, as presented in [28].

The cable models used for simulations are either S-parameter files or RLCG TL models as SPICE netlist files, since the used simulation environment (Ansys, ED 2019R1) supports both representations.

## 4.2. Injection Probe Model

This section describes the different approaches chosen to model the BCI probe *F-120-6A* from FCC.

The injection probe is in principle a transformer whereby it's primary winding is wrapped around the ferrite core and connected to the type-N connector and the secondary winding is formed by one or multiple wires, depending on the cable harness, routed through the ferrite core. Therefore the approach

choosen to model the injection probe originates from the modelling of transformers. To illustrate this Fig. 4.1 depicts an equivalent circuit diagram of a transformer. The ohmic losses due to the wire resistance and the leakage inductance due to leakage flux are not coupled to the secondary winding are denoted as $R_P$ and $L_P$ respectively. The same repeats for the secondary winding with $R'_S$ and $L'_S$, these values are additionally denoted with an apostrophe to show that these are values from the secondary referred to the primary side e.g. $R'_S = {}^{R_S}/_{n^2}$. The main inductance and core losses are denoted as $L_M$ and $R_C$ respectively. For simplification the primary and secondary winding losses are combined into $Z_{wp}$ and $Z'_{ws}$ respectively and the excitation branch is denoted as $Z_{mp}$.

A simple and often used method to characterize a transformer is by *open* and *short* measurement [29]. For this the impedance is measured at the primary side while the secondary side is *open* or *short* circuited. In the open configuration there is no current flow through the secondary winding and therefore also no secondary winding losses $Z'_{ws}$. The resistance of this configuration is mainly determined by the excitation branch $Z_{mp}$. This is in contrast to the short measurement where the impedance is mainly determined by both primary and secondary winding losses. Equation 4.1 and 4.2 describe the *open* and *short* impedance respectively, where *OS* and *SS* stand for *open secondary* and *short secondary* respectively. With this measurements the elements of the equivalent cirucit in Fig. 4.1 can be determined.

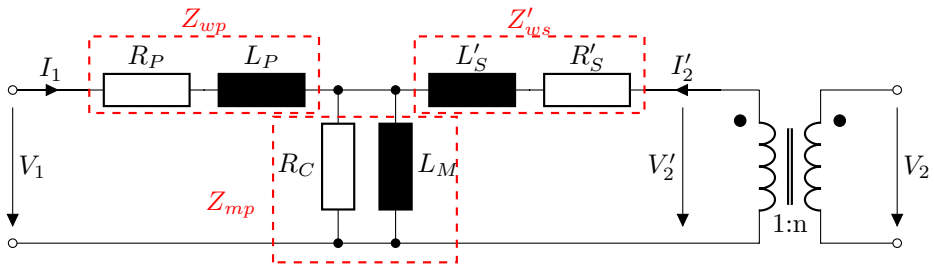


Figure 4.1.: Equivalent circuit diagram of a transformer, depicted as a two-port circuit.

$$Z_{p(OS)} = Z_{wp} + Z_{mp} \tag{4.1}$$

$$Z_{p(SS)} = Z_{wp} + \frac{Z_{mp} Z'_{ws}}{Z_{mp} + Z'_{ws}} \tag{4.2}$$

In the case of the BCI probe the *short* measurement is impractical since the secondary winding is determined by the used cable harness. Therefore only the *open* measurement without the presence of a cable harness was performed. Since the main excitation $Z_{mp}$ is much bigger than the primary winding losses $Z_{wp}$ the winding losses were neglected. Therefore the following BCI probe models were modelled upon the *open* measurement of the BCI probe.

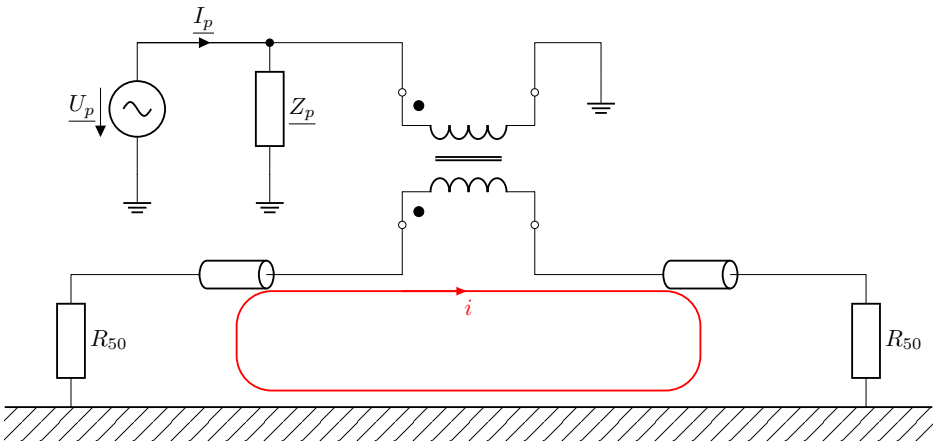


Figure 4.2.: Equivalent circuit diagram of BCI probe on harness.

The measurements were made with a vector network analyzer (VNA) in one port also known as reflection configuration. The measurement system was calibrated (short, open, load) so that the reference plane was located at the input of the probe connector.

### 4.2.1. Probe Impedance Circuit Model

In the objectives Ch. 1 it was mentioned that the probe circuit model is required to consist of passive RLC-elements. This requirement excludes all newer modelling variants described in Sec. 1.4. For this reason the injection probe circuit was modeled following the procedure described in [30]. To

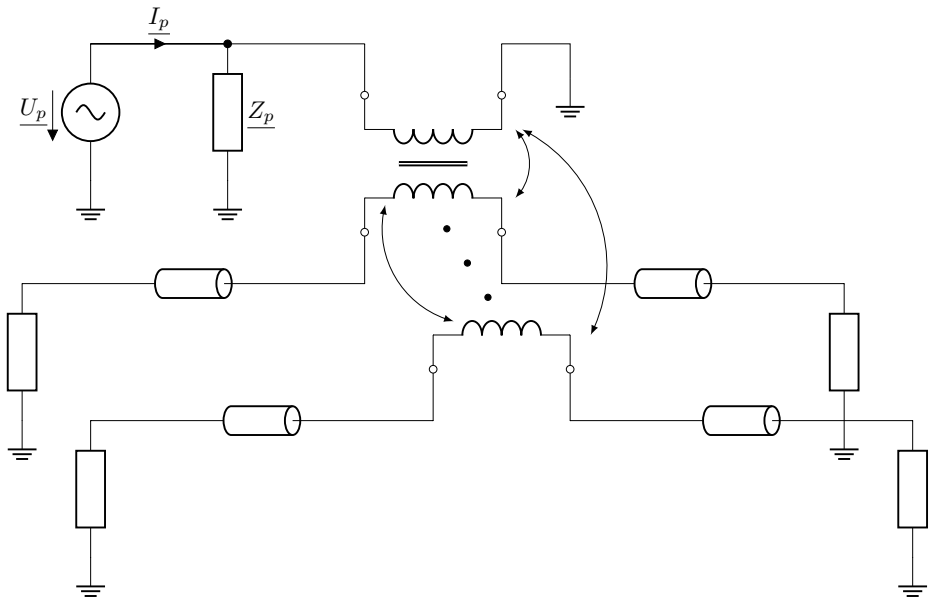


Figure 4.3.: Equivalent circuit diagram of BCI probe on harness.

recreate the probe impedance a number of series connected RLC parallel circuits was used, as depicted in Fig. 4.5. The number of used parallel circuits depends on the number of resonances that are in the impedance spectrum, depicted frequency range and required accuracy.

$$f_r = \frac{1}{2\pi\sqrt{LC}} \tag{4.3}$$

$$Q = R\sqrt{\frac{C}{L}} \tag{4.4}$$

$$BW = \frac{f_r}{Q} \tag{4.5}$$

An RLC parallel circuit is a second-order circuit. At the resonance frequency $f_r$ (Eq. 4.3) the impedance of the circuit is at a maximum and is soley

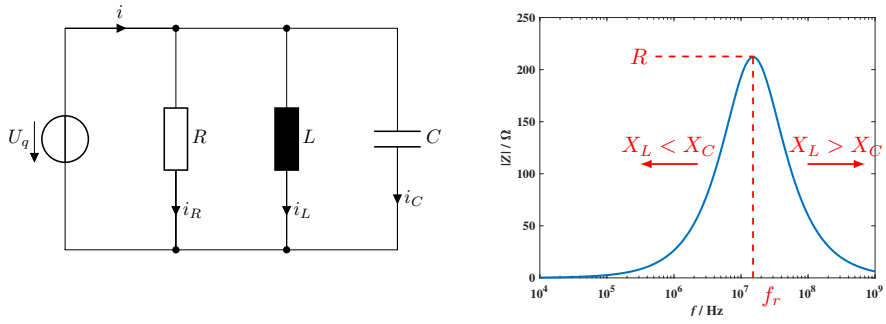


(a) (b)

Figure 4.4.: (a) RLC-parallel circuit and (b) magnitude of the impedance of a RLC-parallel ciruit over frequency, where $f_r$, $X_L$ and $X_C$ are the resonance frequency and the reactance of the inductor and capacitor respectively.

determined by the resistor as depicted in Fig. 4.4. The resonance frequency is defined by the relation of the values of the reactive components as shown in Eq. 4.3. The quality factor $Q$ (Eq. 4.4) can be changed by altering the values of the reactive components by the same but inverse ratio. With this the bandwidth of an RLC element can be changed as shown in Eq. 4.4 and 4.5.

The probe model is easily created by adding one parallel element for each local maxima in the impedance spectrum to replicate. Further parallel elements are added depending on necessary accuracy, for example to better match certain slopes. A series resistance, with the DC resistance value of the coil, necessary to ensure correct DC behaviour in simulations is omitted in this model. The resulting impedance graph is the superposition of all resonances as depicted in Fig. 4.5. Fig. 4.6 depicts the finished probe model versus measurements.

### Coupling Model

In contrast to the 3D model where the coupling of the probe to the harness is an inherent part of the model the circuit model needs a way of coupling the probe circuit to the cable harness and DUT.

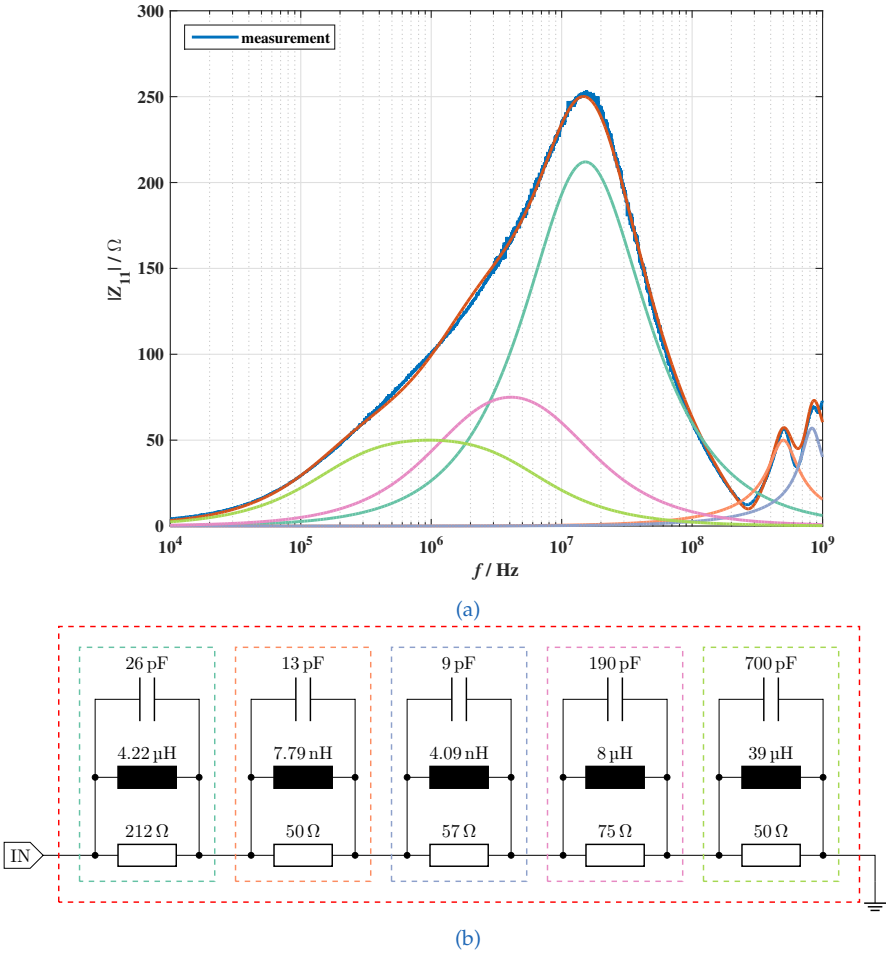


Figure 4.5.: Plot of all individual parallel impedances and the superposition (red) next to a measurement of the actual probe impedance (blue) (a), probe model circuit framed in matching colours (b).

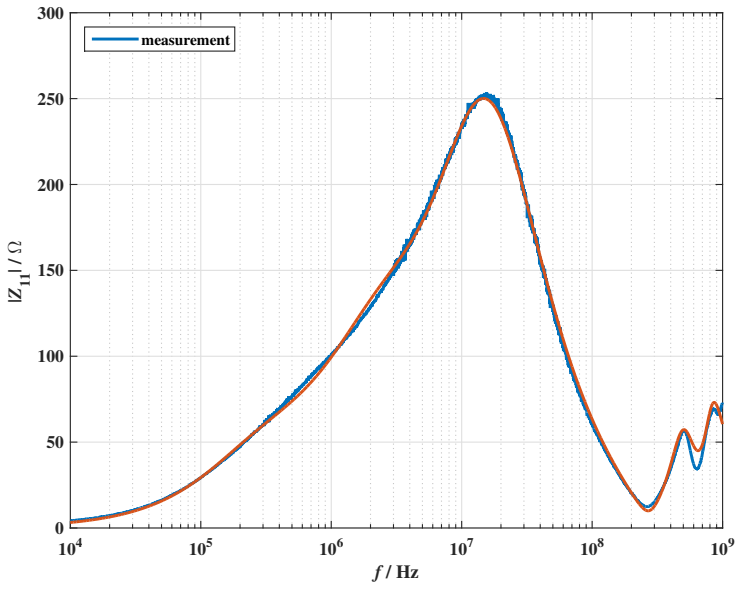


(a)

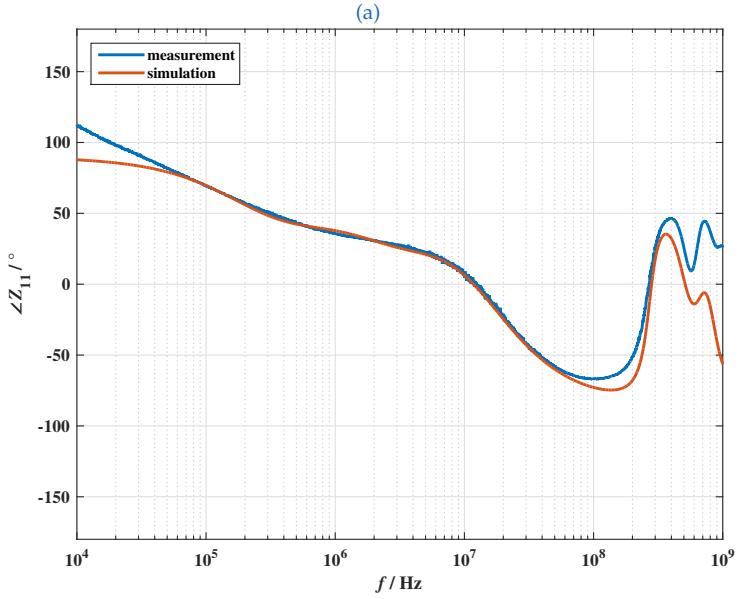


(b)

Figure 4.6.: Magnitude (a) and phase (b) of the measured and simulated probe impedance.

The circuit model explained in the former section consists of series connected parallel RLC circuits. Each parallel circuit contains an inductance. Modelling the coupling via mutual inductance statement e.g. SPICE [31] would also require inductances in the receiving harness. The amount of inductances involved would render the mutual inductance statement complicated and prone to failure.

The coupling between the injection probe and the cable harness is modelled as an ideal inductive coupling via the use of ideal transformers with coupling coefficients of one. An ideal inductive coupling was chosen because both windings utilize the same ferrite core. Capacitive coupling was disregarded because of the construction of the injection probe whereby the outer housing of the injection probe is connected to the signal ground. The injection probe and the harness together form a multi-winding transformer with multiple windings on one shared core as depicted in Fig. 4.7. Similar coupling methods for one wire harnesses were already proposed in [32]–[35], where the couplings were modelled with ideal transformers.

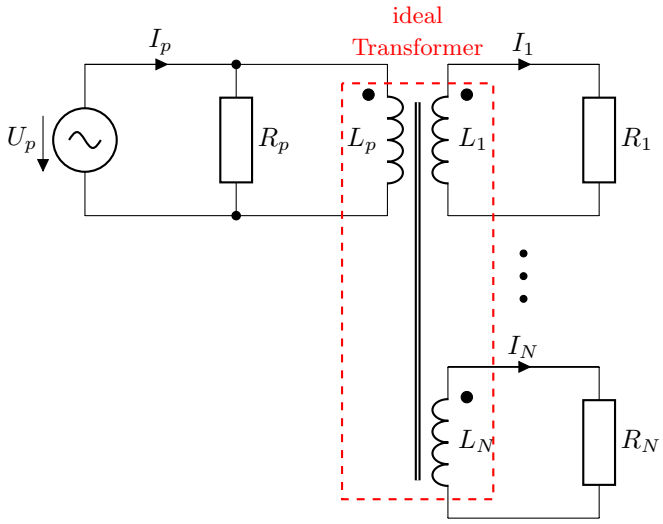


Figure 4.7.: Equivalent circuit diagram of a transformer with $N + 1$ windings.

A disadvantage of this approach is that the amount of necessary couplings increases substantially with the number of wires in the harness as follows:

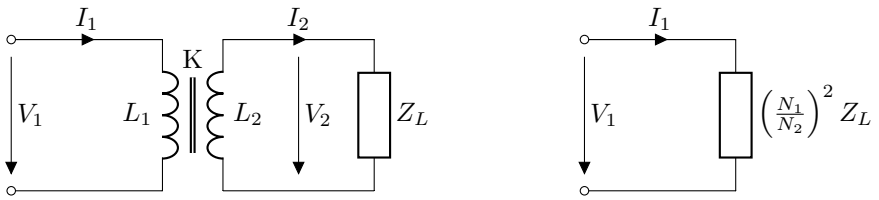


Figure 4.8.: Impedance conversion from secondary to primary side.

$$L = \frac{(N+1) \cdot N}{2}, \tag{4.6}$$

where $N$ is the number of windings or wires in the harness and $L$ is the number of mutual inductances or couplings.

### Source Model

During the BCI test the measurement equipment records forward and reverse power at the directional coupler as well as the common mode (CM) current in the cable harness. To compare the measured and simulated currents it is necessary to source the model with the same power as during the measurements. The net power ($P_{\text{net}} = P_{\text{fwd}} - P_{\text{rev}}$) describes the part of the forward power that is not reflected and therefore goes into the probe. In the utilized simulation environment only a frequency dependend sinusoidal voltage source is available, therefore the net power was converted to voltage for every frequency point. The net power was recorded in decibel milliwatt (dBm) and is defined as:

$$P_{\text{net, dBm}}(f) = 10 \cdot \log_{10}\left(\frac{P_{\text{net}}}{1\,\text{mW}}\right), \tag{4.7}$$

where $P_{\text{net}}(f) = \frac{V_S^2}{Z_{in}}$, $V_S$ is the voltage at the probe and $Z_{in}$ is the input impedance of the injection probe loaded with the cable harness and its

terminations on each side of the harness. With this we can calculate the probe voltage as follows:

$$V_S(f) = \sqrt{10^{\frac{P_{\text{net, dBm}}}{10} - 3} \cdot \underline{Z_{in}}} \tag{4.8}$$

As mentioned earlier the BCI probe can be described as a transformer whereby the cable harness embodies the secondary winding. Therefore the probe is loaded with the harness and its terminations. To get the input impedance $Z_{\text{in}}$ it is necessary to simulate or measure the respective measurement setup. This was done for all BCI test setups.

### 4.2.2. Probe 3D Model

The 3D model of the injection probe (FCC 120-6A) was drawn up from measurements and x-ray imaging, since dismantling the probe was not viable. The x-ray images gave crucial information about the internal structures of the probe, which allowed a very accurate model of the injection probe. It revealed the off-centre placement of the ferrite core in its aluminium housing as well as the form and connection of the primary winding as shown in Fig. 4.10. This effort was necessary to achieve a mechanically very accurate model of the probe, as depicted in Fig. 4.9, but still the ferrite material and its frequency behaviour were unknown.

Since the ferrite core of this particular probe consists of two separate ferrits, with visually different material appearences, emphasis was placed on determining an equivalent permeability $\hat{\mu}(\omega)$ to match the probe impedance over the frequency range of interest.

#### Determine Permeability

For the 3D model to match the physical dimensions is not enough, it is also necessary that the material properties of the ferrite are accurately depicted, so that the model matches the probe input impedance.

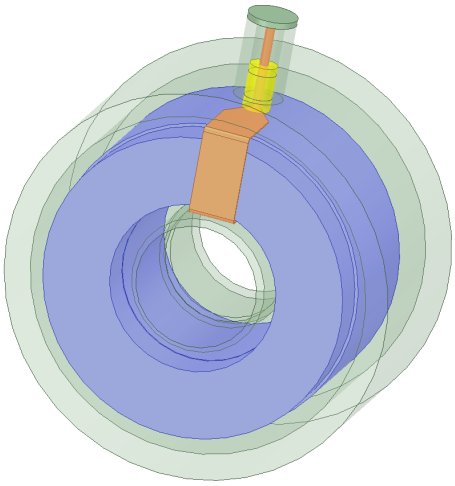

Figure 4.9.: 3D model of the injection probe (*FCC 120-6A*).

To aquire the equivalent complex permeability $\hat{\mu}(\omega)$ of the ferrite core different methods were tried as explained below.

It was not possible to match the probe impedance by assigning a constant permeability to the ferrite core. Grassi provides an analytical formula for a ferrite in [4]. The equivalent circuit for the probe is shown in Fig. 1.12. For the following equations just the primary circuit is used. Eqs. (4.9, 4.10) are the input impedance $Z_{in}$ rearranged for the self inductance $\hat{L}_1$ of the probe or primary winding. Where the indices $W$ and $N$ denote winding and N-connector related parasitics respectively.

$$\hat{L}_1(\omega) = \frac{1}{D}\{Z_{in}(\omega) - j\omega(L_N + L_{W1}) - \omega^2 L_{W1} \times (C_N + C_{W1})[Z_{in}(\omega) - j\omega L_N]\} \tag{4.9}$$

$$D = j\omega\{1 + j\omega(C_N + C_{W1})[-Z_{in}(\omega) + j\omega L_N]\} \tag{4.10}$$

Alternatively Eq. 4.11 describes the self inductance of the probe as a function of shape and dimensions with the assumption $\mu_r = 1$ as follows

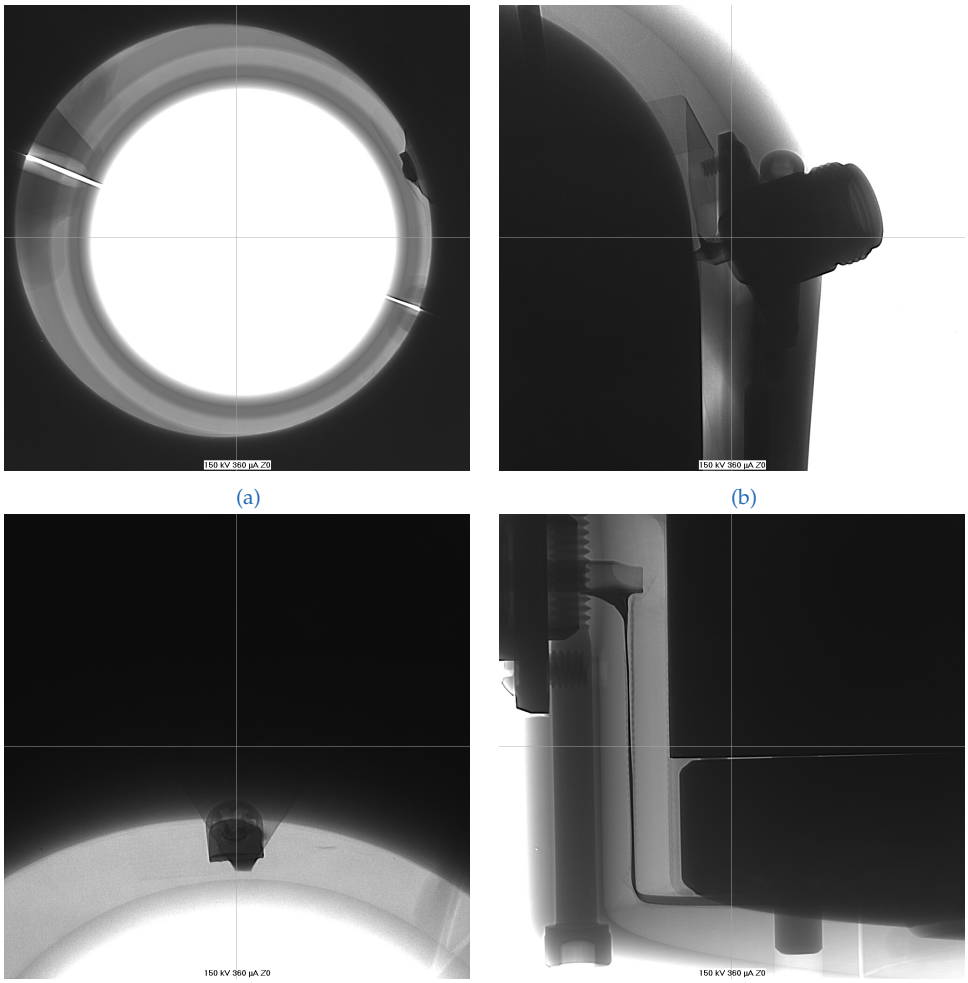


(a) (b)

(c) (d)

Figure 4.10.: X-ray images of the FCC 120-6A BCI probe. The black areas in the images are the ferrite core in its aluminium housing (light grey). Figure (a) displays the off-centre position of the ferrite core in the housing. Figures (b), (c), and (d) show the primary winding going from the N connector around the ferrite core and terminating into the aluminium housing on the side of the probe. Tapering of the coil to the connection points is noticeable. These X-ray images were made by ams AG Premstätten.

$$L_0 = \mu_0 \frac{N_1^2 b}{2\pi} \ln\left(\frac{r_c^{(o)}}{r_c^{(i)}}\right), \tag{4.11}$$

were $N_1$ is the number of turns, $b$, $r_c^{(o)}$ and $r_c^{(i)}$ are thickness, and outer and inner radius of the ferrite core respectively. Multiplication with $\mu_r(\omega)$ again gives $\hat{L}_1$. With this one can calculate $\mu_r$ from $Z_{in}$ and the probe dimensions.

$$\hat{L}_1(\omega) = L_0[\mu_r'(\omega) - j\mu_r''(\omega)] \tag{4.12}$$

Due to the different construction of the probe used in this work simulations of the model with the calculated permeability produced considerable different values for the probe impedance compared to the measured probe impedance as shown in Fig. 4.11.

To aquire the equivalent complex permeability $\hat{\mu}(f)$ of the ferrite core, first an initial estimate for $\hat{\mu}$ was calculated with the analytical formulas derived by Grassi for the explicit model shown in Fig. 1.12 [4].

To aquire the equivalent complex permeability $\hat{\mu}(f)$ of the ferrite core, the analytically calculated permeability, denoted as inital estimate, was used as start value for an optimization task. Goal of the optimization task was to fit the permeability so that the 3D models impedance reproduces the measurements as close as possible. The results of the optimization are shown in Fig. 4.11. Due to a problem with the function fitting the model impedance deviates significantly below 100 MHz.

## 4.3. Calibration Fixture

The calibration fixture was modelled as a pi-circuit similar to [5].

The measurements were made with a VNA in two port series configuration. The measurement system was calibrated (short, open, load) so that the reference plane was located at the input of the probe connector.

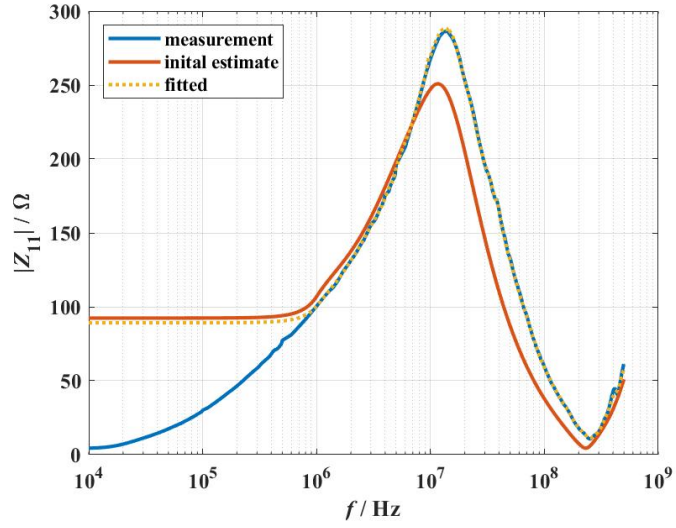


(a)

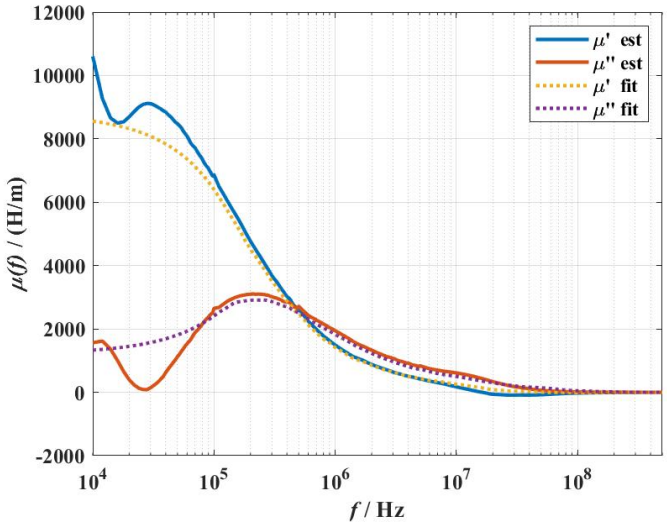


(b)

Figure 4.11.: Magnitude of probe input impedance (a), measured, calculated and fitted, real and imaginary part of ferrite permeability (b), calculated and fitted.

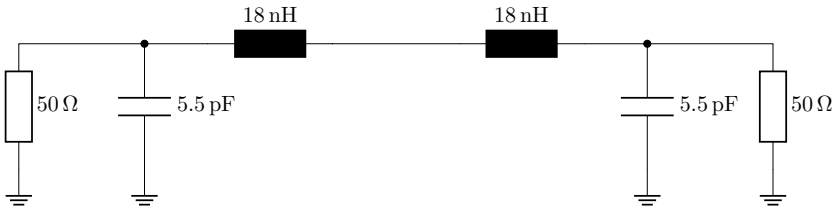


Figure 4.12.: Equivalent circuit diagram of the calibration fixture.

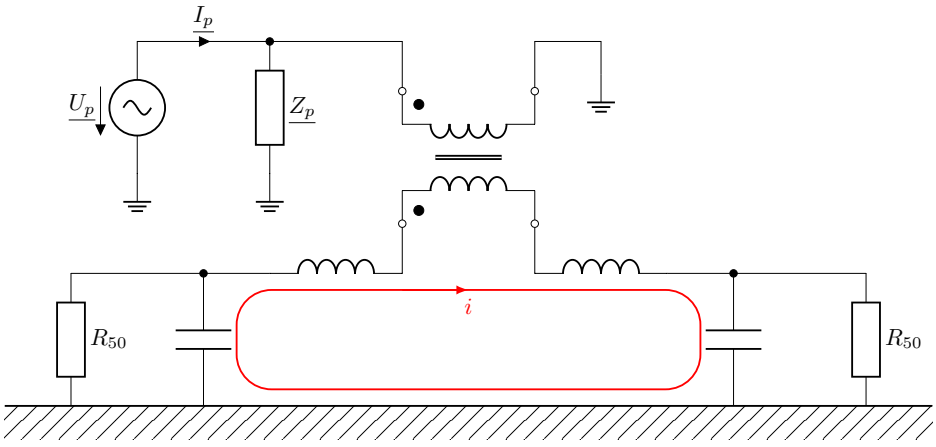


Figure 4.13.: Equivalent circuit diagram of the bci probe on the calibration fixture.

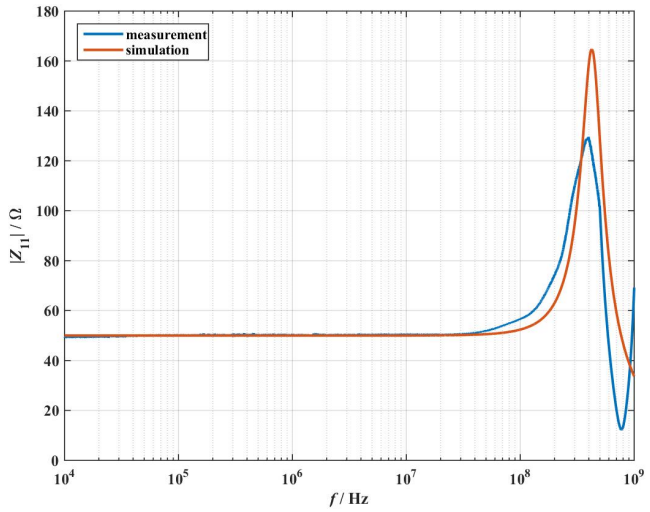


(a)

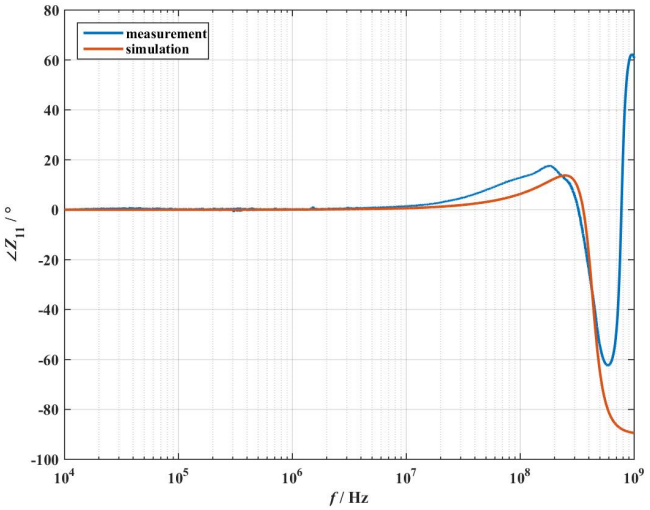


(b)

Figure 4.14.: Magnitude (a) and phase (b) of calibration fixture input impedance, measured and simulated.

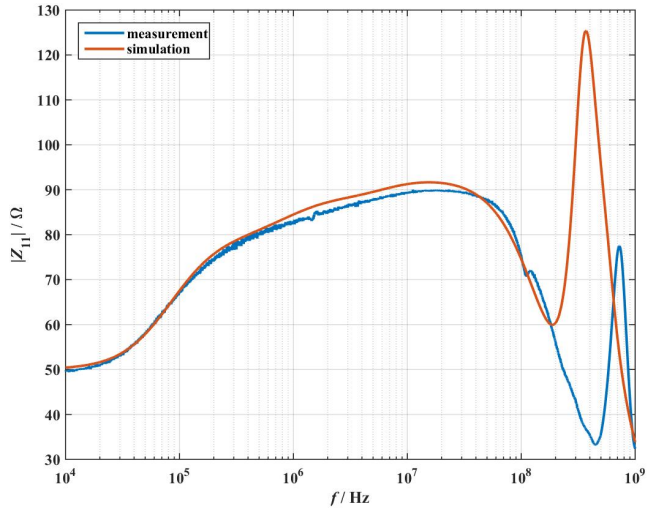


(a)

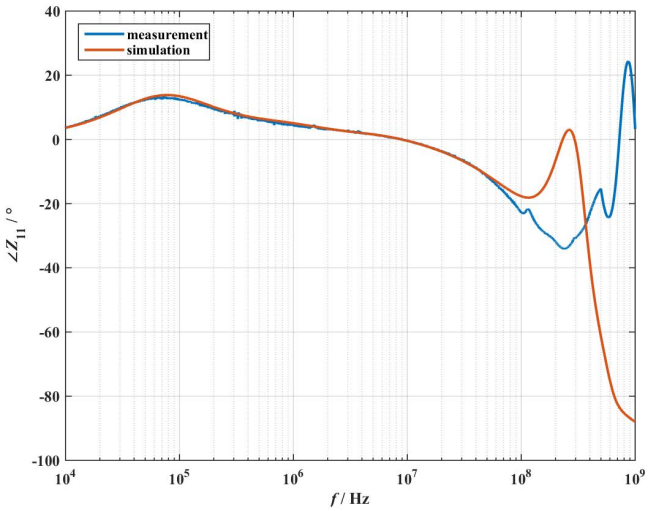


(b)

Figure 4.15.: Magnitude (a) and phase (b) of calibration fixture input impedance, whilst injection probe is mounted in the fixture. The port of the injection probe is terminated with 50 Ω.

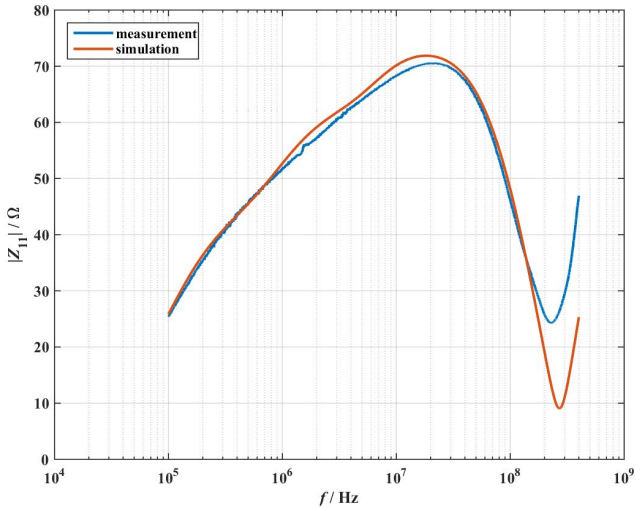


(a)

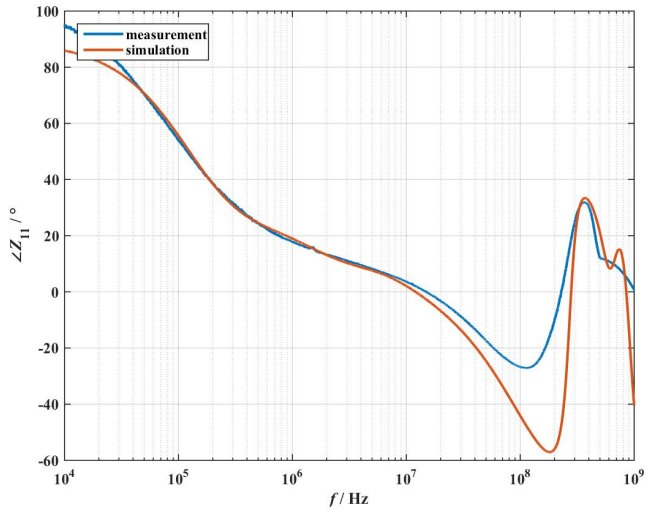


(b)

Figure 4.16.: Magnitude (a) and phase (b) of injection probe input impedance, whilst injection probe is mounted in the fixture. For the measurement the fixture ports are terminated with 50 Ω.

# 5. Results

This chapter compares measured common mode currents from actual BCI tests to simulated currents with either the described circuit model or the 3D model.

To validate the presented model several quasi BCI tests were executed in different setups and configurations. The measured common mode currents were recorded and compared to the simulated currents. The subsequent BCI tests adhere to the test methods described in Sec. 2 and in the ISO standard [2].

## 5.1. BCI Probe on Calibration Fixture

For this test the probe is mounted on the calibration fixture similar as during the calibration process, as depicted in Fig. 5.1. The calibration fixture is also terminated with 50 Ω.

The first test utilized the *substitution* method, as described in Sec. 2.1.5. For the *substitution* method, first a power profile needs to be recorded on the calibration fixture. A constant target current of 150 mA is selected, because it corresponds to the maximum current of **Test Level III** from Tab. 2.2.

For this, the injection probe is mounted in the calibration fixture. The fixture is terminated with 50 Ω. The forward power necessary to achieve the target current in the calibration fixture is recorded at every frequency step.

When the probe is mounted on the actual test setup the DUT is then exposed to a disturbance signal generated by the RF amplifier and injected into the cable harness. The RF amplifier replicates the same net power as previously

recorded during the calibration. The current injected into the actual test setup depends on the input impedance of the test setup.

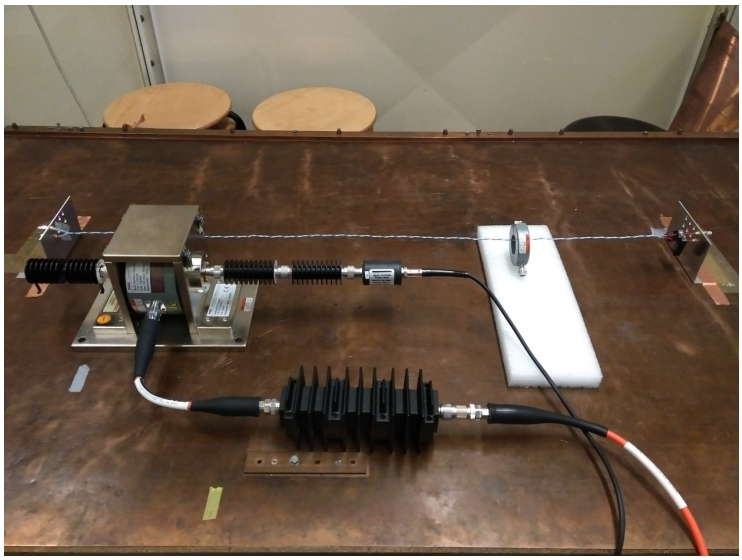

Figure 5.1.: The BCI injection probe on the calibration fixture. A termination resistor, and power probe were visible on the left and right side of the calibration fixture respectively. The power amplifier was connected via an attenuator to the probe.

Since this test setup is the same as the calibraton setup the measured current is around 150 mA as expected.

For the S-parameter model a two-port measurement between the probe and one side of the calibration fixture is used using the same source data as the circuit model and terminated by 50 Ω. Therefore the relatively constant deviation between the s-parameter model and the measurement current can be affiliated to the source data. The drop in the current of the circuit model after 200 MHz is related to problems or inaccuracies of the circuit model of the calibration fixture. Since the calibration fixture is relatively short compared to the wavelength of the highest frequency we don't see any resonances caused by the geometric dimensions.

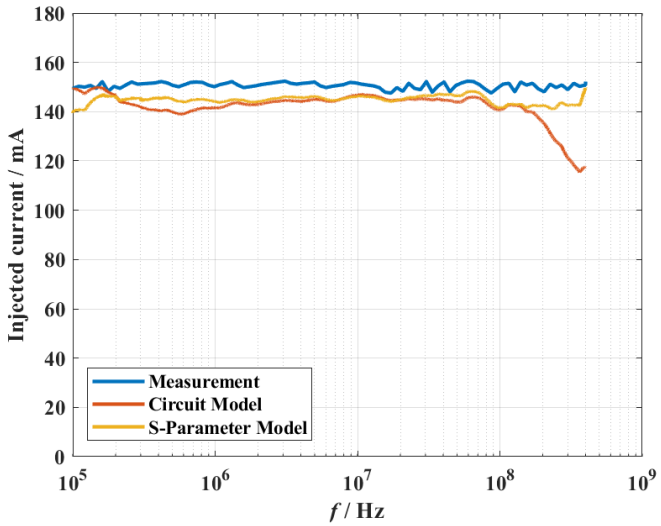


Figure 5.2.: Measured and simulated current injected into the calibration fixture.

## 5.2. BCI Probe on Twisted Pair

For this setup a twisted wire pair (TWP) transmission line is spanned between two angle brackets made of aluminium. The line is 1 m long and 65 mm above a conducting ground plane. The TWP is mounted in the angle brackets with SMA connectors which are terminated with 50 Ω resistors. The measurement and injection probe are positioned at 500 mm and 900 mm from the right bracket respectively.

The line length of 1 m was choosen to match the copper rods used in following tests.

According to [36] a difference in the injected current can be observed if the harness is placed close to the body of the probe. Therefore the angle brackets, depicted in Fig. 5.3b, were designed so that the cable harness passes through the center of the probe opening, resulting in a bigger distance of the cable harness to the ground plane than specified in the ISO standard. For the TWP two vertically stacked holes in the angle bracket were used to mount the

SMA connectors resulting in a harness height of 65 mm above the conducting ground plane.

Deviating from the standard, the position of the injection and monitoring probe was altered to make room for additional current probes to measure the current in each conductor. The probes were connected to an oscilloscope. Unfortunately this resulted in disturbance of the Oscilloscope and no utilisable data.

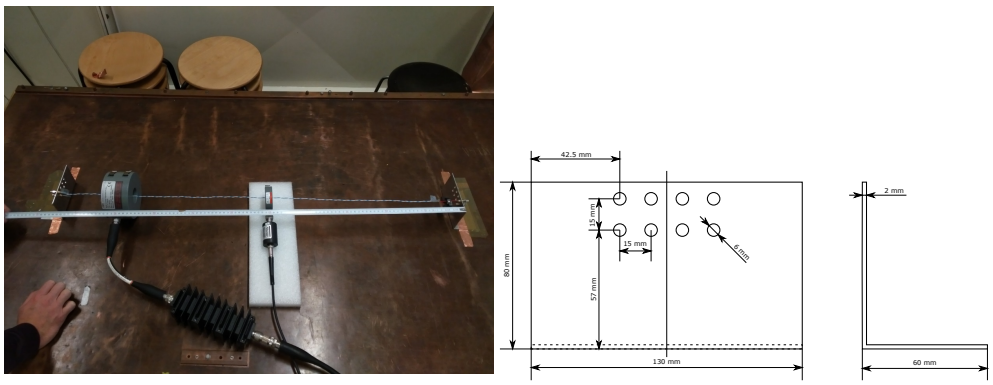


(a) (b)

Figure 5.3.: Test setup of the 1 m long TWP between aluminium angle brackets (a). The TWP is mounted 65 mm over a conducting ground plane. The wire ends are soldered to SMA connectors and where terminated with 50 Ω SMA resistors. The measurement and injection probes are positioned at 500 mm and 900 mm from the right. Detail of the aluminium angle bracket (b).

This test used the *closed loop* method. Similar to the *substitution* method, the *closed loop* method starts with recording the power profile of the injection probe on the calibration fixture whilst terminated with 50 Ω. During the test the calibration power is applied and the injected CM current is measured. Is the measured current below the target current the power is increase, up to 6 dB until the target current is reached as explained in Sec. 2.1.6. For this setup the target current is set to 150 mA.

Fig. 5.4 shows a flat current curve until 30 MHz as a result of the controlled input power. Above that frequency, the injected current decreased because the input power reached its limit. The decrease of the injected current below

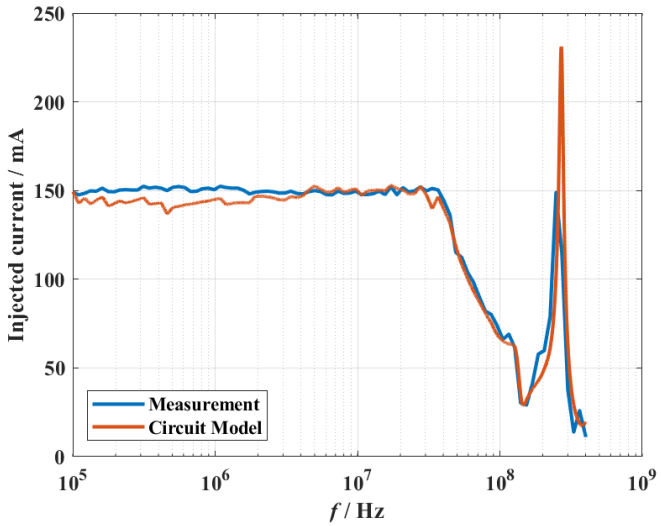


Figure 5.4.: Measured and simulated current injected into a TWP, with *closed loop* method.

150 mA arises from an increased input impedance in that region. There the input impedance increased so high that the target current could not be reached within the power limits. The capability of this test method to adjust the output power according to the target current is the reason why there is no influence of the termination on the injected current.

The peak above 200 MHz is the result of a reduced input impedance at that Frequency. A resonance resulting from the line length would be expected at 300 MHz, due to the isolation material between the conductors this resonance frequency is reduced, as deduced in Eq. 3.25.

## 5.3. BCI Probe on Copper Rod

This test investigates the injection into a straight copper rod of 5 mm diameter and a length of 1 m. SMA connectors were soldered to each end. The copper rod was mounted into the formerly mentioned angle brackets and is situated at 72 mm above a conducting ground plane, as displayed in Fig. 5.5. The

measurement probe is located 50 mm from the right bracket and the injection probe is placed in the center. Both ends of the copper rod were terminated with 50 Ω

From here on the following test setups utilize the *substitution* method with a different current profile for calibration. The calibration current is similar to **Test Level IV**, as shown in Tab. 2.2, without the current decrease at the end. The target current increases exponentially from 6.67 mA at 100 kHz to 200 mA at 3 MHz and stays constant from then on till 400 MHz, as depicted in Fig. 5.5b. The linear increase of the current in Fig. 2.7 comes from the logarithmic scaling of the Y-axis.

Fig. 5.6 presents the comparism of the measured and simulated injection current for the injection into a single copper rod. The circuit for this setup is depicted in Fig. 4.3. The path for the injected current is formed by the copper rod, termination resistors and ground plane. The impedance of this loop is mainly determined by the sum of the terminations and adds up to 100 Ω.

Similar to the results of the TWP the input impedance increases substantially above 10 MHz. The peak at 300 MHz corresponds to the expected resonance resulting from the line length of 1 m. Due to the lack of dielectric material the resonance is exactly at 300 MHz.

## 5.4. BCI Probe on two Copper Rods

The setup from before is now extended by a second copper rod of the same dimensions, as shown in Fig. 5.7. Several measurements with varying injection probe positions and termination resistances were conducted. In the first test the injection probe is positioned at the center, 500 mm from the right. The measurement probe is located 50 mm from the right, for all tests. For the other tests the injection probe is put at 850 mm from the right. Termination of the terminals was varied. As the last setup, this setup also utilizes the *substitution* method with the prior introduced calibration profile, depicted in Fig. 5.5b.

The first thing that is immediately recognizable in Fig. 5.8, Fig. 5.9 and Fig. 5.10 is that the injected current increased in all tests. The current increase

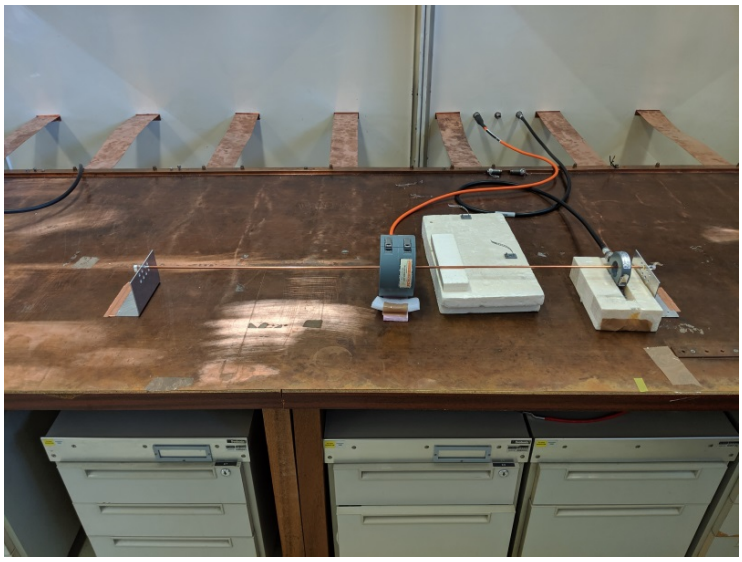

(a)

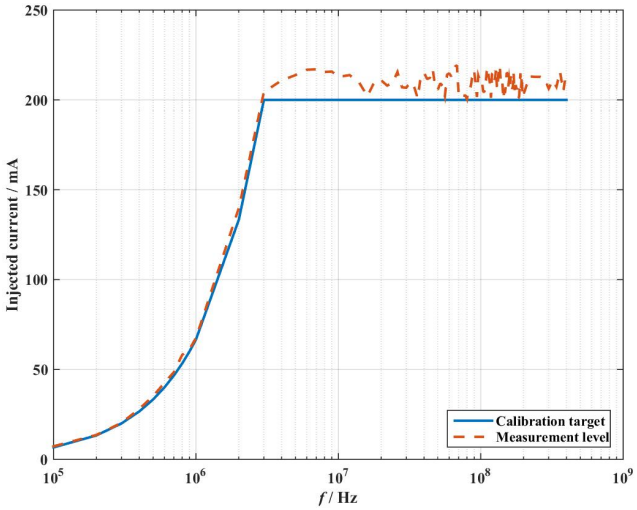


(b)

Figure 5.5.: BCI injection into a single copper rod of 1 m length, 72 mm over a conducting ground plane (a). The measurement and injection probes are positioned at 50 mm and 500 mm from the right side respectively. Target and measured calibration current for the substitution method (b).

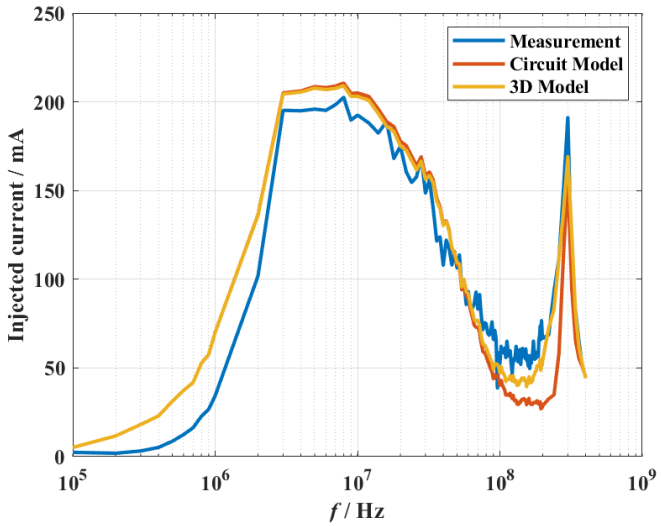


Figure 5.6.: Measured and simulated current for BCI injection into a single copper rod. The injection probe and the measurement probe were positioned in the center and 50 mm from the right bracket. Both ends were terminated with 50 Ω SMA resistors.

results from the impedance reduction due to the parallel circuit formed by the second copper rod. In the case of Fig. 5.8, the loop impedance decreased to 50 Ω from 100 Ω in the previous test. The resonance at 300 MHz is noticeable in Fig. 5.8 and less pronounced in Fig. 5.9 and Fig. 5.10. In Fig. 5.9 and Fig. 5.10

Additionally to the much smaller resonance at 300 MHz, there appears a new resonance at 150 MHz. The difference between these tests is the position of the injection probe. Therefore it must be assumed that this resonance is contingent on the changed probe position.

## 5.5. BCI Probe on six isolated Wires

In this test a 2.5 m harness consisting of six automotive wires was used, as depicted in Fig. 5.11. The measurement probe was again placed at 50 mm

(a) (b)

Figure 5.7.: First test setup with the injection and measurement probe at the center (500 mm) and 50 mm from the right (a). Second setup with the measurement probe again at the same position and the injection probe at 850 mm from the right side (b).

and the injection probe was put at 900 mm from the right angle bracket. All terminals were equally terminated with 50 Ω.

As a result of the additional wires the impedance of the setup decreased again and we see therefore that the current in this setup is larger than in the previous ones. Fig. 5.12 illustrates excellent correlation of resonance frequencies of measurement and the simulation, although the model shows resonance exaltation for the simulated current.

The current peak at 120 MHz corresponds to the expected resonance resulting from the line length of 2.5 m.

It is noticeable in Fig. 5.12 that the second and third current peaks of the simulation were slightly higher than in the measurement. This can be attributed to inaccuracy in the cable models parameters like the isolation material.

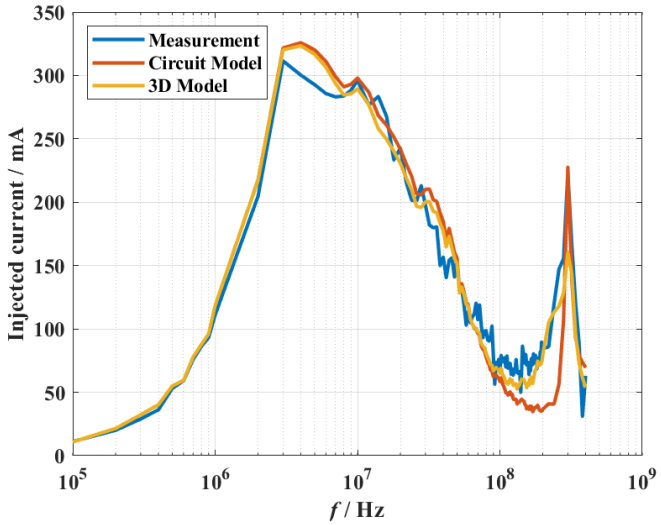


Figure 5.8.: Measured and simulated current for BCI injection into two copper rods, with the injetion position at the center, and all terminals terminated with 50 Ω resistors.

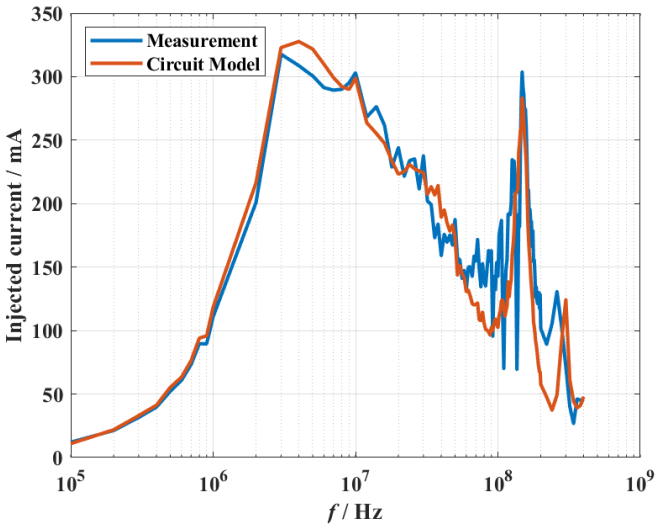


(a)

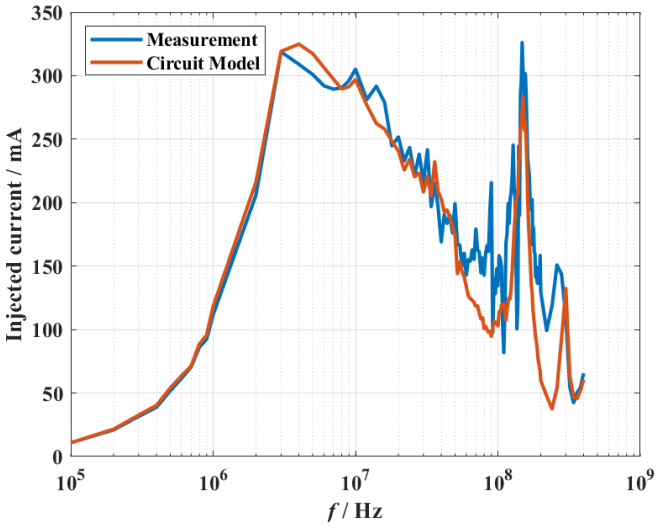


(b)

Figure 5.9.: Measured and simulated current for BCI injection into two copper rods, with the injetion position at 850 mm from the right side, and varying terminations. (a) all terminals are terminated with 50 Ω. (b) both terminals on the left are terminated with 100 Ω and both terminals on the right are shorted.

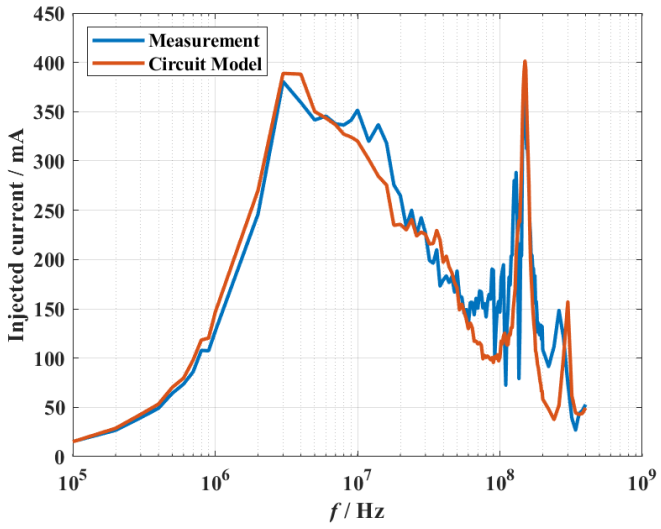


(a)

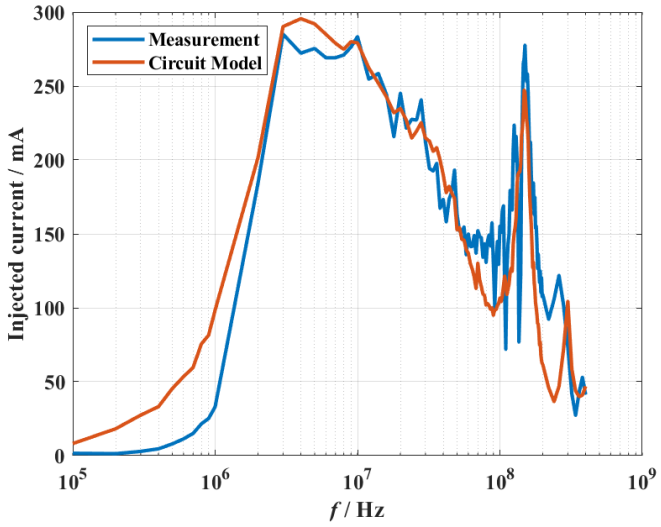


(b)

Figure 5.10.: Measured and simulated current for BCI injection into two copper rods, with the injetion position at 850 mm from the right side, and varying terminations. (a) one terminal on the right side is shorted all other terminals are terminated with 50 Ω. (b) one terminal on the right side is terminated with 100 Ω and the rest is again terminated with 50 Ω.

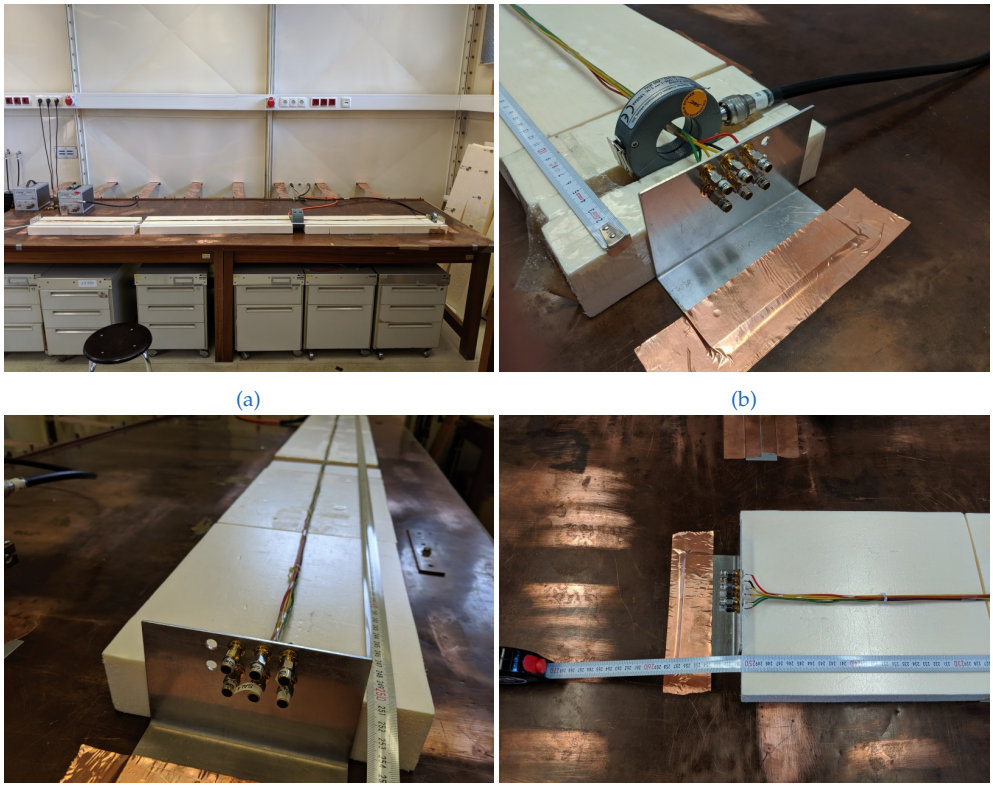

(a) (b)

(c) (d)

Figure 5.11.: This test setup consists of a 2.5 m long harness comprised of six isolated automotive wires (a). The harness was suspended 50 mm over the conducting ground plane with foam blocks. The foam blocks have a $varepsilon_r$ close to one and were therefore omitted in the simulation. The measurement and injection probe are positioned at 50 mm and 900 mm from the right side. All terminals are terminated by 50 Ω SMA resistors, shown in (c) and (d).

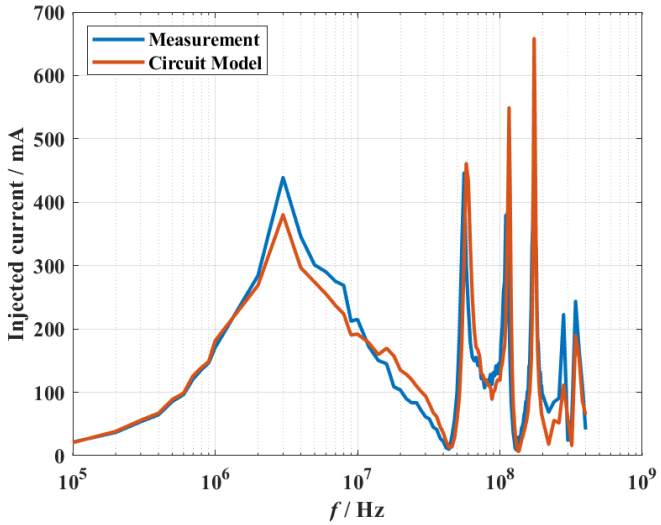


Figure 5.12.: Measured and simulated current for BCI injection into a 2.5 m six wire automotive cable.

# 6. Discussion

This work illustrates that the proposed circuit model can accurately replicate the behaviour of the injection current during a BCI test. The resonance location in the spectrum is accurately reproduced by the model even though the current was in some cases exaggerated at the resonance frequency. The proposed model showed comparable results to full 3D FEM simulation, whilst being far less computationally intensive. Because of the use of passive components, integration into any circuit simulation tool should work without hindrance.

Designers can easily integrate the model into their existing design and check at which frequencies during the test the common mode current will pose a risk to the performance of the DUT. With this new tool, designers can optimize their devices and protection circuitry for the harsh conditions of the BCI test before the first prototype is even produced.

This modelling approach is not without flaws. Models of distributed circuits, especially large distributed structures like cable harnesses, need a large number of passive components to replicate their frequency behaviour, even more so if you include RF effects like skin-effect or increase the bandwidth of the model. Similarly, the number of conductors included in the harness rapidly increases the component count and complexity. This is a significant drawback in case of setup changes and makes the model not easily suitable for recurring modifications, e.g. different wire harnesses.

Comparing the measurements with the simulations showed a constant deviation between the measured and simulated current for the injection into the calibration fixture. This can either be attributed to the source or the coupling model and should be investigated. There is also a deviation of the injection current for higher frequencies that is most likely related to inaccuracies of the calibration fixture model.

Further investigation of the coupling path from the probe to the harness and distinguishing between the coupled and non-coupled parts of the probe model could have potential to lead to improve the model of the coupling path. Also, currently, there is no data about proposed models performance regarding differential mode (DM) currents. Futher measurements would be necessary to evaluate the models performance regarding DM currents. A more modular and adaptable approach is intended to ease the workflow for circuit designers.

The missing of frequency dependent sources in LTSpice does not allow effortless simulation of the BCI test. This can be avoided by remote controling LTSpice and constructing the BCI simulation results from many simulation runs. This would ease access to this simulation method and increase dissemination of the proposed model.

# Appendix

# Appendix A.

# Schematics

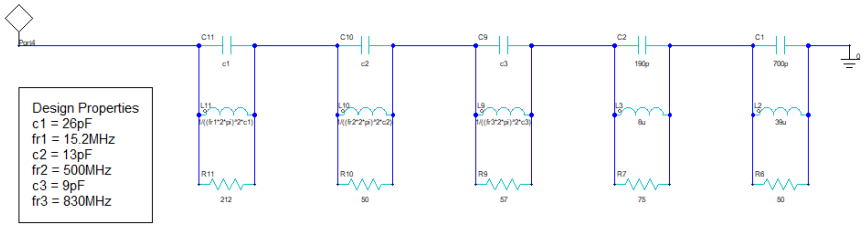


Figure A.1.: Circuit model of the injection probe.

# Appendix A. Schematics

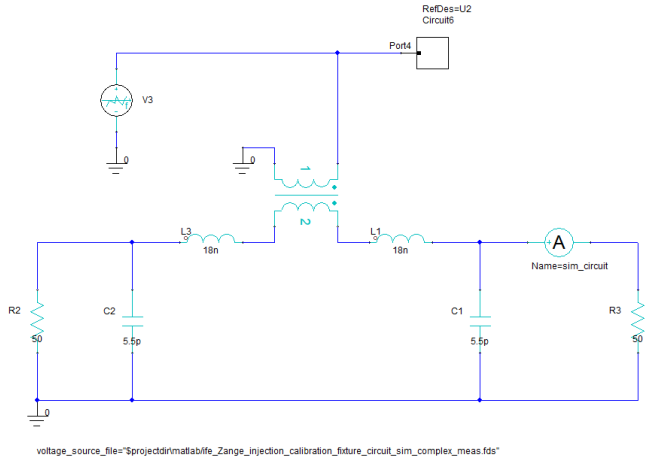


Figure A.2.: Circuit model for the BCI probe on the calibration fixture.

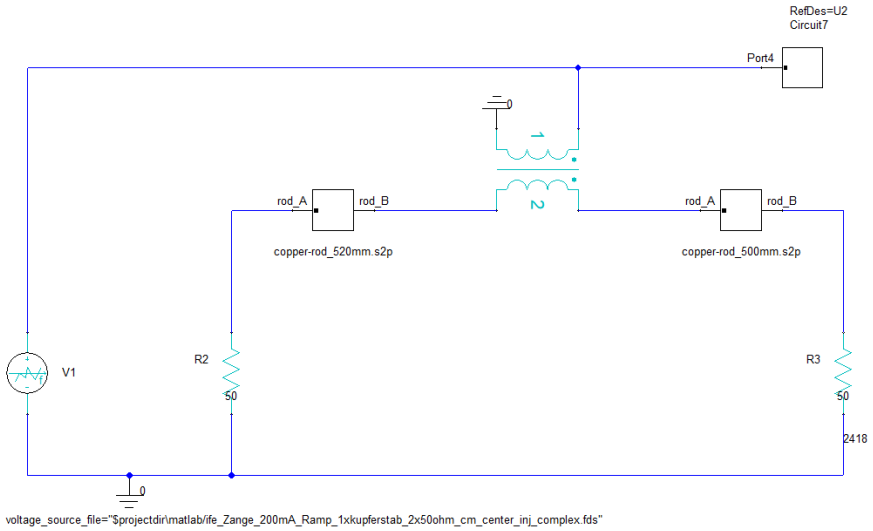


Figure A.3.: Circuit model for the BCI probe on a copper rod.

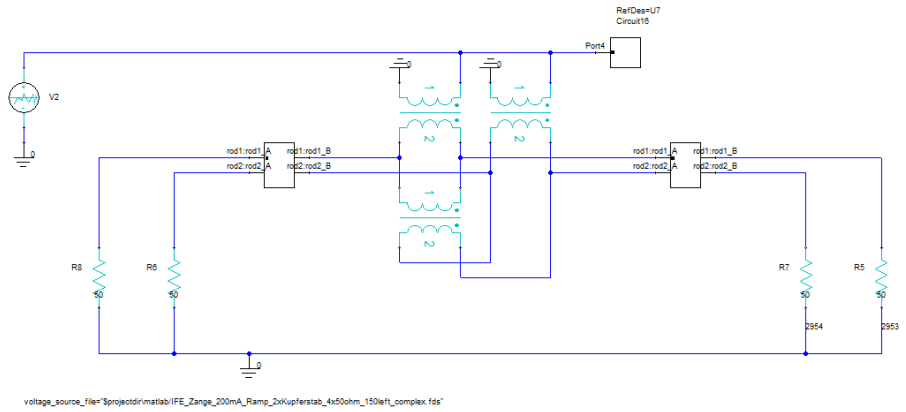


Figure A.4.: Circuit model for the BCI probe on two copper rods.

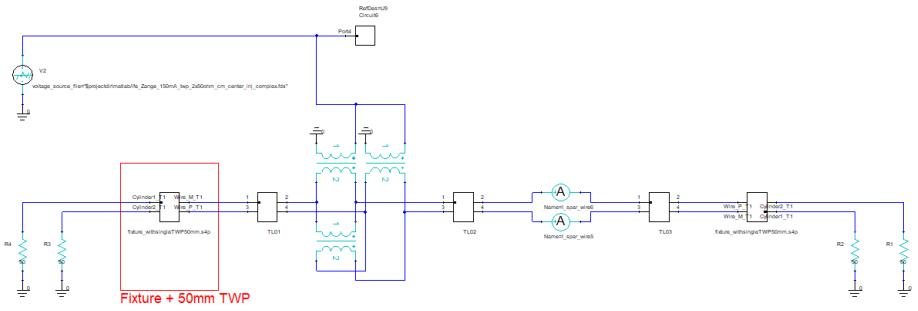


Figure A.5.: Circuit model for the BCI probe on a TWP.

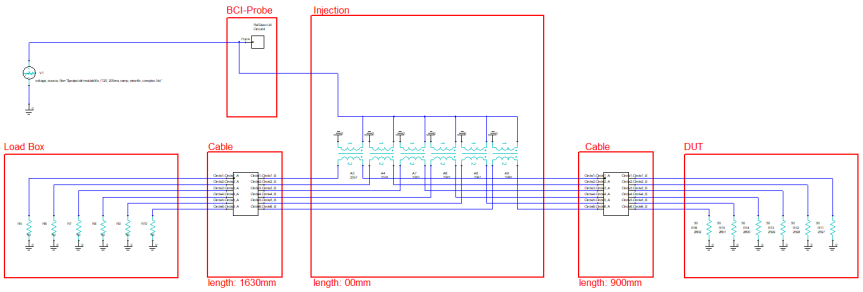


Figure A.6.: Circuit model for the BCI probe on six isolated wires.

# Bibliography


[1] A. Macleod, *Autonomous vehicles: the Chevy Spark problem*, 2017. [Online]. Available: https://www.mentor.com/mentor-automotive/blog/2017-12-17-Autonomous-vehicles--the-Chevy-Spark-problem (visited on 01/29/2021) (cit. on p. 1).

[2] ISO 11452-4:2011(E), "Road vehicles – component test methods for electrical disturbances from narrowband radiated electromagnetic energy – part 4: Harness excitation methods," International Organization for Standardization, Geneva, CH, Standard, Dec. 2011 (cit. on pp. 4, 17, 18, 20, 21, 23, 24, 87).

[3] M. F. Sultan, "Modeling of a Bulk Current Injection Setup for Susceptibility Threshold Measurements.," *IEEE International Symposium on Electromagnetic Compatibility*, pp. 188–195, 1986, ISSN: 01901494 (cit. on pp. 4–12).

[4] F. Grassi, F. Marliani, and S. A. Pignari, "Circuit Modeling of Injection Probes for Bulk Current Injection," *IEEE Transactions on Electromagnetic Compatibility*, vol. 49, no. 3, pp. 563–576, Aug. 2007, ISSN: 0018-9375. DOI: 10.1109/TEMC.2007.902385 (cit. on pp. 12–14, 79, 81).

[5] F. Lafon, Y. Belakhouy, and F. De Daran, "Injection probe modeling for bulk current injection test on multiconductor transmission lines," in *IEEE Symp. on Embedded EMC Proceedings, Rouen, France*, 2007 (cit. on pp. 13–16, 81).

[6] ISO 11452-1:2005(E), "Road vehicles – component test methods for electrical disturbances from narrowband radiated electromagnetic energy – part 1: General principles and terminology," International Organization for Standardization, Geneva, CH, Standard, Feb. 2005 (cit. on pp. 18, 22, 23).

[7] EMC Hire Ltd., *Fischer F-140 Bulk Current Injection Probe*, 2019. [Online]. Available: https://www.emchire.co.uk/product/fischer-f140-bulk-current-injection-probe-255 (visited on 10/29/2019) (cit. on p. 19).

[8] Fischer Custom Communications, Inc., *FCC-BCICF-2-1 bulk current injection probe fixtures*, 2019. [Online]. Available: https://www.fischercc.com/products/fcc-bcicf-2-1/ (visited on 11/21/2019) (cit. on p. 20).

[9] Teseq GmbH, *NSG 4070B ApplicAtioN for iSo 11452-4:2011*, 2013. [Online]. Available: http://www.teseq.com/products/downloads/application-notes/nsg_4070/nsg-%204070A/NSG_4070B_ISO_11452_4_e01.pdf (visited on 10/31/2019) (cit. on pp. 21, 22).

[10] T. Sato, *Possible influences of probe position, test harness length and load simulator impedance in bci test*, 2016. [Online]. Available: http://t-sato.in.coocan.jp/compliance/bci-probe-position.html (visited on 12/24/2019) (cit. on pp. 23–28).

[11] H. Heuermann, *Hochfrequenztechnik*. Springer Vieweg, 2018 (cit. on pp. 29, 34, 52, 65, 66, 68).

[12] M. Reta-Hernández, *Transmission line parameters*, 2012. [Online]. Available: https://www.unioviedo.es/pcasielles/uploads/proyectantes/cosas_lineas.pdf (visited on 12/05/2019) (cit. on pp. 39, 41, 46, 47).

[13] S. M. Bauer, "Modeling and Simulation of Conducted Disturbances in Automotive Systems," Master's thesis, Graz University of Technology, 2014 (cit. on p. 40).

[14] C. R. Paul and A. E. Feather, "Computation of the Transmission Line Inductance and Capacitance Matrices from the Generalized Capacitance Matrix," *IEEE Transactions on Electromagnetic Compatibility*, vol. EMC-18, no. 4, pp. 175–183, 1976, ISSN: 1558187X. DOI: 10.1109/TEMC.1976.303498 (cit. on pp. 44, 48, 49, 52–55).

[15] J. Clements, C. Paul, and A. Adams, "Computation of the Capacitance Matrix for Systems of Dielectric-Coated Cylindrical Conductors," *IEEE Transactions on Electromagnetic Compatibility*, vol. EMC-17, no. 4, pp. 238–248, Nov. 1975, ISSN: 0018-9375. DOI: 10.1109/TEMC.1975.303430. [Online]. Available: http://ieeexplore.ieee.org/document/4090962/%20http://ieeexplore.ieee.org/document/4090922/ (cit. on p. 48).

[16] S. Friedel, *How to calculate a capacitance matrix in comsol multiphysics®*, 2017. [Online]. Available: https://www.comsol.com/blogs/how-to-calculate-a-capacitance-matrix-in-comsol-multiphysics/ (visited on 12/10/2019) (cit. on p. 50).

[17] E. Bogatin, "Signal and Power Integrity - Simplified," in, Prentice Hall, 2018, ch. 7 (cit. on p. 55).

[18] M. Ibel, H. Hackl, B. Auinger, C. Stockreiter, and B. Deutschmann, "Survey on the generation of equivalent circuit cable models for transient simulation," in *2019 42nd International Convention on Information and Communication Technology, Electronics and Microelectronics (MIPRO)*, May 2019, pp. 102–107. DOI: 10.23919/MIPRO.2019.8757048 (cit. on p. 57).

[19] B. Carey-Smith, P. Warr, M. Beach, and T. Nesimoglu, "Wide tuning-range planar filters using lumped-distributed coupled resonators," *IEEE Transactions on Microwave Theory and Techniques*, vol. 53, no. 2, pp. 777–785, Feb. 2005, ISSN: 0018-9480. DOI: 10.1109/TMTT.2004.841221. [Online]. Available: http://ieeexplore.ieee.org/document/1393225/ (cit. on p. 58).

[20] H. A. Wheeler, "Formulas for the Skin Effect," *Proceedings of the IRE*, vol. 30, no. 9, pp. 412–424, 1942, ISSN: 00968390. DOI: 10.1109/JRPROC.1942.232015 (cit. on p. 57).

[21] M. Kazimierczuk, *High-Frequency Magnetic Components*. Wiley, 2011, ISBN: 9781119964919. [Online]. Available: https://books.google.at/books?id=t2TgU-uuNQ0C (cit. on pp. 57, 63).

[22] Biezl, *Skin effect*, 2008. [Online]. Available: https://en.wikipedia.org/wiki/Skin_effect (visited on 11/22/2019) (cit. on p. 60).

[23] I. Wikimedia Foundation, *Electrical resistivity and conductivity*, 2019. [Online]. Available: https://en.wikipedia.org/wiki/Electrical_resistivity_and_conductivity (visited on 11/21/2019) (cit. on p. 61).

[24] S. Kim and D. Neikirk, "Compact equivalent circuit model for the skin effect," *1996 IEEE MTT-S International Microwave Symposium Digest*, vol. 3, pp. 1815–1818, 1996, ISSN: 0149-645X. DOI: 10.1109/MWSYM.

1996.512297. [Online]. Available: http://ieeexplore.ieee.org/document/512297/ (cit. on pp. 61, 62).

[25] D. P. Neikirk, *Compact equivalent circuit model for the skin effect*, 1996. [Online]. Available: http://www.weewave.mer.utexas.edu/MED_files/MED_research/Intrcncts/Skin_Effect_Ldr/MTT_96_skn_ldr.html (visited on 11/22/2019) (cit. on p. 62).

[26] S. Caniggia and F. Maradei, *Signal Integrity and Radiated Emission of High-Speed Digital Systems*. Chichester, UK: John Wiley & Sons, Ltd, Nov. 2008, pp. 1–528, ISBN: 9780470511664. DOI: 10.1002/9780470772874. [Online]. Available: http://doi.wiley.com/10.1002/9780470772874 (cit. on pp. 63, 64).

[27] U. Gudmundsdottir, "Proximity effect in fast transient simulations of an underground transmission cable," *Electric Power Systems Research*, vol. 115, pp. 50–56, 2014, Special issue based on selected expanded contributions from the 10th International Conference on Power System Transients (IPST), ISSN: 0378-7796. DOI: https://doi.org/10.1016/j.epsr.2014.03.016. [Online]. Available: https://www.sciencedirect.com/science/article/pii/S0378779614001035 (cit. on p. 64).

[28] M. Ibel, H. Hackl, B. Auinger, C. Stockreiter, and B. Deutschmann, "Semi-automatic generation of lumped element transmission line circuits from 2d cross section," in *17. EMV-Fachtagung*, [Poster Session], Graz, Styria, Austria, Feb. 2019 (cit. on p. 69).

[29] J. G. Hayes, D. Cashman, M. G. Egan, T. O'Donnell, and N. Wang, "Comparison of test methods for characterization of high-leakage two-winding transformers," *IEEE Transactions on Industry Applications*, vol. 45, no. 5, pp. 1729–1741, 2009 (cit. on p. 70).

[30] S. A. Boulingui and A. C. Ndoye, "IC-EMC v2 – Application Note A model of the Bulk Current Injection Probe," no. 95242, pp. 1–9, 2010. [Online]. Available: http://www.ic-emc.org/appnotes/IC-EMC-Application-Note-BCI.pdf (cit. on p. 71).

[31] B. P. Nayak, A. Das, S. R. Vedicherla, and D. Gope, "Circuit models for Bulk Current Injection (BCI) clamps with multiple cables," *2018 IEEE International Symposium on Electromagnetic Compatibility and 2018 IEEE Asia-Pacific Symposium on Electromagnetic Compatibility, EMC/APEMC*

*2018*, pp. 1160–1163, 2018, ISSN: 1538-7836. DOI: 10.1109/ISEMC.2018.8393970 (cit. on p. 76).

[32] F. Grassi, "Accurate modeling of ferrite-core effects in probes for bulk current injection," *2009 IEEE International Conference on Microwaves, Communications, Antennas and Electronics Systems, COMCAS 2009*, 2009. DOI: 10.1109/COMCAS.2009.5385974. [Online]. Available: https://ieeexplore.ieee.org/abstract/document/5385974/ (cit. on p. 76).

[33] Z. Cui, F. Grassi, S. A. Pignari, and B. Wei, "Pulsed Current Injection Setup and Procedure to Reproduce Intense Transient Electromagnetic Disturbances," *IEEE Transactions on Electromagnetic Compatibility*, vol. 60, no. 6, pp. 2065–2068, 2018, ISSN: 00189375. DOI: 10.1109/TEMC.2017.2789206 (cit. on p. 76).

[34] F. Grassi, F. Marliani, and S. A. Pignari, "SPICE modeling of BCI probes accounting for the frequency-dependent behavior of the ferrite core," *XIXth General Assembly of U.R.S.I.,Chicago, IL, USA, Aug. 7-16*, pp. 2–5, 2008. [Online]. Available: http://www.ursi.org/proceedings/procGA08/papers/E07p6.pdf (cit. on p. 76).

[35] J. McLean and R. Sutton, "Dependence of the time- and frequency-domain response of BCI injection probes on the common-mode characteristic impedance of the cable bundle," *IEEE International Symposium on Electromagnetic Compatibility*, pp. 334–339, 2010, ISSN: 10774076. DOI: 10.1109/ISEMC.2010.5711296 (cit. on p. 76).

[36] G. Winkler and B. Deutschmann, "BCI-Tests - Durchführung und Herausforderung," in *17. EMV-Fachtagung*, G. Winkler, Ed., ser. OVE-Schriftenreihe, 27-28 February 2019, vol. 98, Österreichischer Verband für Elektrotechnik, pp. 127–139 (cit. on p. 89).